W Alss 2270
S

STELLINGEN

behorende bij het proefschrift

Testing, Modelling and Numerical Analysis of the Mechanical Behaviour of Bituminous Concrete

P.G. Bonnier, Delft, 1993

1. Het door Sluys in zijn proefschrift gestelde, dat een Perzyna overstress model niet gebruikt kan worden voor hoekige vloeioppervlakken of vloeioppervlakken met een apex, is onjuist.

   L.J. Sluys, 'Wave Propagation, Localisation and Dispersion in Softening Materials', Proefschrift TU Delft, 1992, p 106-107.

2. Materiaalgedrag is nodig voor het bepalen van constructiegedrag. Bij het ontwikkelen van modellen voor het materiaalgedrag is het noodzakelijk rekening te houden met het feit dat een model (in de toekomst) gebruikt kan worden voor het berekenen van constructies. Indien hier geen rekening mee wordt gehouden volgt er een model dat voor de praktijk weinig waarde heeft.

3. Vermindering van het aantal (betaalde) arbeidsuren zal vaak gecompenseerd dienen te worden door toenemend hobbyïsme van de betrokken werknemer.

4. Het gebruik van meerdere Kelvin-Voigt elementen in een visco-elastisch model verruimt de toepassingsmogelijkheden, zonder dat voor iedere toepassing andere parameters gekozen dienen te worden. In een eindige-elementen-berekening zullen hierbij de rekentijden nauwelijks toenemen.

5. De aanname dat het volume van de zettingstrog bij het boren van tunnels gelijk is aan het teveel ontgraven volume grond is onjuist.

6. Het introduceren van normen ondermijnt het gebruik van het gezonde verstand van degenen die de normen moeten toepassen.

7. Het gebruik van complexe modellen verhoogt het inzicht in het werkelijke gedrag van constructies.

8. Het vergelijken van parameters voor verschillende materiaal-modellen is lang niet altijd mogelijk. Daarom dient de term 'materiaal-parameters' niet gebruikt te worden. Een term als 'model-parameter' is meer op zijn plaats.

9. Het meenemen van de stijfheid van een bekledingslaag bij de analyse van opdrijfproblemen geeft hogere toelaatbare overdrukken dan volgt uit een één-dimensionale beschouwing. In dit proefschrift is dit aangetoond voor een ontkoppelde grondwater en deformatie berekening. Bij een gekoppelde analyse zal een hogere veiligheid worden gevonden.

10. Beter een kind dat niet hoort dan een kind dat niet luistert.

TR diss
2278

TESTING, MODELLING AND NUMERICAL ANALYSIS OF THE MECHANICAL BEHAVIOUR OF BITUMINOUS CONCRETE

PROEFSCHRIFT

ter verkrijging van de graad van doctor aan
de Technische Universiteit Delft, op gezag van
de Rector Magnificus, prof. ir. K.F. Wakker,
in het openbaar te verdedigen ten overstaan van een
commissie aangewezen door het College van Dekanen
op maandag 25 oktober 1993 te 14.00 uur

door

Paul Godfried Bonnier

geboren te Nijmegen
civiel ingenieur

BIBLIOTHEEK TECHNISCHE UNIVERSITEIT
Prometheusplein 1
DELFT

Dit proefschrift is goedgekeurd door de promotor: prof.dr.ir. A. Verruijt
Toegevoegd promotor: dr.ir. P.A. Vermeer

Aan Irene en Bas

ACKNOWLEDGEMENTS

The research for this thesis was carried out at the Geotechnical Laboratory of the Faculty of Civil Engineering of Delft University of Technology, under the supervision of dr. P.A. Vermeer.

The research project was initiated by ir. E. Troost, working at the time both for the Structural Research Division (BSW) and the Road and Hydraulic Engineering Division (DWW) of the Dutch Ministry of Transport, Public Work and Watermanagement (RWS). It was partly financed through the Cornelis Lely Foundation and partly through the Technical Advisory Committee on Water Defences. As the material testing involved was very costly, substantial contributions were obtained from various groups within RWS; Material Testing and Hydraulic Engineering (DWW) and the Structural Research Division (Bouwdienst). I wish to acknowledge not only ir. E. Troost but also ir. J. Lindenberg for coordinating finances and their technical support during the research.

As indicated above, a substantial testing program was carried out on bituminous concrete samples. This was done at Delft Geotechnics in a special temperature controlled triaxial cell. It was done by Mr. L. Smidt under the direct supervision of ir. P.A. Ruygrok. I have greatly appreciated the stimulating discussions with ir. P.A. Ruygrok.

During my stay in the Geotechnical Laboratory of Delft University, I enjoyed the stimulating interaction with colleagues; especially those of the PLAXIS Research and Development Team.

P.G. Bonnier

CONTENTS

1. INTRODUCTION 1

1.1 Aims and scope of this study 1
1.2 Contents of this thesis 2
1.3 Notation 4

2. SECONDARY CREEP BEHAVIOUR 5

2.1 General formulas for secondary creep in uniaxial tests 5
2.2 Constant strain rate in standard triaxial tests 7
2.3 Two options for secondary creep 11

3. PRIMARY CREEP BEHAVIOUR 13

3.1 Primary creep in uniaxial compression tests 13
3.2 Primary creep in triaxial compression tests 15
3.3 Analytical solution for multiple-step creep tests 17
3.4 Verification by data from multiple-step creep tests 18

4. VERIFICATION OF HARDENING CONCEPT FOR PRIMARY CREEP 21

4.1 Determination of hardening function from stress relaxation tests 21
4.2 Reproducibility of relaxation tests 22
4.3 Influence of deformation rate on relaxation curve 24
4.4 Influence of confining pressure on relaxation curve 25
4.5 Formulation of hardening curve 26
4.6 Results of extension relaxation tests 28
4.7 Relaxation tests without confining pressure 30

5. VISCO-ELASTIC BEHAVIOUR 37

5.1 Visco-elasticity in the classical formulation 37
5.2 Visco-elasticity using spring/dashpot models 39
5.3 Response to sinusoidal loading 41
5.4 From a simple Zener model to a Kelvin-Voigt series model 45
5.5 Determination of visco-elastic material parameters for Delft bituminous concrete 48
5.5 Concluding remarks on visco-elasticity 55

6. THE INFLUENCE OF TEMPERATURE ON MATERIAL BEHAVIOUR 57

6.1 The influence of temperature on viscosity η 57
6.2 Shift function S(T) for cyclic loading 59
6.3 The influence of temperature on the hardening function for visco-plasticity 64
6.4 The influence of temperature on the time parameter τ 67
6.5 Concluding remarks on temperature dependency 68

7. GENERAL 3-D CONSTITUTIVE MODEL 71

7.1 General framework of the model 71
7.2 Generalization of Kelvin-Voigt series model 72
7.3 Generalization of visco-plastic creep model 76
7.4 Some comments on the shape of the yield function 82

8. TIME INTEGRATION OF DIFFERENTIAL STRESS-STRAIN MODEL 85

8.1 Basic time-integration 85
8.2 Integration of visco-elastic strain rates 88
8.3 Integration of visco-plastic strain rates 90
8.4 Critical time steps for visco-elasticity 92
8.5 Theory on time step selection for visco-plasticity 95
8.6 Manipulation of control parameters for visco-plasticity 101
8.7 Simulation of multiple-step creep test 103
8.8 Simulation of stress-relaxation test 105

9. FINITE ELEMENT IMPLEMENTATION AND VALIDATION 107

9.1 Compatibility and equilibrium equations for finite element analysis 107
9.2 Finite element equations 109
9.3 Accelerated solution techniques 111
9.4 Validation of finite element implementation 113

10. ANALYSIS OF REVETMENT UNDER HYDRAULIC UPLIFT PRESSURES 117

10.1 One-dimensional considerations 118
10.2 Two-dimensional ground water flow analysis 120
10.3 Input for two-dimensional deformation analysis 125
10.4 Material data for bituminous concrete 127
10.5 Two-dimensional calculations and results 130
10.6 Concluding remarks 134

11. PERMANENT DEFORMATIONS IN ROADS 137

11.1 Modelling of the problem 137
11.2 Initial situation 139
11.3 Simulations 140
11.4 Application of multiple load pulses 144
11.5 Concluding remarks 147

12. DISCUSSION AND CONCLUSIONS 149

Appendix MATERIAL DESCRIPTION 153

REFERENCES 157

SUMMARY IN DUTCH (SAMENVATTING) 161

1. INTRODUCTION

Bituminous concrete is often used for the construction of road surfaces and revetments for embankments. For the design of such structures in bituminous concrete the linear elastic model for mechanical behaviour is most often used. This limits the possibilities for analysing and predicting deformations such as rut formation for road surfaces and uplift for revetments of embankments which often occur in practice.

To improve the quality of analysis and predictions of the behaviour of bituminous concrete structures, it is necessary to construct a material model with the aid of which its behaviour can be described under a variety of conditions. To this end Rijkswaterstaat initiated research in this field (Troost, 1989).

For the development of a new model for bituminous concrete a series of triaxial experiments was carried out on samples taken from an existing revetment in the neighbourhood of West-Kapelle. These samples were tested at Delft Geotechnics. The results of these tests are reported in this study. For the sake of simplicity this material will be referred to as Delft bituminous concrete.

1.1 Aims and scope of this study

The main aim of this study is to develop a constitutive model for bituminous concrete. This material model should be able to describe the most important types of behaviour of the material in practical situations. In practice, bituminous concrete serves as a load-bearing layer or a protection layer on a granular sub-base.

In hydraulic engineering, where the material is used, for instance, to protect embankments, one can distinguish between short and long loading times. Wave attack on revetments of embankments is an example of rapid loading whilst uplift of a revetment can be caused by much slower tidal movements. In road engineering both short-term and long-term loading also occur. Loading by moving traffic is an example of short term loading. On a

parking-lot loading times are much longer. Compared to hydraulic structures, road structures are subjected to relatively high loads. The constitutive model should take this variety of load situations into account.

Another important effect is that of temperature. In practical situations temperature plays an important role in the development of deformations. Temperature-dependent model parameters have therefore been derived.

The second aim is to develop numerical procedures and implement these procedures in a finite element program (PLAXIS) which can be used for the analysis of practical structures.

1.2 Contents of this thesis

This study of the deformation behaviour of bituminous concrete - as is the case with the study of many other materials - is based on two theoretical approaches to deformation behaviour, namely that of reversible visco-elastic strain and that of irreversible visco-plastic strain. This thesis starts in Chapters 2, 3 and 4 with a description of the irreversible strains using the concept of over-stress visco-plasticity (Perzyna, 1966). In Chapter 2 restriction is made to so-called secondary creep as relevant for high stresses. In Chapter 3 the formulations are extended to include so-called primary creep relevant for relatively low stresses. To include primary creep, a hardening law is used. In Chapter 4 a great deal of experimental evidence is put forward for the existence of a unique hardening curve. This hardening curve appears to be independent of, for instance, the rate of deformation, temperature and confining pressure. In this chapter attention is also focused on the behaviour under low compressive and tensile stresses.

In Chapter 5 visco-elasticity is discussed. The reversible visco-elastic strains are described using a chain of Kelvin-Voigt elements. Test results involving cyclic loading are considered and compared to results for loading-unloading tests. It appears that the results from cyclic tests and loading-unloading tests can be combined to give a consistent whole which can be described using a series of Kelvin-Voigt elements.

Temperature plays an important role in the deformation of bituminous concrete. In Chapter 6 the influence of temperature on the model parameters is investigated. It has been found that temperature-dependent model parameter can be derived using rather simple formulas.

Whereas the model equations are derived for uniaxial and triaxial testing situations in Chapters 2 to 6, Chapter 7 describes the model for general three-dimensional states of stress and strain. In this chapter material parameters, both visco-elastic and visco-plastic, for Delft bituminous concrete are listed.

In Chapter 8 attention is focused on time integration of the model equations. In the previous chapters, model equations were derived using strain rates. For calculations one has to use finite time increments. One therefore needs incremental relations for stress and strain. Attention is also focused on the convergence and accuracy of the time integration. Two test types are simulated using a program for homogeneous states of stress and strain.

In Chapter 9 the equations for a boundary value problem are stated including some acceleration techniques. A problem involving a visco-elastic layer is treated to validate the finite element implementation.

Chapter 10 deals with the analysis of a revetment under hydraulic uplift pressures. For the problem of uplift of a revetment, results from a time-dependent ground water flow calculation are presented. These results are used to calculate deformations and the safety of a revetment. The safety is compared to the uplift criterion in the Dutch guidelines.

Chapter 11 deals with permanent deformations in roads. A simplified problem for rut formation due to heavy traffic is considered. Instead of moving loads, as in practice, a non-moving load is considered and attention is focused on the permanent deformations and the mechanisms that occur during a number of load pulses.

Chapter 12 contains some general considerations on the subject. In this chapter several suggestions are given for future research on the behaviour of the material and the application to practical problems.

1.3 **Notation**

The derivation of the model equations is primarily based on uniaxial and triaxial states of stress and strain. Therefore, we use practical variables for the description on the model. Later, from Chapter 7 where the model is generalized for three dimensional states of stress and strain, we use matrix-vector notation. A single underscore is used to identify a vector and a matrix is indicated by a double underscore. A global list of symbols is not included because several symbols have more than one meaning. Instead, symbols are defined when they first appear.

2. SECONDARY CREEP BEHAVIOUR

In this chapter attention is focused on secondary creep behaviour. A model is developed within the framework of Perzyna's (1966) over-stress theory. Four material parameters are used to characterize the creep mechanism; two of them are temperature dependent. The validity of the model is demonstrated using triaxial testing data.

2.1 General formulas for secondary creep in uniaxial tests

Creep tests on bituminous concrete give results as also found for metals at high temperatures (Odqvist, 1966; Hult, 1966). In general we can distinguish three stages of creep as illustrated in Fig. 2.1. In the first stage of so-called primary creep we observe a decreasing strain rate. In the second stage of so-called secondary creep, the creep strain rate is approximately constant. In the third stage of tertiary creep, the creep strain rate increases.

In Fig. 2.2a typical results from creep tests on bituminous concrete are shown. The lower curves represent data at low stress levels, the upper curves show data for higher stress levels. Creep tests at very low stress levels show only primary creep, i.e. the creep strain rate gradually decreases to zero and the total strain reaches a distinct final value. Hence, at a very low stress level, the secondary creep strain rate is simply equal to zero.

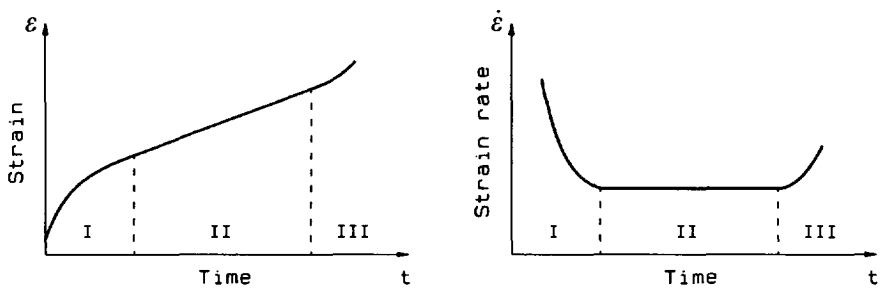

Fig. 2.1. Strain and strain rate in uniaxial creep test. Three different stages: primary creep, secondary creep and tertiary creep.

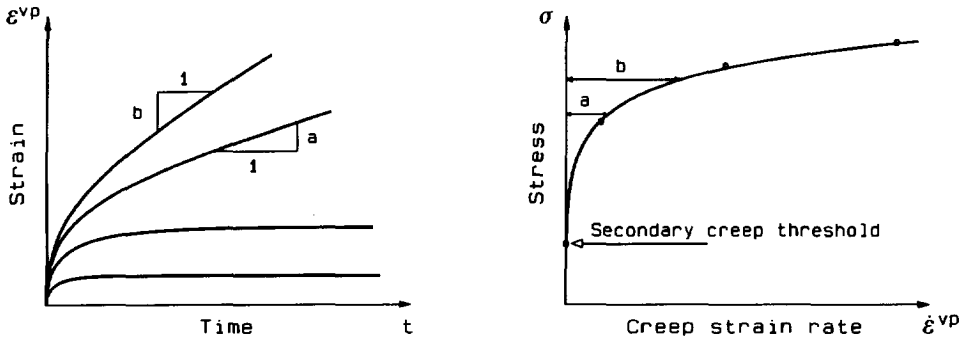

Fig. 2.2. (a) Typical creep data for different constant stresses.
(b) Secondary creep strain rates as a function of stress level.

Creep tests at relatively high stress levels show primary creep first, in the sense that the creep strain rate decreases with time. After this first stage of primary creep a stage of secondary creep follows. During secondary creep the strain rate remains constant. The constant secondary creep strain rate depends on the applied stress, for higher stress values higher values of the secondary creep strain rate will be found. Below a particular secondary-creep-threshold stress no secondary creep is observed. On evaluating the secondary creep strain rate from testing data for various different stress levels, one can obtain a curve as shown in Fig. 2.2b.

Instead of using creep tests with constant stress level, one may also perform tests with different constant strain rates. During such a test the stress will increase up to a particular value, which depends on the applied rate of deformation as illustrated in Fig. 2.3. The pre-peak strains in this figure result from primary creep and elasticity. The post-peak strain consists of secondary creep only. From such data we can obtain the curve of Fig. 2.2b. In fact the curve of Fig. 2.2b was obtained by evaluating data from constant strain rate tests on bituminous concrete as published by Di Benedetto (1987). It relates to uniaxial compression tests at a temperature of 23 °C.

In literature, various functions are used to model secondary creep, for instance the power law as proposed by Norton (1929) and Bailey (1929) and the hyperbolic sine function as proposed by Prandtl (1928). From this hyperbolic

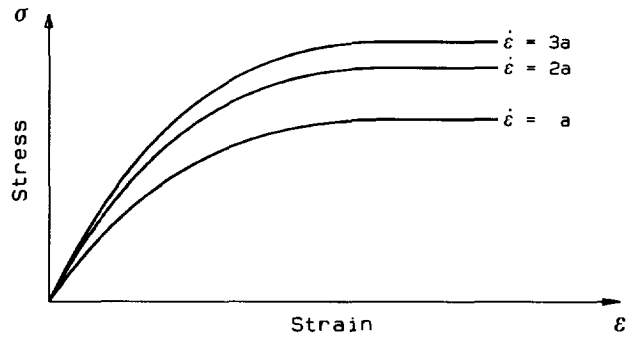

Fig. 2.3. Typical results for uniaxial compression tests with different constant rates of deformation.

sine function, a simpler exponential function can be derived as proposed by Soderberg (1936). Hence we have different options for the secondary creep strain rate (a rate is indicated by a superimposed dot):

$$\dot{\varepsilon}^{vp} = \frac{1}{\tau}(\sigma-\sigma_{sct})^{\beta} \qquad \text{for } \sigma > \sigma_{sct}$$

$$\dot{\varepsilon}^{vp} = \frac{1}{\tau}\sinh(\beta\sigma-\beta\sigma_{sct}) \qquad \text{for } \sigma > \sigma_{sct} \qquad (2.1)$$

$$\dot{\varepsilon}^{vp} = \frac{1}{\tau}\left(e^{\beta(\sigma-\sigma_{sct})} - 1\right) \qquad \text{for } \sigma > \sigma_{sct}$$

σ_{sct} stands for the secondary-creep-threshold stress. The parameter τ depends heavily on temperature (see Section 6.4). To some extent all the above functions can be used to describe test data, but in the following we will use the power law.

2.2 Constant strain rate in standard triaxial tests

In addition to uniaxial tests, Di Benedetto (1987) performed constant strain rate tests at various different confining pressures. In fact, standard triaxial tests were performed with $\sigma_2 = \sigma_3$ = constant. From his data we derived lines of constant secondary creep strain rates as shown in Fig. 2.4. In this figure p and q are defined as

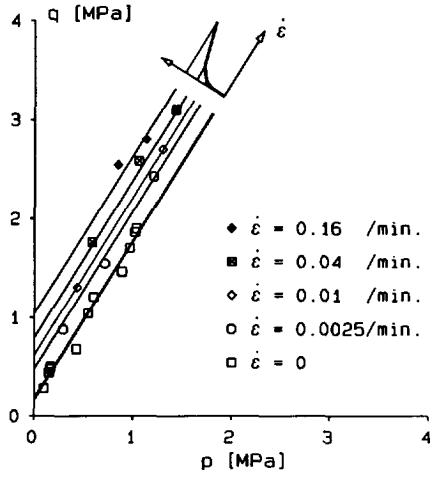

Fig. 2.4. Results from constant strain rate triaxial tests for various different confining pressures and deformation rates after Di Benedetto.

$$p = \frac{1}{3}(\sigma_1 + 2\sigma_3) \ , \qquad q = \sigma_1 - \sigma_3 \tag{2.2}$$

where σ_1 is the axial stress and σ_3 is the confining pressure. Note that pressure is considered positive. The markers in the figure represent stress combinations from actual tests.

Interpreting the data, we found that parallel lines can be used to fit the data. Each line in the figure is found for a particular value of the applied rate of deformation. At the end of the constant strain rate tests, after which the maximum stress was to remain constant, further strain was blocked by Di Benedetto; i.e. the strain rate was set equal to zero. After this the stresses were found to decrease in time until a final constant value was reached. We have used these post-relaxation stresses to evaluate the secondary-creep-threshold locus in the *p*-*q*-plane. From the data in Fig. 2.4 it follows that the secondary-creep-threshold value depends on the applied confining pressure or, more generally, on the isotropic stress *p*. As for the loci of constant creep rate we find a straight line. In fact all lines are parallel and they give a very consistent whole.

Similar to failure of soils and other granular materials, the secondary-creep-threshold can be described using a friction angle and a cohesion. They will be denoted as ϕ_{sct} and c_{sct} respectively. From the testing data by Di Benedetto we find $\phi_{sct} = 39^{\circ}$ and $c_{sct} = 150$ kPa, at least for a temperature of 23 °C. Di Benedetto did not introduce the concept of a secondary-creep-threshold, but by considering his data, it appears that this concept can be used. Considering his data, it is found that ϕ_{sct} hardly depends on temperature (see also Section 6.4). Indeed, within a range of 35 degrees Celsius very little variation of ϕ_{sct} is observed as indicated in Table 2.1. On the contrary, the cohesive threshold rapidly decreases when temperature is increasing.

To be able to find values for β and τ we need to extend the power law (2.1a) from uniaxial stress to general states of stress. For stress states as met in triaxial tests this formula can be extended to obtain

$$\dot{\varepsilon}^{vp} = \frac{1}{\tau}\left(\frac{q-q_{sct}}{q_0}\right)^{\beta}, \qquad q_0 = 1 \text{ MPa} \tag{2.3}$$

Formally the parameter q_0 can be chosen freely, but we will always use a value of 1 MPa. The value of q_{sct} is the secondary creep threshold of the deviatoric stress q. Note that this value depends on the isotropic stress and can be calculated using the friction angle ϕ_{sct} and the cohesion threshold value c_{sct} (Fig. 2.5).

$$q_{sct} = (p + a_{sct})\, M_{sct} \tag{2.4}$$

$$a_{sct} = c_{sct} \operatorname{cotg} \phi_{sct} \quad ; \quad M_{sct} = \frac{6 \sin \phi_{sct}}{3 - \sin \phi_{sct}} \tag{2.5}$$

Using equation (2.3) we found values of the creep exponent β and the time parameter τ. From Table 2.1 we also observe that the creep exponent β shows little variation for different temperatures. The parameter τ varies strongly with temperature; see Section 6.4 for details. Also, caution is necessary because τ will depend on the value of the creep exponent β and it is difficult to compare values of τ when a different value of β is found.

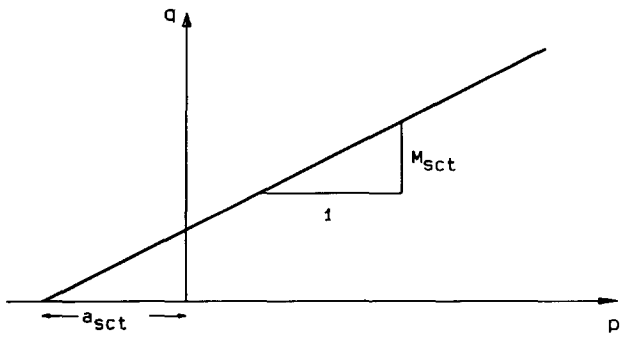

Fig. 2.5. Parameters M_{sct} and a_{sct} for triaxial compression tests.

Table 2.1. Material parameters for equation (2.3) from constant strain rate triaxial tests performed by Di Benedetto.

T [°C]	ϕ_{sct}	c_{sct} [kPa]	τ [s]	β
5	37	320	320000	4.5
23	39	150	3300	3.4
41	39	90	200	4.1

Not all bituminous concrete mixtures give secondary creep thresholds as high as the ones presented in Table 2.1. From tests on a different bituminous concrete we obtained ϕ_{sct} = 15° and c_{sct} = 55 kPa, at least for a temperature of 28 °C. The differences in the friction angle and the cohesion between the tests performed by Di Benedetto and tests performed in Delft can be explained by considering the different mixtures. Di Benedetto tested a well-graded bituminous concrete with a bitumen content of 7.3 per cent which is commonly used in road engineering. We tested a gap-graded bituminous concrete with a bitumen content of 6.2 per cent for application in hydraulic engineering. For details the reader is referred to the Appendix. It is an extremely loose skeleton of fairly coarse gravel. Such a loose granular skeleton will obviously yield a very low friction angle.

2.3 Two options for secondary creep

In Section 2.1 a number of formulations are given for the creep behaviour in uniaxial tests. Properly applied, the power law, the sine hyperbolic law and the exponential law (eq. 2.1) all give a reasonable description of the secondary creep; in fact, test results can be described with all three formulations. The power law is definitely effective, but this option is not compulsory because the other formulations also give good results.

Also when extending the power law of uniaxial state of stress to triaxial state of stress, there are several other possibilities, for example

$$\dot{\varepsilon}^{vp} = \frac{1}{\tau}\left(\frac{q}{q_0} - \frac{p^*}{q_0} M_{sct} \right)^{\beta} \tag{2.6}$$

$$\dot{\varepsilon}^{vp} = \frac{1}{\tau}\left(\frac{q}{p^*} - M_{sct} \right)^{\beta} \tag{2.7}$$

in which $p^* = p + a_{sct}$. The first option is in accordance with equation (2.3) and in this case all contours for constant $\dot{\varepsilon}^{vp}$ are parallel to the Coulomb line $q=p^*M_{sct}$. The second option according to equation (2.7) does not show parallel contour lines but a fan of lines through the point $p^*=0$.

In view of the test results in Fig. 2.4, the parallel contour lines according to equation (2.6) appear somewhat better than the rotating contour lines in equation (2.7), but data from other researchers may possibly indicate otherwise. For the practical application of a bituminous concrete model, both formulas are, however, acceptable, because bituminous concrete is seldom used with high mean stresses p. These are usually a dyke surface or a road surface with stresses in the ringed area in Figures 2.6a and 2.6b. As can be seen in the figure, there is in this limited stress area hardly any difference between parallel and rotating contour lines. For this reason the choice between equations (2.6) and (2.7) also becomes less important.

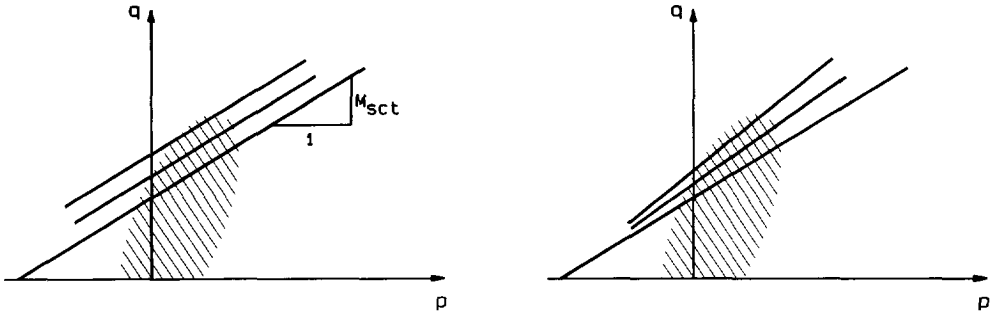

Fig. 2.6 Practical stress combinations for bituminous concrete.

3. PRIMARY CREEP BEHAVIOUR

In the previous chapter attention was focused on secondary creep. In this chapter attention is focused on extending the formulation for secondary creep to include the primary creep.

3.1 Primary creep in uniaxial compression tests

In the previous chapter an over-stress model was used; this means that continued creep is only possible when the stress is above a certain value. The formulas of equation (2.1) only apply if $\sigma > \sigma_{sct}$. At lower stress no continued straining will take place. However, some limited irreversible straining may take place. A possible adjustment to the previously used power-law (2.1a) is the formulation:

$$\dot{\varepsilon}^{vp} = \frac{1}{\tau}\left(\frac{\sigma}{\sigma_0} - h(\varepsilon^{vp})\right)^{\beta} \qquad \text{for} \qquad \frac{\sigma}{\sigma_0} > h(\varepsilon^{vp}) \tag{3.1}$$

where $h(\varepsilon^{vp})$ is a yet unknown hardening function, β is the creep exponent and τ is a creep time constant. The constant σ_0 can be chosen more or less arbitrarily. Obviously a change in σ_0 will require a change in the function h and the creep time constant τ. Both the hardening function $h(\varepsilon^{vp})$ and the coefficients β and τ should be determined using test data. The determination of a hardening function will be discussed in Chapter 4. Here we will, for the time being, assume a monotonically increasing function which increases to a limiting value of σ_{sct}/σ_0. When this limiting value is reached, formula (3.1) is equivalent to the power-law formulation (2.1a).

To show the behaviour of equation (3.1), we will consider a creep test at a low stress level. For a low stress level, and thus small creep strains, we use a linearization of the hardening function to obtain

$$h(\varepsilon^{vp}) \approx H \cdot \varepsilon^{vp} \tag{3.2}$$

where $H = dh/d\varepsilon^{vp}$. Introducing this linearization in equation (3.1) we obtain

$$\dot{\varepsilon}^{vp} = \frac{1}{\tau}\left(\frac{\sigma}{\sigma_0} - H\varepsilon^{vp}\right)^{\beta} \tag{3.3}$$

This differential equation can be solved to obtain:

$$\varepsilon^{vp} = \frac{\sigma}{H\sigma_0}\left(1 - (1 + at)^{-b}\right) \tag{3.4a}$$

where for $\beta \neq 1$:

$$a = \frac{H}{\tau}(\beta-1)\left(\frac{\sigma}{\sigma_0}\right)^{\beta-1}, \qquad b = \frac{1}{\beta-1} \tag{3.4b}$$

For comparing these equations with test data, it should be realized that bituminous concrete exhibits not only creep strains but also an elastic strain component. Hence the general equation reads

$$\varepsilon = \varepsilon^{e} + \varepsilon^{vp} \tag{3.5}$$

The elastic behaviour will, for the time being, be modelled using the simplified formulation

$$\varepsilon^{e} \approx \frac{\sigma}{E} \tag{3.6}$$

where E is Young's modulus. For Delft bituminous concrete as described in the Appendix, Young's modulus was found to be 300 MPa, at least at a temperature of T = 28 °C and for long periods of loading. On using equations (3.4a), (3.5) and (3.6), the total strain can be written as

$$\frac{\varepsilon}{\varepsilon_{max}} = 1 - \frac{E}{E + H\sigma_0}(1 + at)^{-b} \tag{3.7a}$$

where

$$\varepsilon_{max} = \frac{\sigma}{E} + \frac{\sigma}{H\sigma_0} \tag{3.7b}$$

The analytical solutions for different values of the creep exponent β are shown in Fig. 3.1. For this figure, the ratio of E over $H\sigma_0$ was chosen to be 9, so that ε^{e} is 10 per cent of the total strain ε_{max}. Furthermore, a

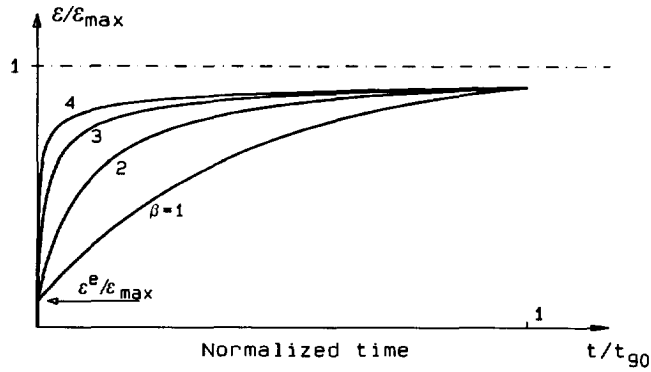

Fig. 3.1. Analytical solutions for different values of β.

normalized time is used by introducing t_{90}. This is the elapsed time up to 90 per cent of the total creep strain. The concept of t_{90} is introduced simply as a convenient factor of normalization. Curves are plotted for different values of the exponent β. Just after loading, a high creep rate is observed, at least for $\beta \geq 2$, but the creep rate gradually decreases. In fact a very long time, well beyond t_{90}, is needed for the entire creep process. Considering for instance the particular case of β=3, the time to reach 95 per cent of the total creep strain will take 4 times as long as it takes to reach 90 per cent.

The analytical solution (3.7) is very important for interpreting test data. Due to the linearization (3.2), it would seem that its application is restricted to small loads. However, relatively large values of σ/σ_0 can be considered when using the mean value theorem. Then H is not defined as $dh/d\varepsilon^{vp}$ but

$$H = \frac{h(\varepsilon^{vp}_{max}) - h(0)}{\varepsilon^{vp}_{max}} \tag{3.8}$$

3.2 Primary creep in triaxial compression tests

In this section the formula for primary creep will be extended to triaxial conditions with $\sigma_2 = \sigma_3 \neq 0$. Hence, instead of uniaxial states we consider a confining pressure $\sigma_2 = \sigma_3$. Suitable stress measurements for a triaxial test are defined as

$$q = \sigma_1 - \sigma_3 , \qquad p^* = \frac{1}{3}(\sigma_1 + 2\sigma_3) + a_{sct} \tag{3.9}$$

where a_{sct} is defined by equation (2.5).

Primary creep and secondary creep can now be combined into the single formula:

$$\dot{\varepsilon}^{vp} = \frac{1}{\tau}\left(\frac{q}{p^*} - h(\varepsilon^{vp})\right)^{\beta} \tag{3.10}$$

The difference with equation (3.1) is that σ/σ_0 is replaced by q/p^*. The function h increases monotonically up to a limiting value of M_{sct} as illustrated in Fig. 3.2. Hence, up to $h(\varepsilon^{vp}) = M_{sct}$ we have primary creep and we have secondary creep as soon as $h(\varepsilon^{vp})$ has reached the value of M_{sct}.

For verification and determination of material parameters, we performed special creep tests: the so-called multiple-step creep tests. In these tests various different stress levels were applied. For each step, a constant stress level is maintained until the (creep) strains have reached an ultimate value and no longer change. This implies that the hardening function has reached the value of q/p^* as applied for the loading step considered. After this, the stress is increased to the next level. This procedure is depicted in Fig. 3.3. Hence it is assumed that the value of the hardening function at the end of a particular step is equal to the ratio q/p^*.

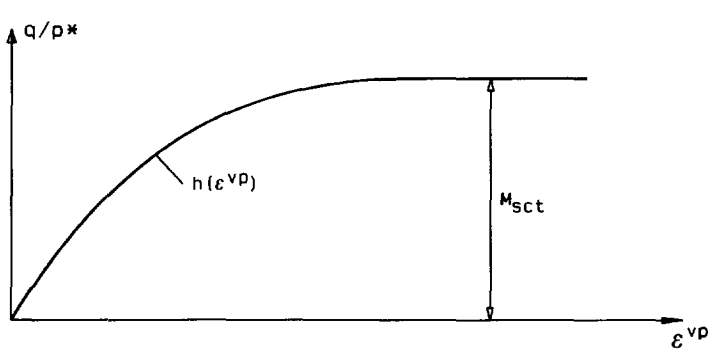

Fig. 3.2. Hardening function; first monotonically increasing then constant for $h(\varepsilon^{vp})=M_{sct}$.

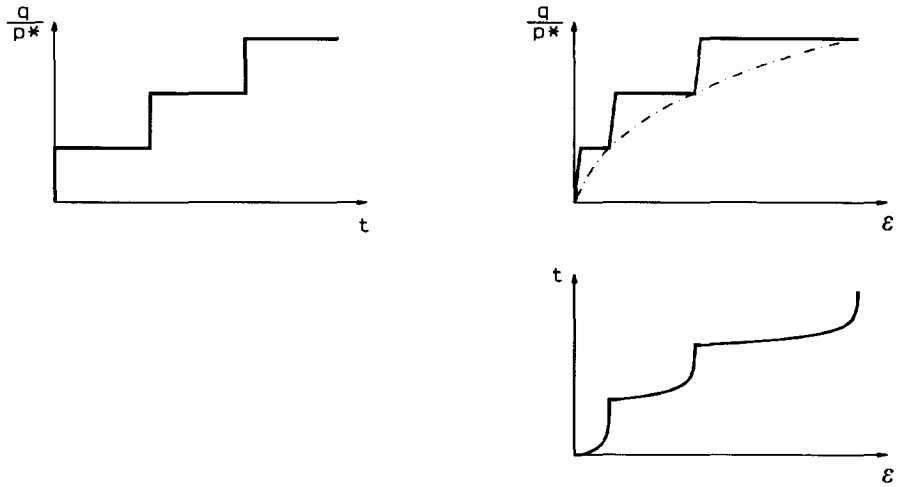

Fig. 3.3. Schematic representation of multiple-step creep test.

3.3 Analytical solution for multiple-step creep tests

For multiple-step creep tests we can also derive an analytical solution. To this end we consider a particular step. During this step we linearize the hardening function to obtain

$$h(\varepsilon^{vp}) = h(\varepsilon_0^{vp}) + H\Delta\varepsilon^{vp} \tag{3.11}$$

where

$$\Delta\varepsilon^{vp} = \varepsilon^{vp} - \varepsilon_0^{vp} \quad , \qquad H = \frac{h(\varepsilon_{max}^{vp}) - h(\varepsilon_0^{vp})}{\Delta\varepsilon_{max}^{vp}} \tag{3.12}$$

ε_{max}^{vp} is the creep strain at the end of the step considered, and ε_0^{vp} is the creep strain at the end of the previous step. A diagram of the procedure to determine the average hardening modulus H for a particular step is given in Fig. 3.4. Here we have plotted the creep strain on the horizontal axis and the stress ratio q/p^* on the vertical axis. For each particular step, the value of H is determined by dividing the stress ratio increment $\Delta(q/p^*)$ by the creep strain increment as illustrated in Fig. 3.4.

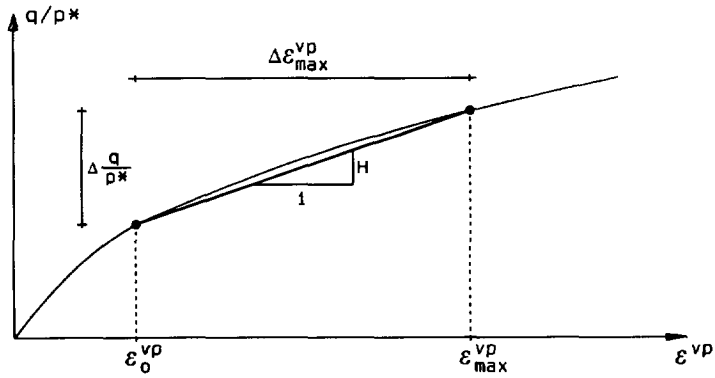

Fig. 3.4. Determination of average hardening modulus H for a particular step.

Using the linearization (3.11) to solve differential equation (3.10), we obtain for a particular step:

$$\Delta\varepsilon^{vp} = \frac{1}{H}\Delta\left(\frac{q}{p^*}\right)\left(1 - (1 + a\Delta t)^{-b}\right) \tag{3.13}$$

where

$$a = \frac{H}{\tau}(\beta-1)\,\Delta\left(\frac{q}{p^*}\right)^{\beta-1}, \qquad b = \frac{1}{\beta-1} \tag{3.14}$$

Note that Δt is the elapsed time for the loading step considered. The total strain increment is given by

$$\frac{\Delta\varepsilon}{\Delta\varepsilon_{max}} = 1 - \frac{E\cdot\Delta(q/p^*)}{H\cdot\Delta q+E\cdot\Delta(q/p^*)}\,(1 + a\Delta t)^{-b} \tag{3.15}$$

3.4 Verification by data from multiple-step creep tests

To be able to perform comparisons with test data, we performed a test where $\Delta(q/p^*)$ is approximately equal for each step. The values of H for each step are given in Table 3.1. In the table we used $\Delta\varepsilon^e = \Delta q/E$ for the elastic strains, with E = 300 MPa and a_{sct} = 200 kPa.

Table 3.1. Characteristics of multiple-step creep test, σ_3 = 300 kPa.

Step	q	p*	q/p*	Δ(q/p*)	ε_{max}	$\Delta\varepsilon_{max}$	$\Delta\varepsilon^{vp}_{max}$	H
	kPa				%			
1	49	516	0.095	0.095	0.125	0.125	0.108	87
2	99	533	0.186	0.091	0.261	0.136	0.119	76
3	149	550	0.271	0.085	0.456	0.195	0.178	48
4	199	566	0.351	0.080	0.700	0.244	0.227	35

For equal values of $\Delta(q/p^*)$ it is possible to present test data in the following way: On the horizontal axis we plot $H\Delta t$ and on the vertical axis we plot a normalized incremental strain $\Delta\varepsilon/\Delta\varepsilon_{max}$ with

$$\Delta\varepsilon_{max} = \frac{\Delta q}{E} + \frac{1}{H}\Delta\left(\frac{q}{p^*}\right) \tag{3.16}$$

This is done in Fig. 3.5. The solid lines represent test data. The dashed line uses equation (3.15) with β = 2.5. From Fig. 3.5 it can be seen that this curve for β = 2.5 exhibits close agreement between the test data and the analytical solution. Using the particular value of a/H corresponding to this curve we calculate τ = 1200 s from the equation

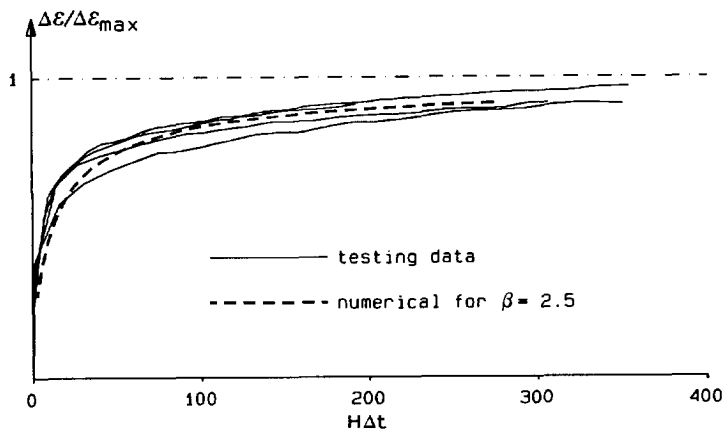

Fig. 3.5. Comparison of test data and analytical solution for a multiple-step creep test, σ_3 = 300 kPa, temperature 28 °C. Time in hours.

$$\tau = \frac{H}{a}(\beta-1)\,\Delta\left(\frac{q}{p^*}\right)^{\beta-1} \tag{3.17}$$

The above values of β and τ were used to predict test data for a different confining pressure of 100 kPa. For each step of the multiple-step creep test the value of the hardening modulus H was determined as shown in Table 3.2. When all values of β, τ, H, q and p^* are known it is possible to make Fig. 3.6. On the horizontal axis we plot the normalized time $a\Delta t$ where a is defined in (3.14), on the vertical axis we plot the normalized incremental strain $\Delta\varepsilon/\Delta\varepsilon_{max}$. Again it is found that we have close agreement between the test data and the analytical solution for $\beta = 2.5$ and $\tau = 1200$ s. This supports the present model.

Table 3.2. Characteristics of multiple-step creep test for $\sigma_3 = 100$ kPa.

Step	q	p*	q/p*	Δ(q/p*)	ε_{max}	$\Delta\varepsilon_{max}$	$\Delta\varepsilon^{vp}_{max}$	H
	kPa					%		
1	28	309	0.091	0.091	0.217	0.217	0.207	44
2	50	317	0.158	0.067	0.340	0.123	0.116	58
3	70	323	0.216	0.058	0.484	0.144	0.138	42
4	100	333	0.300	0.084	0.716	0.232	0.222	38

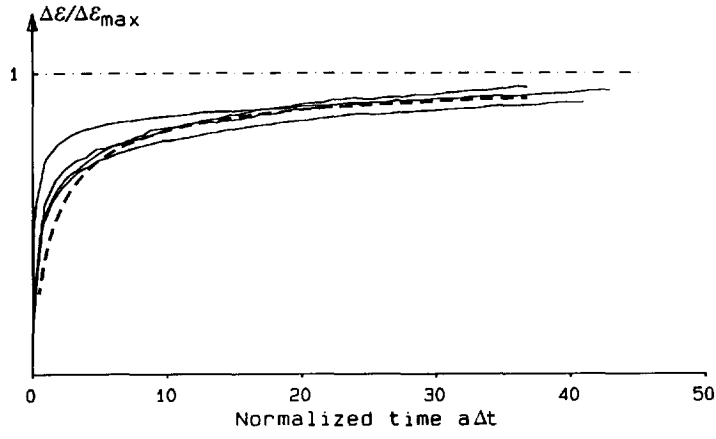

Fig. 3.6. Comparison of test data and analytical solution for a multiple-step creep test, $\sigma_3 = 100$ kPa, temperature 28 °C. Graph made using creep parameters from Fig. 3.5.

4. VERIFICATION OF HARDENING CONCEPT FOR PRIMARY CREEP

In Section 3.2 the hardening curve in Fig. 3.2 was determined on the basis of two multiple-step creep tests. Considering the limited number of tests, the idea of a hardening curve can, however, hardly be verified on the basis of test results. For this reason this concept will be examined extensively in this section, against the test results. Instead of multiple-step creep tests (Fig. 3.3) the results from stress-relaxation tests will be considered (Fig. 4.1). Considering the convex form of the hardening curve, stress-relaxation tests are most suited to the determination of this curve.

4.1 Determination of hardening function from stress relaxation tests

In stress-relaxation tests, at a constant deformation rate, a certain deformation is imposed. When this deformation has been reached, further deformation is inhibited. When applying the deformation, the stress will increase rapidly. If the deformation is kept constant, the stress will then decrease again until a certain constant value has been reached. If the stress is more or less constant, the procedure is repeated for successive deformation levels. The test is ended when the stress following relaxation is lower than in the previous step, because this is an indication of failure. A relaxation curve results from the stresses following relaxation; the dashed line in Fig. 4.1. This figure shows the process of a stress-relaxation test.

When applying deformation the stresses will increase rapidly. During the application, elastic strain in particular will occur and, to a lesser extent, visco-plastic creep. As soon as the deformation has been fixed the visco-plastic creep will continue to develop at the expense of the elastic strain. Total strain, therefore, remains constant, but an exchange takes place between the elastic contribution and the visco-plastic contribution. Because the elastic strain decreases, the stress will also decrease. At the end of this process, when the stress is constant, the elastic strain rate and therefore the visco-plastic strain rate will both have reached zero. Every stress-relaxation test produces several values for the stress following relaxation; relaxation takes place for various deformation levels. By interpolation we obtain a relaxation curve.

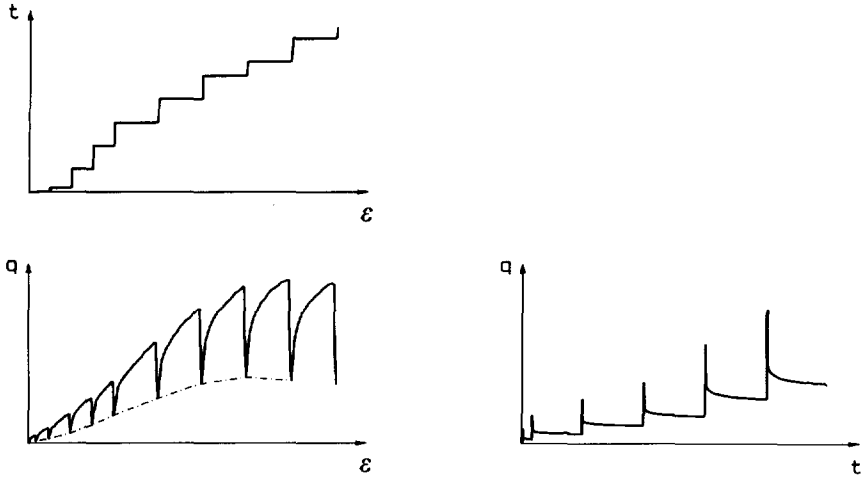

Fig. 4.1. Characteristic stress-relaxation test. (a) strain-time (input), (b) stress-strain and (c) stress-time.

The majority of stress-relaxation tests are carried out at a relatively high temperature of 28 °C, because the relaxation process then takes place rapidly. In order to give an indication of the times required, we can state that in the test shown in Fig. 4.1 each step took about 10 to 15 hours. The total time involved in the test amounted to a good 110 hours.

4.2 **Reproducibility of relaxation tests**

First of all, the reproducibility of the tests is examined. It has to be borne in mind here that the samples of bituminous concrete were taken from an existing dyke surface, with a thickness of 20 to 25 cm, taken from West-Kapelle in the South West of the Netherlands. These are samples that are 200 mm in height and 100 mm in diameter. This bituminous concrete comprises approximately 50 % gravel, two thirds of which with a diameter of more than 8 mm (see also the Appendix). Because this diameter is not small in relation to the diameter of the sample, a wide range in composition and in properties of the various samples is to be expected. This contrasts with samples created in the laboratory, where, for example, finer aggregate materials can be used (Di Benedetto, 1987).

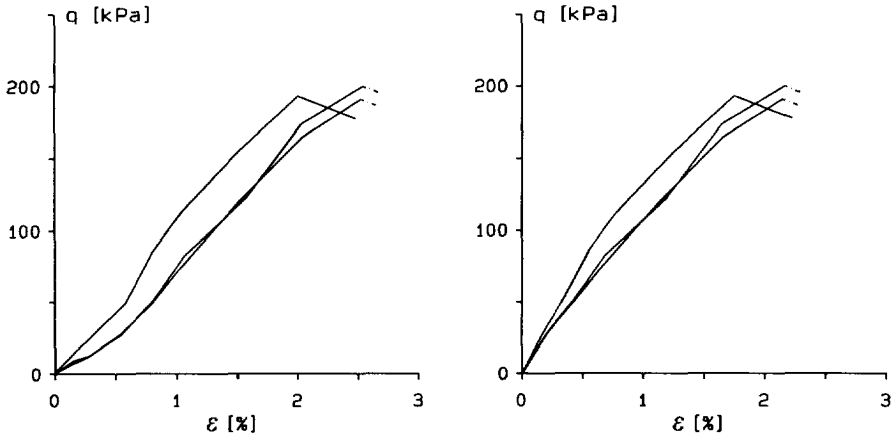

Fig. 4.2. Stress-relaxation tests. Temperature of 28 °C, confining pressure of 100 kPa and a deformation rate of $2.5 \cdot 10^{-3}$ s^{-1}. (a) Measured relaxation curves, (b) corrected relaxation curves.

Fig. 4.2 shows the relaxation curves for 3 identical tests. These are 3 tests with the same test temperature of 28 °C and a confining pressure of 100 kPa. The rate at which the deformation is applied is $2.5 \cdot 10^{-3}$ per second. This corresponds to a strain rate of 15 % per minute. It can be seen in Fig. 4.2a that the relaxation curves, apart from a limited starting phase, show the same characteristics; the slope and the maximum of the relaxation curves are approximately the same.

The discrepancies in the more or less concave starting range may have a number of causes. For instance, because the end faces are not entirely plan-parallel, whereby one side of the sample is, at the start, more heavily loaded. Another possibility is that initial cracks are pressed closed during the starting phase of the test. A correction was made for this discrepancy in the start-up phase; a new zero point for vertical strain was calculated. After correction of the data in Fig. 4.2a the curves in Fig. 4.2b result. We can see here that the relaxation curves for identical tests are, to a reasonable extent, in agreement. Considering the heterogeneity within the range of samples as mentioned above, this can be called good reproducibility.

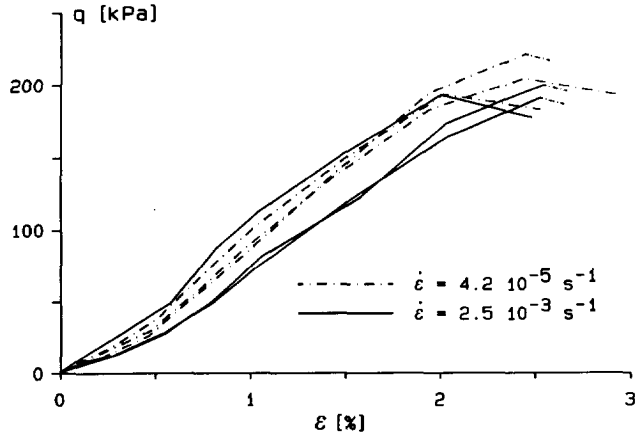

Fig. 4.3. Stress-relaxation tests. Temperature of 28 °C, confining pressure of 100 kPa and two deformation rates of $2.5 \cdot 10^{-3}$ and $4.2 \cdot 10^{-5}$ s^{-1}.

4.3 Influence of deformation rate on relaxation curve

The deformation rate has a great influence on the development of stresses before and during relaxation. With rapid deformation an almost exclusively elastic strain is created in the first instance ($\Delta\varepsilon^e$) and therefore a high peak stress, because $\Delta\sigma = E\Delta\varepsilon^e$. With slow deformation there is time for the development of creep ($\Delta\varepsilon^{vp}$) and proportionally less elastic strain will occur and therefore less stress will be built up. For an extremely slow deformation rate, one can expect the relaxation curve to be followed without any additional peak stresses and stress relaxation as shown in Fig. 4.1.

Fig. 4.3 shows the relaxation curves for tests in which different deformation rates have been used. This figure also shows approximately the same slope and maximum values for the relaxation curves. The solid lines in Fig. 4.3 are in accordance with those in Fig. 4.2a. The dashed lines in Fig. 4.3 were found for tests with a deformation rate of $4.2 \cdot 10^{-5}$ per second, in other words, a deformation rate that is sixty times smaller. Other tests, at a confining pressure of 300 kPa, hardly show any influence of the deformation rate on the relaxation curve. This means that the relaxation curve is not influenced by the rate at which the deformation is applied. In spite of very large

differences in the peak stresses before relaxation, it would appear that the deformation rate has no perceptible influence on the relaxation curve.

4.4 Influence of confining pressure on relaxation curve

Confining pressure has an obvious influence on the relaxation curves. With higher confining pressure the relaxation curve is steeper and the maximum is higher, at least if we plot the deviatoric stress $q = \sigma_1 - \sigma_3$ against the axial strain ε. This can be seen from the results of measurements for triaxial tests at various confining pressures σ_3. Fig. 4.4 shows the results of tests with σ_3 = 100, 300 and 500 kPa. From the various relaxation curves stresses can be determined that all give the same deformation and this has been done in Fig. 4.4 for three strain levels.

Data in Fig. 4.4 indicate that there is a relationship between the deformation level and the stress ratio q/p^*, where $p^* = p + a_{sct}$ with a_{sct} constant for all tests. The pseudo stress a_{sct} has already been covered in Sections 2.2 and 3.2. The relationship between ε and q/p^* was also introduced earlier under the name hardening function (eq. 3.11) or hardening curve.

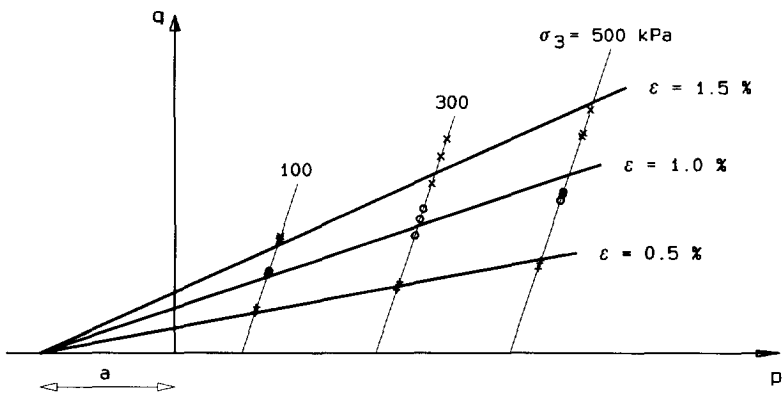

Fig. 4.4. Contours of deviatoric stresses after relaxation for different confining pressures of 100, 300 and 500 kPa and different deformation levels.

4.5 Formulation of hardening curve

Fig. 4.5 shows the normalized relaxation curves for relaxation tests with various confining pressures, in other words the measured relaxation curves have been normalized by dividing by $p^*=p+a_{sct}$. In fact several tests were carried out per confining pressure in order to assess reproducibility, but Fig. 4.5 shows, for each confining pressure, only one average curve, because the figure would otherwise become illegible. In total, 5 curves are shown, 2 of which relate to deformation rates of $4.2 \cdot 10^{-5}$ s^{-1} (confining pressures of 100, and 300 kPa). Three curves in Fig 4.5 are generated from the range of tests with a deformation rate of $2.5 \cdot 10^{-3}$ s^{-1} (confining pressures 100, 300 and 500 kPa). The relaxation curves have been normalized by incorporating a value of 200 kPa for a_{sct} in order to evaluate p^*. As can be seen from the figure, this normalization is a good way to describe a hardening curve. The formulation for equation (3.10) then follows:

$$\dot{\varepsilon}^{vp} = \frac{1}{\tau}\left(\frac{q}{p^*} - h(\varepsilon^{vp})\right)^{\beta} \quad ; \quad p^* = p + a_{sct} \tag{4.1}$$

where a_{sct} = 200 kPa.

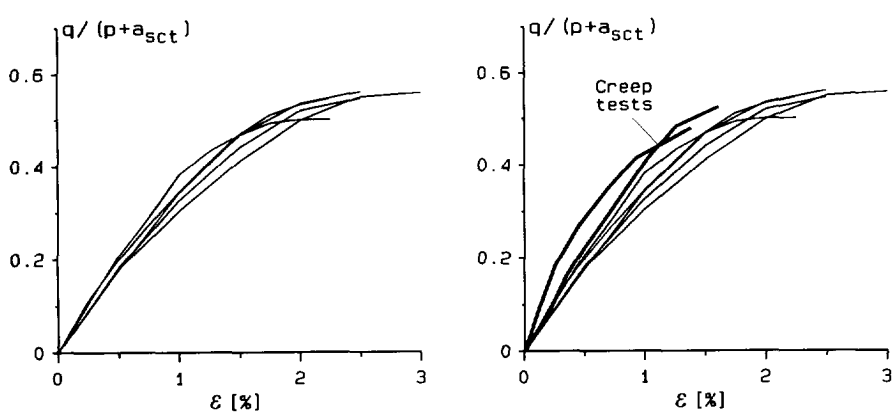

Fig. 4.5. Normalized relaxation curves or hardening curves; 2 curves for σ_3 = 100, 2 curves for σ_3 = 300 and 1 curve for σ_3 = 500 kPa. (a) From stress-relaxation tests and (b) includes measured data from multiple-step creep tests.

On the basis of relaxation tests we find practically the same hardening curve as with the multiple-step creep tests described in Section 3.2 . In Fig. 4.5b the creep-test curves are located a little above the relaxation test curves, but this is probably caused by the application of somewhat too short creep times in the 2 creep tests.

In order to obtain a complete constitutive model, a formulation for the data in Fig. 4.5 needs to be found. The curves in Fig. 4.5 can be described by various functions. In Section 3.2 the relaxation curves were applied multi-linearly. A smooth curve is suggested here:

$$h(\varepsilon^{vp}) = M_{sct} \frac{\varepsilon^{vp}}{\varepsilon_{sct}} \exp(1 - \varepsilon^{vp}/\varepsilon_{sct}) \qquad (4.2)$$

This exponential function has two parameters: the maximum value of the stress ratio (M_{sct}) to be achieved and the parameter ε_{sct} indicates at which creep strain the maximum is to be found. Hardening curves can be described well by M_{sct} = 0.55 and ε_{sct} = 0.03. These parameters were used for producing Fig. 4.6 where the formula (4.2) is compared with the test results. Formula (4.2) shows a decline after the peak. This decline is, however, only slight; for $\varepsilon^{vp} = 2\varepsilon_{sct}$ approximately 75 % of the maximum value M_{sct} still follows.

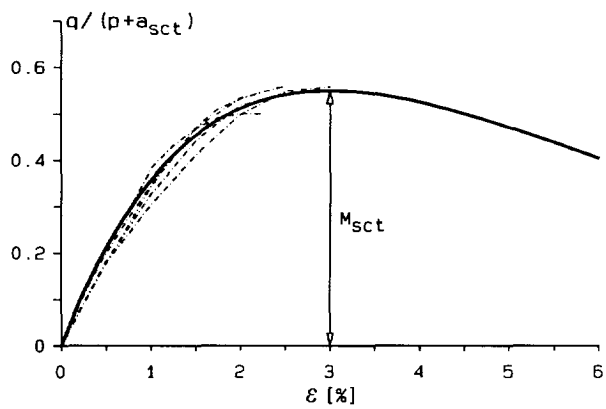

Fig. 4.6. Comparison of hardening function (4.2) and test data.

4.6 Results of extension relaxation tests

In Section 4.5, a formulation for the hardening curve was given. This formulation is based on triaxial compression tests; in other words $\sigma_1 \geq \sigma_2 = \sigma_3$ as has been considered until now. For extension tests with $\sigma_1 \leq \sigma_2 = \sigma_3$, the hardening function found earlier cannot be used without problem, as will be shown in this section.
In order to formulate a generally applicable model, it is necessary also to be able to describe extension tests. Therefore, extension tests were also carried out within the scope of this investigation. To this end, an extension of the sample is imposed after applying the cell pressure.

For triaxial compression tests, the axial pressure σ_1 is greater than the radial pressure and therefore $\sigma_1 \geq \sigma_2 = \sigma_3$ applies, at least if compression stresses are taken positive. The deviatoric stress $q = \sigma_1 - \sigma_3$ described in Section 2.2 is positive here. However, for triaxial extension tests, $\sigma_1 \leq \sigma_2 = \sigma_3$ applies. The result is, therefore, a negative deviatoric stress, q.

The relaxation curves for a number of triaxial extension tests were determined, as described in Section 4.1 for compression tests. They are set out in Fig. 4.7. The stress ratio $q/(p+a_{sct})$ and the strain have both been negatively plotted to indicate that extension tests are involved here. It can be seen in the figure that the shape of these curves is different from the shape of the relaxation curves from the compression tests (Fig. 4.5). After an initial rise in the relaxation curves, there is a flatter characteristic to the curves for the tests with a confining pressure of 100 kPa. These samples, therefore, fail at relatively modest "extension" stresses. Following an initial strong hardening, the tests with a confining pressure of 300 kPa show a fairly rapid softening, after a strain of approximately 0.5 % has been reached. At a relatively low stress ratio, failure is found again; in this case brittle failure, i.e. considerable softening. Generally speaking, this brittle behaviour would be expected at a more modest confining pressure of 100 kPa and not at this high confining pressure of 300 kPa.

A curve (thick line) has been plotted in Fig. 4.7 which makes use of formula (4.2), but then with a special value for M_{sct}. Compression tests on Delft bituminous concrete gave a value M_{sct} = 0.55, which amounts to a friction

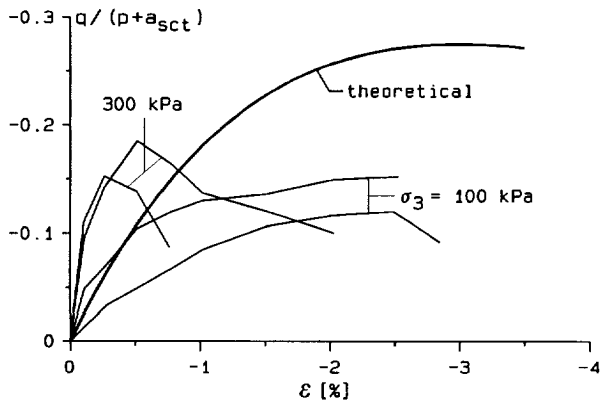

Fig. 4.7. Normalized relaxation curves from extension tests. Normalization using a_{sct} = 200 kPa, T = 28 °C.

angle of approximately 15°. Based on this M_{sct} value, the bold curve in Fig. 4.7 should give a peak value of 0.55. Of course with this value there is hardly any agreement with the measured results. Compression states and extension states of stress will, for that reason, not be dealt with in the same manner.

$$\text{Compression:} \quad \dot{\varepsilon}^{vp} = \frac{1}{\tau}\left(\frac{q}{p^*} - h(\varepsilon^{vp}) \right)^{\beta}$$

$$\text{Extension:} \quad |\dot{\varepsilon}^{vp}| = \frac{1}{\tau}\left(2\frac{|q|}{p^*} - h(\varepsilon^{vp}) \right)^{\beta} \tag{4.3}$$

in which

$$h(\varepsilon^{vp}) = M_{sct} \frac{|\varepsilon^{vp}|}{\varepsilon_{sct}} \exp(1 - |\varepsilon^{vp}|/\varepsilon_{sct}) \tag{4.4}$$

Contrary to equation (4.3a), the absolute value of the strain rate $\dot{\varepsilon}^{vp}$ is used in equation (4.3b). The most important difference between the compression state and the extension state of stress concerns the factor 2 for the stress ratio. It will be shown in Section 7.4 that an isotropic model can be described with the equations (4.3). For a factor higher than 2 in equation (4.3b), it is no longer possible to describe an isotropic model.

A possible explanation for the modest strength in extension tests in Fig. 4.7 is that homogeneous stresses and deformation are assumed. This is perhaps not an acceptable assumption for extension tests. In the first instance, it may occur that with a non-homogeneous stress distribution at micro level, tensile stresses occur, whereas on average a compression stress dominates. These local tensile stresses may give rise to micro cracks whereby part of the surface is no longer involved. In the second instance, the effect of the weakest link applies here. If a particular section is weaker or becomes weaker than the rest, the strain can be concentrated. This can be compared to the occurrence of necking in a tension test on steel. When carrying out the tests, the strain is determined by dividing the total extension by the height of the sample, whereby any localisation of strain will not be apparent in the measured results. Non-uniform deformation can only be measured by means of local strain measurements in a number of locations in the sample, which is something that did not take place.

It appears from the measured relaxation curves in Fig. 4.7 that the extension tests are poorly reproducible. This is in contrast to the compression tests dealt with in earlier sections. Just as with the modest strength, this may perhaps be related to the occurrence of micro cracks at an early stage in an extension test, but there are no conclusive indications of this.

4.7 Relaxation tests without confining pressure

In Section 4.5, a formulation was given for the hardening curve. This function is based on triaxial compression tests with confining pressure. However, in compression tests without confining pressure, lower relaxation stresses are found; not only absolutely lower stresses, but also following normalization. N.B. in normalization, deviatoric stress is divided by $p^*=p+a_{sct}$, where the same value of a_{sct} is taken for extension states of stress as described in Section 4.6 and for compression states of stress with and without confining pressure. This is shown in Fig. 4.8 where both the results of compression tests with confining pressure as well as results of compression tests without confining pressure are plotted.

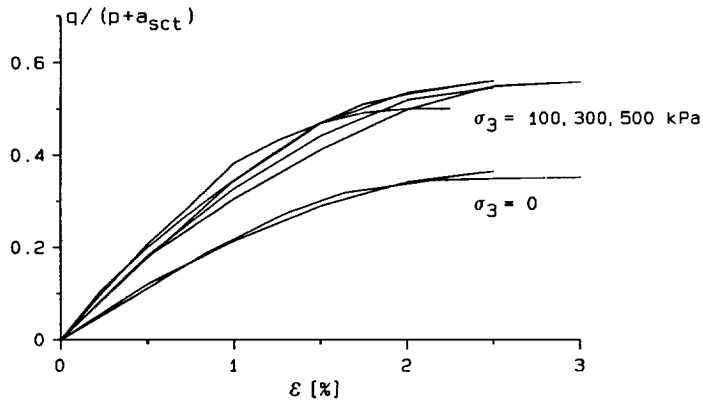

Fig. 4.8. Normalized relaxation curves from compression tests with different confining pressures; a_{sct} = 200 kPa, T = 28 °C.

It can be seen in the figure that the shape of the curves with and without confining pressure is the same, but the tests without confining pressure show a maximum value for the hardening function which is approximately two thirds of the maximum value from the tests with confining pressure.

Therefore, the uniaxial compression tests with $\sigma_2=\sigma_3=0$ cannot be described with equation (4.2) and this formulation needs, therefore, to be adapted. We continue to assume the equations

$$\text{Compression:} \quad \dot{\varepsilon}^{vp} = \frac{1}{\tau}\left(\frac{q}{p^*} - h(\varepsilon^{vp},p) \right)^{\beta}$$

$$\text{Extension:} \quad |\dot{\varepsilon}^{vp}| = \frac{1}{\tau}\left(2\frac{|q|}{p^*} - h(\varepsilon^{vp},p) \right)^{\beta} \tag{4.5}$$

$$h(\varepsilon^{vp},p) = M^*_{sct} \frac{|\varepsilon^{vp}|}{\varepsilon_{sct}} \exp(1 - |\varepsilon^{vp}|/\varepsilon_{sct}) \tag{4.6}$$

But in contrast to equation (4.4) we now define M^*_{sct} as

$$M^*_{sct} = M_{sct} \left(1 - e^{-(p+p_1)/p_2} \right) \tag{4.7}$$

The term with p_1 and p_2 is new. For high values of p this term loses its influence and we find $M^*_{sct} = M_{sct}$. But for low values of p there is a clear influence.

In the p-q plane, the formulation according to equations (4.5) to (4.7) results in curved lines for $\dot{\varepsilon}^{vp} = 0$. We find a series of flow areas for various values of ε^{vp}. The failure surface for Delft bituminous concrete is shown in Fig. 4.9. The curved lines are in accordance with equations (4.5) to (4.7); the straight dashed lines give the original Mohr-Coulomb lines without the adjustment according to equation (4.7). The points in the figure give the maximum relaxation stresses for the compression tests and for the extension tests. As commented earlier, the strength of the extension tests with confining pressure is overestimated.

The failure surface of Fig. 4.9 can be found with $\varepsilon^{vp} = \varepsilon_{sct}$. In this case $h(\varepsilon^{vp}, p)$ reduces to M^*_{sct} and with $\dot{\varepsilon}^{vp}=0$ gives equation (4.5a) for compression states of stress

$$\frac{q}{p^*} = M^*_{sct} = M_{sct}\left(1 - e^{-(p+p_1)/p_2}\right) \qquad \text{for } \dot{\varepsilon}^{vp}=0,\ \varepsilon^{vp}=\varepsilon_{sct} \tag{4.8}$$

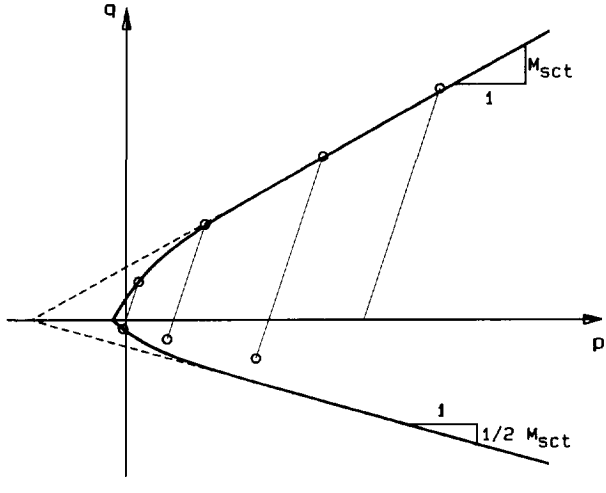

Fig. 4.9. Comparison of test data and adapted yield function according to equations (4.5)-(4.7).

The parameter p_1 determines the point of intersection of this curved surface with the p-axis. The parameter p_2 determines the extent of curvature for low stresses. The values of the parameters p_1 and p_2 follow by fitting the test results. It is first of all assumed for this that $M^*_{sct} \simeq M_{sct}$ applies to the compression tests with high confining pressure. The coefficients can be determined on the basis of the tests without confining pressure. On the compression side (q>0 in Fig. 4.9) we have a result available from the uniaxial compression tests. On the extension side (q<0 in Fig. 4.9) data from uniaxial extension tests are available.

On the basis of these two data, two stress combinations follow to which formula (4.7) should conform. These stress points in Fig. 4.9 are $(p,q) = (\frac{1}{3}\sigma_c,\ \sigma_c)$ and $(-\frac{1}{3}\sigma_t,\ -\sigma_t)$ where σ_c and σ_t are the maximum (absolute) relaxation stresses of compression and extension tests without confining pressure, respectively. The values of p_1 and p_2 can be expressed in the values σ_t and σ_c. On the basis of the values for σ_t and σ_c, values for M^*_{sct} can be calculated; i.e. M^t_{sct} for uniaxial extension and M^c_{sct} for uniaxial compression.

Uniaxial tension: $$M^*_{sct} = M^t_{sct} \equiv \frac{6\sigma_t}{3a_{sct} - \sigma_t}$$

Uniaxial compression: $$M^*_{sct} = M^c_{sct} \equiv \frac{3\sigma_c}{3a_{sct} + \sigma_c}$$

After some manipulation using equation (4.7) there follows

$$p_2 = \frac{1}{3}\ \frac{\sigma_t + \sigma_c}{\ln\left(\dfrac{M_{sct} - M^t_{sct}}{M_{sct} - M^c_{sct}}\right)} \tag{4.9}$$

and

$$p_1 = -\,p_2 \ln\left(1 - \frac{M^t_{sct}}{M_{sct}}\right) + \frac{1}{3}\sigma_t \tag{4.10}$$

In order to calculate p_1 and p_2, sufficient data should be available and the value for a_{sct} in particular is necessary for determining M^t_{sct} and M^c_{sc} and then the value for M_{sct} is used to determine p_1 and p_2.

At a temperature of 28 °C we measure for Delft bituminous concrete

$$\sigma_c = 80 \text{ kPa}, \quad \sigma_t = 18 \text{ kPa},$$
$$a_{sct} = 200 \text{ kPa}, \quad M_{sct} = 0.55,$$
$$\varepsilon_{sct} = 0.03$$

By using equations (4.9) and (4.10) it then follows that

$$p_1 = 28 \text{ kPa}, \quad p_2 = 53 \text{ kPa}.$$

By using these values it appears that for the compression tests with a confining pressure $\sigma_3 = 100$ kPa we find with equation (4.8) that $M^*_{sct} = 0.98\ M_{sct}$ is obtained. The term with p_1 and p_2 in equation (4.8) has, therefore, hardly any influence at all on the confining pressures of 100 kPa and higher.

In Fig. 4.10 the hardening function according to equations (4.6) and (4.7) is plotted for compression tests with the parameters of Delft bituminous concrete as stated above. The thin continuous lines give the test results for uniaxial compression tests. For the tests it is not the relaxation stress q/p^* that has been plotted as a function of ε^{vp}, but the stress function

$$\frac{q/p^*}{1 - \exp(-(p+p_1)/p_2)} \tag{4.11}$$

The thick continuous line follows directly from equation (4.6) with $M^*_{sct} = M_{sct}$. The dashed lines give the results of compression tests with confining pressure. As can be seen in this figure, the results of compression tests can now be described well using the hardening formulation according to equations (4.6) and (4.7).

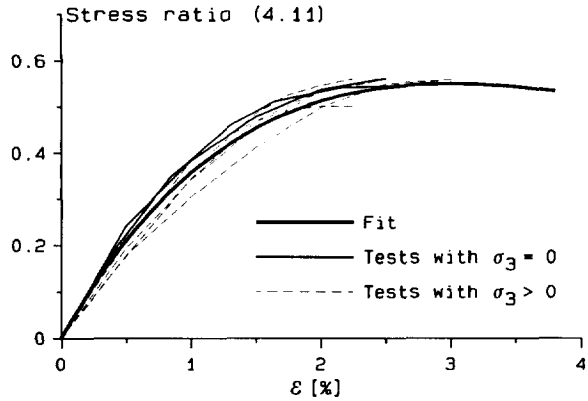

Fig. 4.10 Stress ratios according to eq. (4.11) from triaxial compression tests.

It appears from the above that in order to determine the visco-plastic behaviour of bituminous concrete, a number of triaxial tests are required. In order to determine the behaviour with both low and high confining pressures, three compression tests are necessary, for example at confining pressures of 0, 100 and 300 kPa. A tension test is then required in order to determine the tensile strength. The compression tests with σ_3 = 100 kPa and σ_3 = 300 kPa are required in order to determine a_{sct} and M_{sct}. The uniaxial tension and compression tests give σ_t and σ_c and then the constants p_1 and p_2. In this the uniaxial compression strength must meet the condition

$$\sigma_c \leq \frac{3M_{sct}a_{sct}}{3 - M_{sct}} \tag{4.12}$$

This is in accordance with the condition that $M^t_{sct} \leq M_{sct}$. This is because otherwise the equations (4.9) and (4.10) could not be solved for p_1 and p_2. The restriction on σ_c is a convexity condition for the flow surface; plotted in the p-q plane this should give a failure point below the Coulomb line, as determined by a_{sct} and M_{sct}. For certain mixtures (Di Benedetto, 1987) the compression test gives a stress point that is more or less on the Coulomb line. In such a case, the value can be reduced by one or two percent in order to obtain a sufficiently convex flow area.

5. VISCO-ELASTIC BEHAVIOUR

In the previous chapters the visco-plastic creep was covered. That is, the time dependent irreversible strain. Generally speaking, a model for visco-plasticity is required for the description of fairly large strains as they occur at high loads and for long periods of load time. The visco-plastic creep model is not sufficient for an accurate description of the material behaviour for small strains or short load times. For this reason, this chapter will give more details of an improved approach to the behaviour for short and/or small loads. This improved approach is obtained by taking into account the visco-elastic behaviour.

5.1 Visco-elasticity in the classical formulation

The origin of the term visco-elasticity lies in the simple models combining elastic and viscous elements. Classical examples of such models are the Maxwell model and the Kelvin-Voigt model as illustrated in Fig. 5.1. In general, all models combining elastic springs and viscous dashpots are referred to as visco-elastic. For materials whose behaviour is linearly visco-elastic there is linearity between load and deflection; doubling the loads will give doubling of the deformations, but the linear relation depends on a third parameter, i.e. time. In other words, the rate of deformation affects the stress and vice versa. In general, the current state of the material cannot be determined completely unless the entire history of loading is known; the material remembers the entire past.

The classical definition (Zener, 1948; Fung, 1965; Schapery, 1974; Ferry, 1980) is that a material reacts in a linear visco-elastic way if the constitutive equation can be written in the form

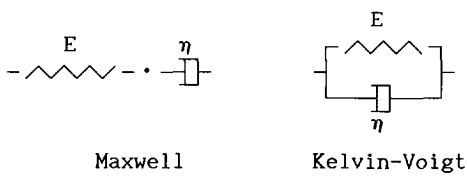

Fig. 5.1. Basic visco-elastic models.

$$\varepsilon^{ve}(t) = \int_{-\infty}^{t} c(t-\tau) \frac{d\sigma}{d\tau} d\tau \tag{5.1}$$

or in the inverse relationship

$$\sigma(t) = \int_{-\infty}^{t} k(t-\tau) \frac{d\varepsilon^{ve}}{d\tau} d\tau \tag{5.2}$$

The type of relation connecting input and response in these equations is called a hereditary law. A superscript ve is used for the strain in order to make a distinction with the irreversible strain ε^{vp} as described earlier. The function $c(t)$ is called the creep function. This function describes the strain due to a unit stress applied at t=0. Hence this function can be measured in a constant-stress creep test. Similarly, the relaxation function $k(t)$ can be used. This relaxation function describes the evolution of stress due to a unit strain applied at t=0. Hence $k(t)$ can be measured in a constant-strain relaxation test.

Within the classical definition of visco-elasticity both reversible strains and irreversible strains are taken into account by means of the function $c(t)$ or the function $k(t)$. Ferry (1980) makes a distinction between visco-elastic liquids and visco-elastic solids. The difference between them relates to long term behaviour and will be explained by means of the creep and relaxation functions. If a material behaves as a visco-elastic liquid, an ongoing deformation will occur under a constant stress; in other words, the creep function is unlimited. If a constant strain is applied to this material, the stress will disappear entirely by relaxation; the relaxation function tends to zero. For a material that behaves as a visco-elastic solid, the creep function is limited; no continuing strain occurs. The relaxation function for this material decreases to a certain value, not zero. With a visco-elastic liquid we are (also) dealing with irreversible strains, but with a visco-elastic solid it is only reversible strains that occur. The use of such concepts as visco-elastic liquid and visco-elastic solid is not a bad use, but we would prefer the terminology visco-elastic solid (only reversible strains) and visco-plastic solid (only irreversible strains). Bituminous concrete is neither a visco-elastic solid, nor a visco-plastic solid, because, under load both reversible and irreversible strains may occur.

From equations (5.1) and (5.2) one can see that there is linearity between the stress and strain, because the creep function and the relaxation function do not depend on the stress. For using equation (5.1) it is necessary that the stress is a continuous function of time. Similarly the strain in equation (5.2) must be continuous with respect to time. However, it is possible to adapt the above formulas to include discontinuous step functions for stress or strain (Fung, 1965).

A visco-elastic model on the basis of convolution integrals as given by the equations (5.1) and (5.2) is less suitable for use in a finite element program for solving practical problems numerically. When solving boundary value problems it is currently well possible to solve the stress-strain relationships of the form $\dot{\sigma}=f(\sigma,\varepsilon,\dot{\varepsilon})$, but equations (5.1) and (5.2) cannot be written in this way. The rate of stress is here not only a function of current stresses and strains, but also of the history of those variables in the past. For every material element the complete stress and strain history would have to be stored in a computer program. From a practical point of view this is not feasible, and there have been up until now still no finite element programs with stress-strain relationships based on equations (5.1) or (5.2).

5.2 Visco-elasticity using spring/dashpot models

As already stated, visco-elastic models generally require the storage of the entire deformation history. By using special creep or relaxation functions we do, however, arrive at a numerically manageable model. Starting with special relaxation functions one arrives in that case at a so-called parallel chain of Maxwell elements as indicated in Fig. 5.2a (De Borst, 1984). Starting with special creep functions one arrives at a series of Kelvin-Voigt elements as indicated in Fig. 5.2b.

For the formulation of the visco-elastic behaviour of bituminous concrete special creep functions will be assumed (see also Schapery, 1974; Argyris, 1976, 1977). In that case we use a Dirichlet expansion of the creep function in the form

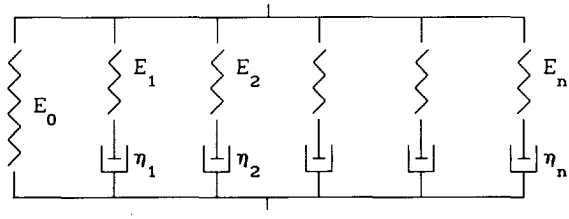

Generalized Maxwell model

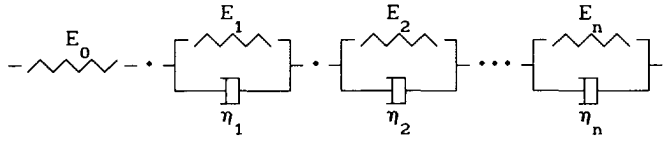

Generalized Kelvin-Voigt model

Fig. 5.2. Generalized models for visco-elastic solids.

$$c(t) = \frac{1}{E_0} + \sum_{i=1}^{n} \frac{1}{E_i} \left(1 - e^{-\frac{E_i}{\eta_i} t} \right) \tag{5.3}$$

By taking this function, the response to a creep test can be described as follows. An instantaneous strain takes place due to the term $1/E_0$ and a strain that increases with time due to the negative e-powers. The strain does, however, remain finite and that renders this formulation suitable for describing a visco-elastic solid. If the number of terms in (5.3) is sufficiently high the creep function is described sufficiently. By substituting equation (5.3) in equation (5.1) there follows

$$\varepsilon^{ve}(t) = \int_{-\infty}^{t} \left(\frac{1}{E_0} + \sum_{i=1}^{n} \frac{1}{E_i} \left(1 - e^{-\frac{E_i}{\eta_i}(t-\tau)} \right) \right) \frac{d\sigma}{d\tau} d\tau \tag{5.4}$$

Equation (5.4) can be used to calculate the time derivative of the strain. If the derivative of both sides of equation (5.4) is taken then, after some manipulation, there follows

$$\dot{\varepsilon}^{ve}(t) = \frac{\dot{\sigma}(t)}{E_0} + \sum_{i=1}^{n} \dot{\varepsilon}_i^{ve}(t) \tag{5.5}$$

where

$$\dot{\varepsilon}_i^{ve}(t) = \frac{\sigma(t)}{\eta_i} - \frac{E_i}{\eta_i}\varepsilon_i^{ve}(t) \tag{5.6}$$

The evolution of ε_i^{ve} can be determined numerically on the basis of the integration scheme

$$\varepsilon_i^{ve}(t) = \varepsilon_i^{ve}(t-\Delta t) + \int_{t-\Delta t}^{t} \dot{\varepsilon}_i^{ve}(\tau)\, d\tau \tag{5.7}$$

From this it appears that for the special option (5.3) of the creep function (5.1) the relatively simple equations (5.5) to (5.7) have been obtained. Instead of the entire stress or strain history we now only need to keep track of the internal variables ε_i^{ve} and to update them when performing calculations. By means of the Dirichlet approach to the creep function the integral equation (5.1) degenerates into a rate-type equation (5.5). Equations (5.5) - (5.7) are also obtained if a Kelvin-Voigt series is assumed, as given in Fig. 5.2b, where E_i and η_i are the spring stiffness and the viscosity of an element respectively. The strain component ε_i^{ve} stands for the strain of a Kelvin-Voigt element. By including sufficient Kelvin-Voigt elements, a realistic approach to linear visco-elasticity can be obtained.

5.3 **Response to sinusoidal loading**

It is interesting to obtain the relationship between load and deflection when a body is forced to perform simple harmonic oscillations. Indeed such tests are often performed by road engineers to asses the performance of bituminous concrete under cyclic loads. We are interested in the steady state response. Hence we assume that a sinusoidal stress acts on the body for a long period of time. This implies that initial disturbances have died out.

Here we will restrict ourselves to the response of a Kelvin-Voigt series model. For these models it follows that a sinusoidal stress will result in a sinusoidal strain. For the stress we write

$$\sigma = \hat{\sigma} \sin \omega t \tag{5.8}$$

where $\hat{\sigma}$ is the amplitude of the stress and ω the circular frequency which is related to the frequency f of loading

$$\omega = 2\pi f \tag{5.9}$$

In general there is a phase lag (δ) between the stress and strain. For the strain we write

$$\varepsilon = \hat{\varepsilon} \sin(\omega t - \delta) \tag{5.10}$$

The strain of a Kelvin-Voigt series model is composed of individual contributions of each single Kelvin-Voigt element; $\varepsilon_i^{ve} = \hat{\varepsilon}_i^{ve} \sin(\omega t - \delta_i)$ where

$$\frac{\hat{\sigma}}{\hat{\varepsilon}_i^{ve}} = \sqrt{E_i^2 + \eta_i^2 \omega^2} \quad ; \quad \delta_i = \arctan\left(\frac{\eta_i \omega}{E_i}\right) \tag{5.11}$$

For the total chain we find

$$E_c^2 \equiv \left(\frac{\hat{\sigma}}{\hat{\varepsilon}}\right)^2 = \frac{1}{\left(\sum_{i=0}^{n} \frac{\eta_i \omega}{E_i^2 + \eta_i^2 \omega^2}\right)^2 + \left(\sum_{i=0}^{n} \frac{E_i}{E_i^2 + \eta_i^2 \omega^2}\right)^2} \tag{5.12}$$

and

$$\delta = \arctan\left(\frac{\sum_{i=0}^{n} \eta_i \omega / (E_i^2 + \eta_i^2 \omega^2)}{\sum_{i=0}^{n} E_i / (E_i^2 + \eta_i^2 \omega^2)}\right) \tag{5.13}$$

The ratio $\hat{\sigma}/\hat{\varepsilon}$ is usually referred to as the complex modulus. A theoretically better name would be: the modulus of the complex modulus. The complex modulus is in fact defined as the relationship between the stress and the strain σ/ε. By using the formula given above for the ratio $\hat{\sigma}/\hat{\varepsilon}$, which for convenience will be indicated further as the complex modulus E_c, we shall look at how various models behave under harmonic loads. In addition to the simple models of Maxwell and Kelvin-Voigt, as shown in Fig. 5.1, the Burgers model, the Zener model (Fig. 5.3) and a Kelvin-Voigt series model will also be covered.

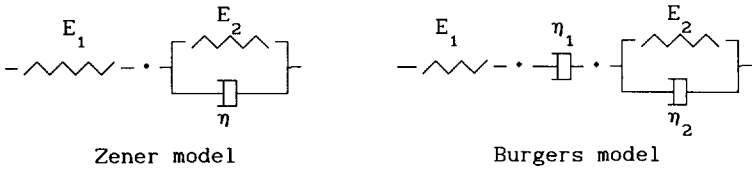

Fig. 5.3. The Zener model and the Burgers model.

The Burgers model and the Zener model can easily be derived from the general Kelvin-Voigt series model by including a limited number of elements and then by setting a number of parameters equal to zero. By doing this one obtains the single spring in the Zener model by immediately setting the viscosity to zero. The single dashpot in the Burgers model is obtained by taking the spring stiffness E of a Kelvin-Voigt element equal to zero.
The (modulus of the) complex modulus for these models is plotted against the imposed frequency in Fig. 5.4.

Fig. 5.4 does, of course, give only a rough idea of the response. By varying the parameters the response can be influenced. By proportionally increasing all stiffnesses, the curve shifts upwards and higher complex moduli are obtained. By proportionally increasing the viscosities, the curve shifts to

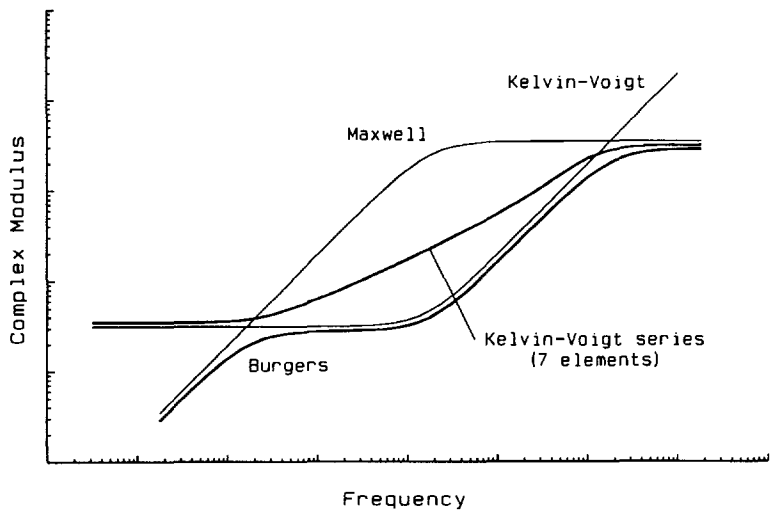

Fig. 5.4. Response to harmonic oscillations for different models.

the left, and a lower frequency now applies to the same modulus. For the response to the Kelvin-Voigt series model (7 elements, of which one is without dashpot) use is made of increasing elastic moduli. Increasing moduli are thus chosen for the various springs. This increase is taken to be exponential. Between two springs there is, for example, a factor 2 in stiffness. The separate spring has the highest stiffness, this spring determines the height of the right hand horizontal asymptote in Fig. 5.4. Because no separate dashpot has been included, the serial model gives a horizontal asymptote on the left hand side. The value of this asymptote follows simply from equation (5.12) as

$$\omega \approx 0 : \quad \frac{\hat{\sigma}}{\hat{\varepsilon}} = \frac{1}{\sum_{i=0}^{n} 1/E_i} \tag{5.14}$$

If the asymptotes of the S-curve are known, for a given number of Kelvin-Voigt elements, the ratio between the successively higher elements can be determined. The value of E_0 follows from the right hand asymptote. Formula (5.14) gives the left asymptote E_∞ for ω=0. If between two consecutive springs it applies that $E_{i+1} = E_i/\alpha$ with α>1 then it follows from (5.14)

$$E_\infty = \frac{E_0}{1+\alpha+\alpha^2+..+\alpha^n} = \frac{\alpha-1}{\alpha^{n+1}-1} E_0 \tag{5.15}$$

By using this equation, by trial and error or by iteration, the relationship α between two consecutive springs is obtained if the number of springs and the relationship between E_0 and E_∞ are known.

In the simple models, such as the Maxwell model and the Kelvin-Voigt model, a slope of 1:1 follows for the slope in the frequency-complex modulus curve, at least in that part of the frequency area where the spring no longer has any influence. In the Zener model and the Burgers model the same slope follows the bending point of the S-shaped curve. In tests on bituminous concrete, a slope is often to be found of approximately 1:2 to 1:3 on a log-log scale. For the serial model the slope of the line may be influenced by also taking the viscosities, just as the spring stiffnesses, exponentially. However, for a lower stiffness modulus of an element, a higher viscosity should be chosen.

In this way for a model with 7 Kelvin-Voigt elements, a slope of 1:2 is obtained as given in Fig. 5.4. Here the ratio between two consecutive viscosities has been taken equal to 2.

5.4 From a simple Zener model to a Kelvin-Voigt series model

From a scientific point of view, a model should be able to describe well the response within the entire frequency range. When applying a model for calculations to practical situations, it is usually sufficient to approximate the response to sinusoidal loads in only a limited frequency range. This means that a model with a limited number of parameters can be selected. This will be explained here by referring to the simple Zener model. The Zener model is in fact a Kelvin-Voigt series of 2 elements in which one element degenerates to a single spring.

In the Zener model we have three parameters, one separate spring, one parallel linked spring and a parallel linked dashpot. For simplicity, the relative stiffnesses are indicated here as E_e , E_{ve} and η_{ve} respectively. Because there are three parameters, we are able to approach the complex modulus for three different frequencies accurately. By using the general equation (5.12) for the Zener model for the complex modulus we obtain

$$E_c^2 \equiv \left(\frac{\hat{\sigma}}{\hat{\varepsilon}}\right)^2 = \frac{E_e^2\,(E_{ve}^2 + \eta^2\omega^2)}{(E_e+E_{ve})^2 + \eta^2\omega^2} \qquad (5.16)$$

If tests are now carried out for three frequencies f_1 , f_2 and f_3 ($\omega_i = 2\pi f_i$), three moduli E_{c1} , E_{c2} en E_{c3} follow. With these data the stiffnesses and the viscosity can be chosen such that the response function passes exactly through the three frequency and modulus combinations. If the frequency range for which fitting is to occur is not too large, a good approximation to the complex modulus is obtained in this frequency range with the Zener model. This will be demonstrated by referring to test results on bituminous concrete.

Terrel et al. (1973) describe tests, including cyclical tests, on bituminous concrete samples with various compositions. Samples of three different

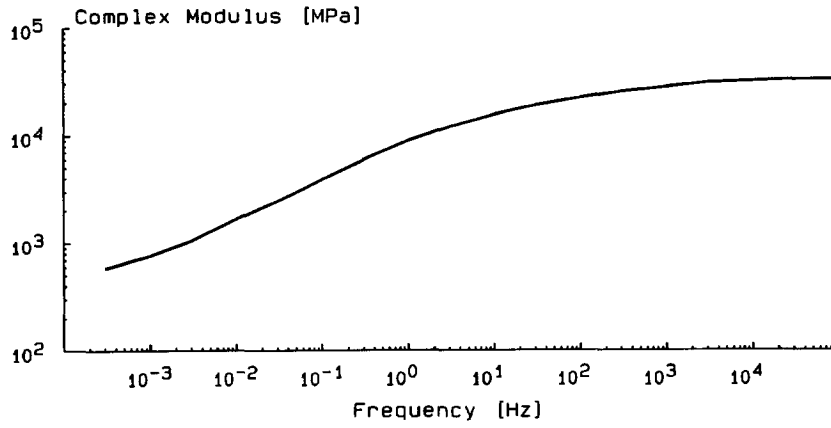

Fig. 5.5. Results for Complex Modulus at different frequencies (after Terrel et al.). Reference temperature of 21 °C, bitumen content of 3.5 %, medium gradation of aggregate.

bitumen levels and three different aggregate materials were tested. It was ensured in the cyclical tests that pressure on the sample was always maintained. In other words, both a constant stress and a sinusoidal stress were applied. The stress level varied from 70-350 kPa.

Fig. 5.5 shows the results for a sample with a bitumen level of 3.5 % and an average gradation of the aggregate. The frequencies are linked to reference temperature of 21 °C (see also Chapter 6).

For the maximum slope of the curve in Fig. 5.5 a value of approximately 1:2.5 is found. It remains salient that this maximum slope varies somewhat with the bitumen content. For a low content of 2.5 % Terrel finds a relatively small slope of 1:3 and for a high content of 4.5 % a slope of 1:2.

If fitting is performed at discrete intervals of the curve in Fig. 5.5, where a factor 100 between the extreme frequencies is assumed, the parameters from Table 5.1 are obtained for the Zener model. The factor 100 in the frequency interval corresponds approximately to the transition area in the Zener model with a ratio of 10 between the spring stiffnesses; the response of the Zener model in this range runs from the minimum modulus to the maximum modulus. Outside this range the modulus is practically constant. The response

Table 5.1. Parameters for Zener model from fit on data in Fig. 5.5.

Fit	Frequency range [Hz]	E_e [GPa]	E_{ve} [GPa]	η [GPa·s]
1	$10 - 10^3$	30	30	0.08
2	$10^{-1} - 10$	15.5	5	2.5
3	$10^{-3} - 10^{-1}$	4	0.9	31

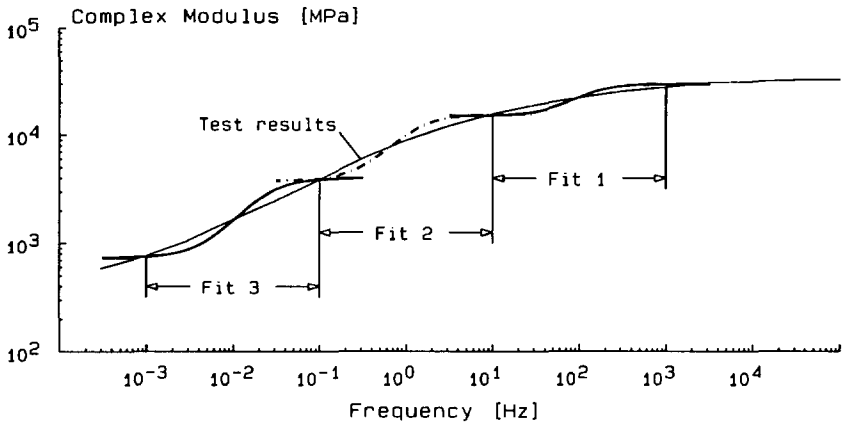

Fig. 5.6. Three fits to Terrels test data in different frequency ranges using the Zener model.

functions for three fits for different frequency ranges are set out in Fig. 5.6 together with the original data.

The parameters in Table 5.1 can be used for a Kelvin-Voigt series with 4 elements. The parameters for this 4 element model are given in Table 5.2. This 4-element model shows approximately the same discrepancies with respect to the S-curve as the discrete fits in their limited frequency range. The difference with the Zener models is that a reasonable fit can be obtained over a range of approximately 10^{-3} to 10^3.

Table 5.2. Parameters for 4-element (7-parameter) Kelvin-Voigt series model.

	0	1	2	3	
E_i	30	30	5	0.9	[GPa]
η_i	-	0.08	2.5	31	[GPa•s]

It is of course possible to fit a model for a smaller frequency range, with, for example, a factor 10 instead of 100. The test results within this limited interval will then of course be more closely approximated. If the whole experimental S-curve is approximated with a Kelvin-Voigt series model with 8 elements and therefore 15 parameters, the model will virtually follow the experimental S-curve.

5.5 Determination of visco-elastic properties of Delft bituminous concrete

In the previous sections a description was given for the visco-elastic behaviour of bituminous concrete. In this section, by referring to data, an attempt will be made to find the parameters for Delft bituminous concrete. No complete S-curve is available for this bituminous concrete. Part of the data available comes from cyclical tests (Montauban, 1988) that were carried out on bituminous concrete from a test strip near West-Kapelle, near to where samples were taken for the stress-relaxation tests and the creep tests. The other results are taken from repeated-loading tests (Fig. 5.8).

The cyclical tests involve data from four point bending tests on beam shaped samples. The samples were loaded by a cyclical imposed movement. The force required is measured and a complex modulus is determined from the data. The temperature varies between 0 °C and 20 °C, the loading frequency varies from 5 Hz to 50 Hz. Further, samples are tested with an acoustic method where the velocity of a wave is determined at a frequency of 37 kHz. The stiffness modulus is determined from the wave velocity (Ruygrok, 1987).

At different temperatures and frequencies, results are available for the complex modulus. In Chapter 6 a method will be described with which the test results for the various temperatures can be compared. The essence of this method is that a change in temperature is comparable to a change in frequency. This method requires the determination of a parameter, the *B*-value, following which a certain frequency and temperature, an equivalent, or a reduced, frequency can be determined at a reference temperature. The results of the tests at different temperatures can be scaled to a reference temperature. From the scaled results for various temperatures, we can then, and in this case only partially, determine an S-curve.

To be able to do this, a suitable *B*-value must be sought in order to arrive at reduced frequencies. The complex moduli for the reduced frequency are plotted in Fig. 5.7. A *B*-value of 22000 K has been used for the reduced frequency. The reference temperature for the figure is 10 °C.

As can be seen in Fig. 5.7, on the basis of the available cyclical tests, only a partial S-curve is to be found. Below, we shall attempt to complete this curve. The supplementary results come from repeated-loading tests (see Fig. 5.8) as carried out within the scope of this research. These are tests which resemble the multiple-step creep tests (see Fig. 3.3). Contrary to the

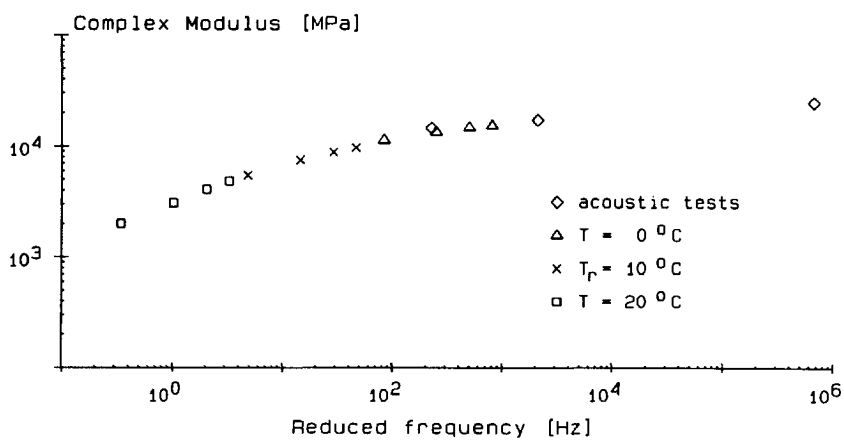

Fig. 5.7. Complex moduli for different reduced frequencies. Reference temperature of 10 °C, B-value of 22000 K.

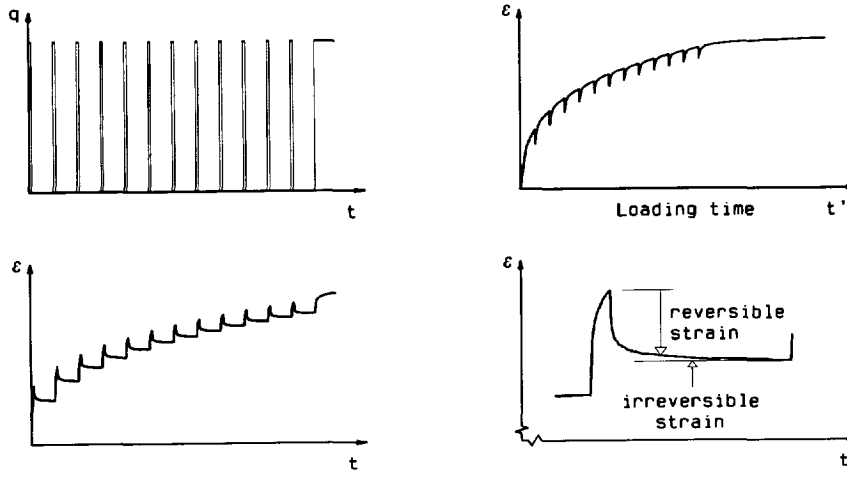

Fig. 5.8. Schematic representation of repeated-loading test.

multiple-step creep tests, the stress is now not placed continuously on the sample, but the load is removed after some time. The time that the sample is loaded amounts in every case to 100 seconds. When the load has been removed, the sample gradually recovers and we find a reversible strain. Following a rest period, a load is again applied. The rest period amounts to 900 seconds. This process of loading and unloading is repeated a number of times. During testing, we not only find (reversible) visco-elastic strain; (irreversible) visco-plastic strain is also found. This permanent strain will only be built up when the sample is loaded. During unloading it is only reversible strains that take place. It is assumed that all reversible strain is activated during the loading phase; in other words, the creep function (see Section 5.1) has reached its maximum value. That this assumption is reasonable appears from Fig. 5.8 where, at the top right, the strain is plotted against the loading time t', this is the total time that load has been applied to the sample. As can be seen in this figure, a smooth line can be taken through the maxima of the curve. The strain that takes place during loading of the sample, touches this line and it can be taken that at the end of the load phase only irreversible strain occurs. The rest phase is significantly longer than the load phase, so that the reversible strains that developed during the load phase, can be completely encountered again at the end of the rest period.

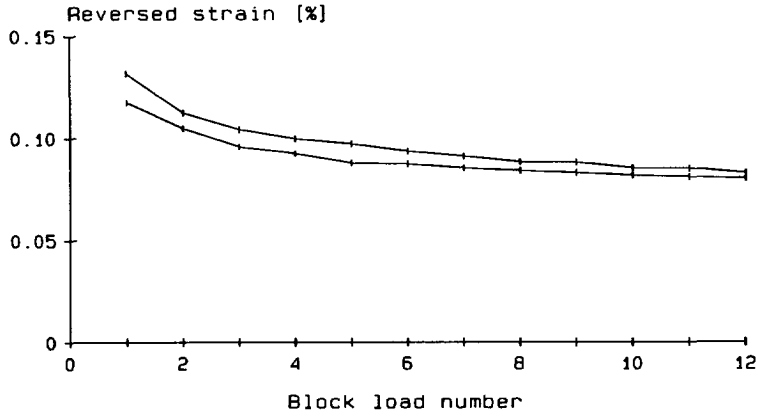

Fig. 5.9. Resulting reversible strains from repeated-loading test. Deviatoric stress 100 kPa, Confining pressure 200 kPa, Temperature 20 °C.

The reversible strains will be used to complete Fig. 5.7. The repeated-loading tests are carried out with various loads at a number of different temperatures. Within the scope of the model to be developed for bituminous concrete, reversible strain is synonymous with visco-elastic strain and irreversible strain is synonymous with visco-plastic strain.

First of all, the reversible strain such as occurs after various block loads will be examined. It appears that after a number of block loads, the reversible strain following each block is approximately equal. Following the first block loads slightly higher reversible strains occur, as can be seen in Fig. 5.9. This is probably a settling in phenomenon. After a number of block loads a more or less steady state arises.

On the basis of these stationary reversible strains, the total reversible strain is studied, i.e. the maximum residual reversible strain. This strain is, of course, dependent on the load applied. In Fig. 5.10 the reversible strain is set out for a number of confining pressures (0, 100, 200 and 300 kPa) and several deviatoric stresses (50, 100, 200 and 400 kPa). A number of matters can be seen in the figure. Firstly, what can be seen is that these strains for the tests with confining pressure are practically independent of the confining pressure, but are about 40 % below those from the tests without

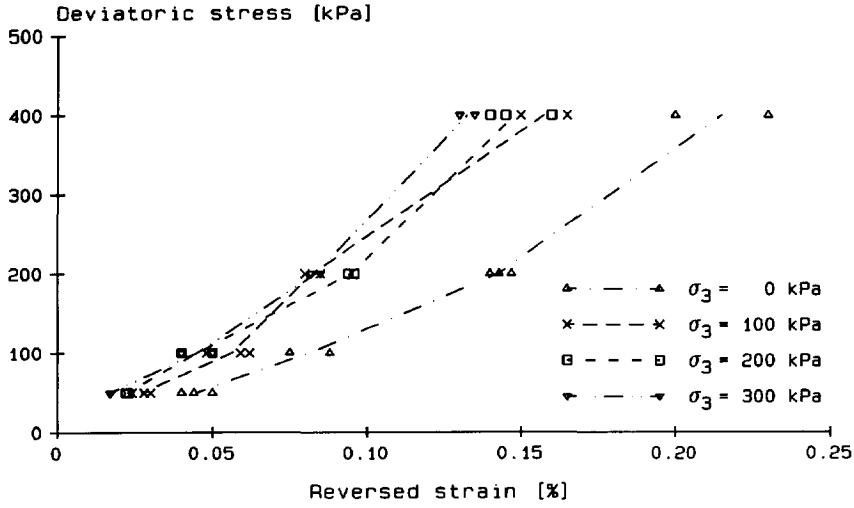

Fig. 5.10. Total reversible strain versus deviatoric stress.

confining pressure. This means that the stiffness i.e. the ratio between the deviatoric stress and the reversible strain, is smaller for the tests without confining pressure. This same effect occurred with the description of the hardening function in Section 4.7. A second noticeable phenomenon in Fig. 5.10 is that the stiffness increases with increasing deviatoric stress. This increase in the stiffness is not dramatic and the results can be described well by a linear relationship between the deviatoric stress and the reversible strain. In Fig. 5.10 such a stiffness modulus of approximately 200 to 300 MPa can be found for the tests with confining pressure. For tests without confining pressure, a modulus of approximately 180 MPa can be found. The modulus which is found in this way for the total reversible strain gives the left asymptote of the S-curve as a supplement to the data in Fig. 5.7. By also considering the time dependent strain after unloading, a time dependent modulus is to be found. This time dependent modulus is defined as

$$E(t) = \frac{\Delta\sigma}{\Delta\varepsilon(t)} \tag{5.17}$$

where t is the time from unloading. In order to be able to compare the results from the repeated-loading tests with the results from the cyclical tests, a load time must be converted into an equivalent frequency. To do this we use the following relationship

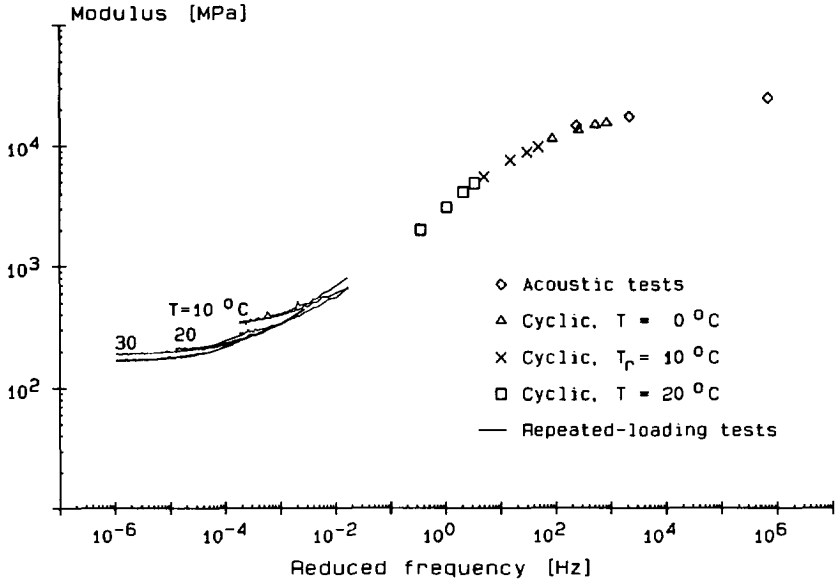

Fig. 5.11. Modulus vs. frequency curve. Same as Fig. 5.7 but augmented with data from repeated-loading test.

$$f_{eq} = \frac{1}{2\pi t} \tag{5.18}$$

This relationship is not exact, but it appears that if the complex modulus according to equation (5.12) is compared with the modulus according to equation (5.17) that there is good agreement. The modulus according to equation (5.17) is equal to $1/c(t)$, with $c(t)$ the creep function according to equation (5.3). By using the relationship (5.18), we can plot the time dependent stiffness modulus against the equivalent frequency. This has been done in Fig. 5.11, where the stiffness modulus so found is plotted against the reduced equivalent frequency. The reduced frequency is calculated by using the same B-value that was used earlier to plot the cyclical tests. The data presented earlier from the cyclical tests are also set out in the figure. From the figure, it appears that with the data a complete S-curve is obtained. The data from the repeated-loading tests at a temperature of 10 °C are higher than the tests at higher temperatures. This is possibly caused by the fact that at this lower temperature, a longer time is required for the reversible strain to develop during the load phase. This can be explained by

the increasing relaxation time; this is the time in which a large part of the strain in a Kelvin-Voigt element occurs. If the load time is small with respect to the relaxation time of a Kelvin-Voigt element, only a part of the strain will occur in this element and as a result a smaller total strain will result. This again means that the modulus obtained is too high.

Now that a complete S-curve has been determined, we can determine material parameters for this bituminous concrete. As commented earlier, we can fit a model on a part of the S-curve for a limited frequency area. Here, however, we shall attempt to describe the whole S-curve well. In order to do this, a series of 10 Kelvin-Voigt elements are used, one element of which with η =0. Table 5.3 gives the fitted values of the parameters. As can be seen from the table, a ratio of 2 has been found for the E-moduli taken between successive moduli, at least for the greater part of the elements. For a good description of the right hand part of the S-curve it was necessary to deviate from this. The ratio between successive viscosities amounts to approximately 2 to 3, except for the first and last viscosities where a higher ratio is obtained.

The complex modulus is plotted in Fig. 5.12 together with the test results. As can be seen, the parameters in Table 5.3 give a good fit for the test results. For the left asymptote, for very low frequencies, a value is found of approximately 180 MPa. The right asymptote for very rapid load cycles gives $E \approx 24$ GPa. If we compare these values with the data from Terrel (see

Table 5.3. Resulting material parameters for Kelvin-Voigt series model, reference temperature of 10 °C.

i	E_i [MPa]	η_i [MPa.s]
0	23800	0
1	23800	10
2	23800	150
3	22400	400
4	11200	750
5	5600	1500
6	2800	3500
7	1400	10000
8	700	50000
9	350	600000

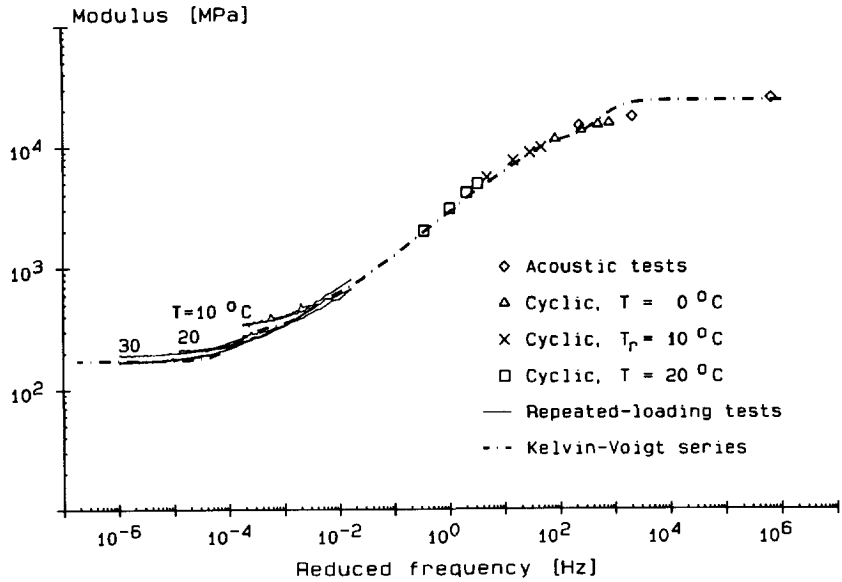

Fig. 5.12. Fit of Kelvin-Voigt series model to test data for Delft bituminous concrete.

Section 5.4), it appears that the right asymptotes agree well. For the lower frequencies the data from Terrel are, however, higher than for Delft bituminous concrete. This means that the viscosities, at the same reference temperature, are higher for Terrel's mixture.

5.6 Concluding remarks on visco-elasticity

It has been argued that the use of a creep function (Eq. 5.1) or a relaxation function (Eq. 5.2) leads to a computationally unattractive model. From a computational point of view it is much more attractive to use a series of Kelvin-Voigt elements. We prefer a series of Kelvin-Voigt elements to a chain of parallel Maxwell elements. This is neither because one of them performs better than the other nor for computational reasons, but due to the fact that it is a generalization of existing bituminous concrete models. Indeed, both the Zener model and the well-known Burgers model, being frequently used for bituminous concrete, can be seen as special cases of a series of Kelvin-Voigt elements.

In order to obtain a complete picture of the behaviour of a bituminous concrete mixture, one or more test samples must be cyclically loaded at a number of frequencies. In order to obtain a complete S-curve, results for at least 8 different frequencies are required. These need to be selected carefully in order to determine all characteristics of the curve. The spring stiffnesses and the viscosities of a series of Kelvin-Voigt elements can then be determined.

If the S-curve is only partly known, the parameters of a series of Kelvin-Voigt elements cannot usefully be determined. In such a case a simpler model can just as well be used; fewer Kelvin-Voigt elements the less data is available.

In the literature on bituminous concrete we often come across the Burgers model as given in Fig. 5.3. This model was applied, among others, by Nunn (1985), Gerritsen (1987), Bednar (1990) and Schmalz et al. (1990). With this relatively simple model we can of course fit the behaviour of bituminous concrete for a very limited frequency interval. Outside the fit interval the model would give very poor results. As a result of the separate dashpot there is, according to the Burgers model, also irreversible strain; it is in fact a visco-elastic visco-plastic model.

With 2 Kelvin-Voigt elements we obtain the Zener model (Fig. 5.3). This is, as it were, a minimum model in which frequency dependence is still included. In this case, judging from the test results, the accuracy can only be guaranteed for a limited frequency interval.

Finally, it must be noted that is was tacitly assumed in this chapter that the visco-elastic behaviour of bituminous concrete is linear. In all publications known to us relating to the visco-elastic behaviour of bituminous concrete this is assumed, but an experimental substantiation could not be found. One could expect that the complex modulus is also determined by various load amplitudes at a given temperature and frequency, but such data could not be found.

6. THE INFLUENCE OF TEMPERATURE ON MATERIAL BEHAVIOUR

In the previous chapters possible formulations are given for the description of the behaviour of bituminous concrete. Material parameters belong together with these formulations. These parameters are dependent on a number of conditions. Temperature is one important influencing factor for a number of parameters. Not all parameters are dependent on temperature. As shown in Section 2.2 the angle of friction and the creep exponent for the description of visco-plastic behaviour are not dependent on temperature. The time factor, τ, which partly determines the rate of visco-plastic strain does depend, just as cohesion, on the temperature. Also for the description of visco-elastic behaviour the temperature is a very important influencing factor. Viscosities in particular will change significantly with a change in temperature.

An attempt will be made in this chapter to determine the influence of temperature on the material parameters. That is, the viscosities for a visco-elastic model and the cohesion and the time parameter τ for the visco-plastic model. Prior to determining the influence of temperature on the individual parameters a general discussion will be given on the temperature dependence of a viscous material.

6.1 The influence of temperature on viscosity η

At first sight the practical application of a visco-elastic model appears to be very awkward because of the large number of parameters. A model that gives a good response for all frequencies of cyclical load and different temperatures requires, after all, a Kelvin-Voigt series with at least 4 elements. That is, four E-moduli and three η-values. These η-values are dependent on temperature. Fortunately, there is a regular pattern with respect to the influence of temperature. Starting from η-values for two different temperatures the viscosity for other temperatures can be calculated with this regular pattern. The basis of this temperature rule can be found in the Rate Process Theory as described by Glasstone et al. (1941) and Mitchell (1964).

The background to the theory is that by applying a stress the distances

between atoms change. By the inherent vibration of the particles, there is a chance that certain atoms take on different positions in relation to each other. The formula for the strain rate that emerges from this can be given as

$$\dot{\varepsilon} = AT\, e^{-B/T} \sinh\,(C\sigma/T) \tag{6.1}$$

with the absolute temperature T in degrees Kelvin. The constants A, B and C depend on the material under consideration. If the formula is applied for relatively low stresses, for example for $C\sigma/T<0.5$ and thus $sinh(C\sigma/T) < 0.52$, we find $sinh(C\sigma/T) \approx C\sigma/T$ and equation (6.1) transforms to

$$\dot{\varepsilon} = D\,\sigma\, e^{-B/T} \quad ; \quad D = AC \tag{6.2}$$

or written in another way

$$\dot{\varepsilon} = \frac{\sigma}{\eta} \quad ; \quad \eta = D\, e^{B/T} \tag{6.3}$$

This equation indicates that the viscosity varies exponentially with $1/T$. If the viscosity at two temperatures is known, the constants B and D can be determined. Starting from a viscosity η_1 at temperature T_1 and a viscosity η_2 at temperature T_2 we find

$$B = \frac{\ln(\eta_1/\eta_2)}{1/T_1 - 1/T_2} \quad ; \quad D = \eta_1 / e^{B/T_1} \tag{6.4}$$

Equation (6.3) denotes an ideal viscous material, a Newton liquid. This law of viscosity would seem to apply reasonably well to bitumen, but equation (6.3) does not, however, suffice for low stresses. A better law of viscosity can be found by replacing σ in the Rate Process Theory by $\sigma-\sigma_0$. This gives after linearization $\dot{\varepsilon} = (\sigma-\sigma_0)/\eta$, where σ_0 is a threshold value of response, as is q_{sct} in equation (2.3) in Chapter 2.

The applicability of the Rate Process Theory for bitumen appears among other things from Fig. 6.1, in which test results from Apicella et al. (1990) and Yan (1988) are represented. Apicella et al. (1990) determined the viscosity of bitumen at different temperatures in the interval from 60 °C to 160 °C. The viscosity was determined by using a coaxial cylinders rotational

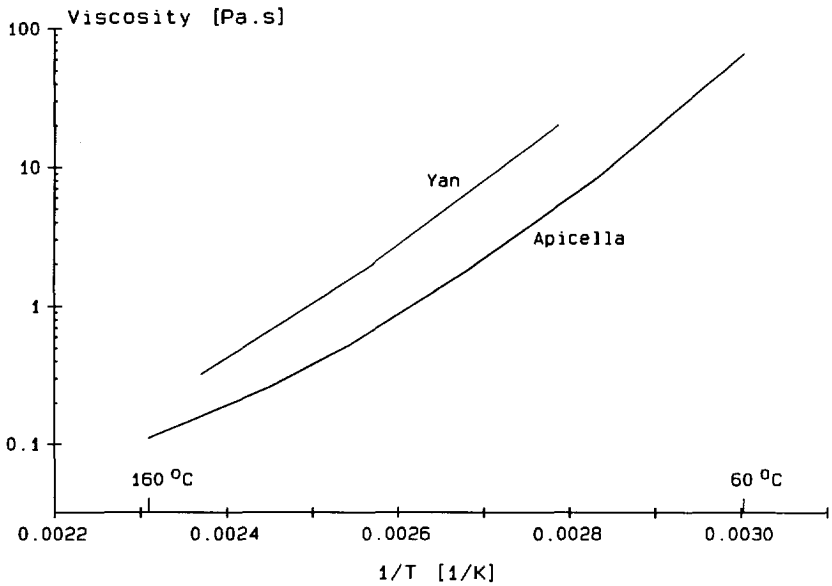

Fig. 6.1. Temperature dependent viscosity of bitumen (after Apicella et al. and Yan).

rheometer. In this way the material is put under shear load with a constant shear speed.

Because the lines in Fig. 6.1 are not completely straight the Rate Process Theory would appear not to be entirely applicable to bitumen, but the discrepancies are relatively small. These discrepancies can be explained by returning to formula (6.1). The constant B in the formula is related to the activation energy of an elementary flow process. This activation energy depends on temperature (Ferry, 1980). This is why no unique *B*-values can be found. However, for a limited temperature interval a constant *B*-value can often suffice. In Fig. 6.1 we can find *B*-values for approximately 6000 to 12000 degrees Kelvin.

6.2 Shift function S(T) for cyclic loading

In order to show that the Rate Process Theory also applies to bituminous concrete we consider cyclic loading and complex *E*-moduli as covered in

Sections 5.3 and 5.4. In the first instance we will restrict ourselves to an S-curve (Fig. 5.5) for test results at a constant temperature. As shown in Section 5.2 the Kelvin-Voigt series applies here:

$$\dot{\varepsilon}^{ve}(t) = \frac{\dot{\sigma}(t)}{E_0} + \sum_{i=1}^{n} \dot{\varepsilon}_i^{ve}(t) \tag{6.5a}$$

where $$\dot{\varepsilon}_i^{ve}(t) = \frac{1}{\eta_i}\left(\sigma(t) - E_i \varepsilon_i^{ve}(t) \right) \tag{6.5b}$$

As yet it has not been shown that

$$\eta_i = D_i \, e^{B/T} \tag{6.6}$$

also applies to bituminous concrete, but we will argue that all dashpots can be described with the same coefficient B. To this end equation (6.6) will first be set out in a different way. The viscosity can be expressed in relation to a viscosity at a different temperature: a reference temperature. Instead of equation (6.6) there follows

$$\eta_i = S(T)\, \eta_i^r \quad ; \quad S(T) = \eta_i/\eta_i^r = e^{B(1/T - 1/T_r)} \tag{6.7}$$

where η_i^r is the viscosity at the reference temperature T_r. The ratio between the viscosities is expressed here by a function $S(T)$. This function gives, therefore, the ratio between the viscosity at a temperature T and the viscosity at the reference temperature T_r. For $T = T_r$ a value $S(T_r) = 1$ follows, for $T>T_r$ $S(T) < 1$ follows and for $T<T_r$ $S(T) > 1$ follows.

Starting from equation (6.7), for equation (6.5b) it follows that

$$\dot{\varepsilon}_i^{ve}(t) = \frac{1}{S(T)\eta_i^r}\left(\sigma(t) - E_i \varepsilon_i^{ve}(t) \right) \tag{6.8}$$

From equation (6.8) it appears that for a creep test at constant stress time is, as it were, scaled. If the temperature is increased, the deformation process for ε_i^{ve}, and therefore for ε^{ve}, takes place more rapidly and by the factor $1/S(T)$.

The above theory can now be applied to cyclic loading as described in Section 5.3. For the Kelvin-Voigt series model, the following equation (5.12) has been derived for the frequency dependent modulus

$$E_c^2 = \left(\frac{\hat{\sigma}}{\hat{\varepsilon}}\right)^2 = \frac{1}{\left(\sum_{i=0}^{n} \frac{x_i}{E_i^2 + x_i^2}\right)^2 + \left(\sum_{i=0}^{n} \frac{E_i}{E_i^2 + x_i^2}\right)^2} \tag{6.9}$$

in which

$$x_i = 2\pi\ \eta_i f = 2\pi\ S(T)\ \eta_i^r\ f \tag{6.10}$$

or written in another way

$$x_i = 2\pi\ \eta_i^r\ f_r \quad , \quad f_r = f\ S(T) \tag{6.11}$$

In the literature f_r is usually referred to as the reduced frequency and $S(T)$ as the shift function. With this formula and equation (6.7) for $S(T)$, it is a simple matter to observe that a change in temperature can be compared with a change in frequency.
Equation (6.7) shows that if there is a change of temperature, the values for the viscosities change, but that the relationships between the viscosities remain the same. Equation (6.10) shows that the change in viscosity corresponds to a change in frequency. A change in temperature is therefore equivalent to a change of frequency.

The above is theoretical and it remains to be seen whether bituminous concrete complies with this. In other words, the theory needs to be verified from test results. One of the most extensive experimental investigations into complex moduli was carried out by Terrel et al. (1973). He reported on complex moduli for 9 different mixtures of bituminous concrete. The results for a mixture with 3.5 % bitumen and a medium aggregate are given in Fig. 6.2. The tests were carried out at a frequency interval of 0.01 to 20 Hz. Each curve in Fig. 6.2 gives the measurement results for a certain temperature. By making use of the shifting function $S(T)$ everything can be reduced to one reference temperature. For every pair of two curves a shifting factor can be measured and by using equation (6.7) a B-factor can then be

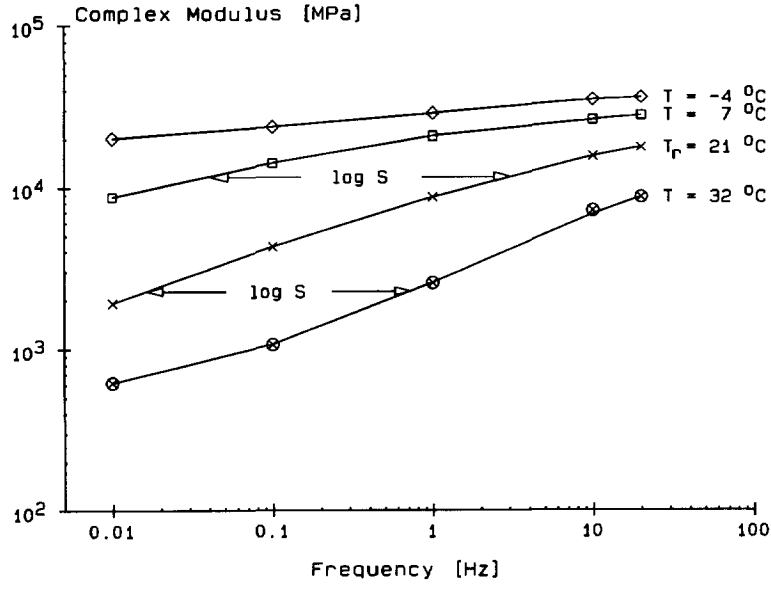

Fig. 6.2 Complex modulus at different temperatures and different frequencies for a bituminous concrete with 3.5 per cent bitumen and medium aggregate after Terrel et al..

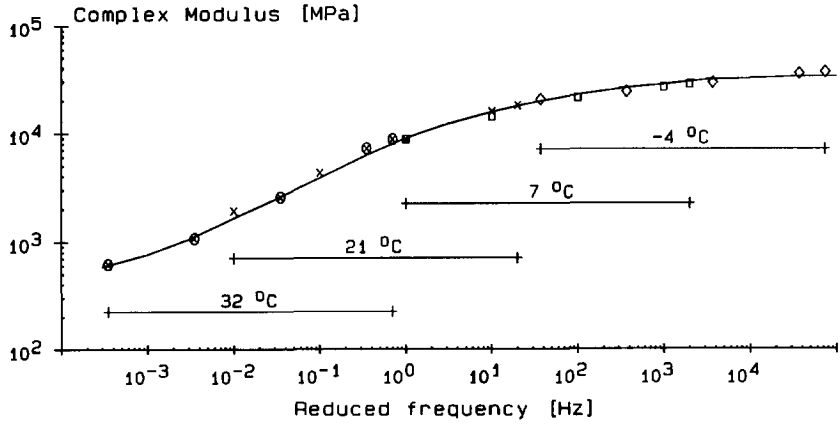

Fig. 6.3 Complex modulus for reduced frequencies, derived from Fig. 6.2. Reference temperature 21 °C.

calculated. All shifting factors then appear to give practically the same B-factor i.e. $B \approx 25000$ K. This proves the effectiveness of the theoretical model. If the shifting factors are applied Fig. 6.2 transforms into Fig. 6.3. This figure has already been used as Fig. 5.5 in Section 5.4. The figure shows a practically complete S-curve for the complex moduli at a reference temperature of $T_r = 21$ °C.

The shift function $S(T)$ for the data presented by Terrel would appear to satisfy the formulation in (6.7). A unique B-factor is not to be found for all mixtures tested by terrel. A unique B-factor implies straight lines in Fig. 6.4. The upper line in Fig. 6.4 corresponds with Terrel's data for a mixture with 2.5 % bitumen and a fine aggregate. The next but one upper curve corresponds with the data in Fig. 6.1. A reference temperature of 21 °C was used for both curves.

In order to further verify the theory for bituminous concrete, the shift functions are set out in Fig. 6.4 on the basis of test data from Chauvin (1990) and Dumont (1992). A complete S-curve did not follow from these last two investigations; the response for the very low reduced frequencies is

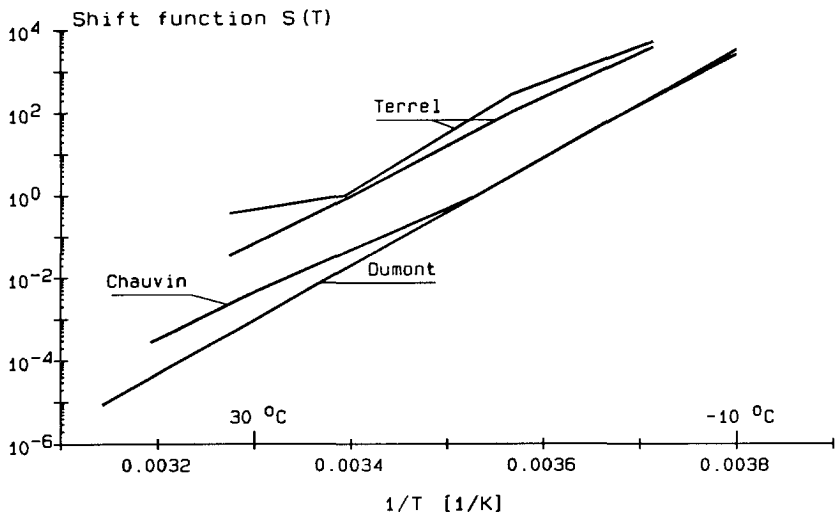

Fig. 6.4 Experimental shift functions for different mixtures of bituminous concrete.

missing. However, a large temperature interval of 50 °C was applied, so that the shift function is known for a greater temperature interval than in Terrel's investigation. Both Chauvin and Dumont used a reference temperature of 10 °C. For this reason these curves are lower than the Terrel's curves to which a reference temperature of 21 °C applies. It would appear from Fig. 6.4 that for the different lines approximately the same slope can be found. This means that for all mixtures approximately the same *B*-values are to be found. The values vary from approximately 25000 K to 30000 K.

6.3 The influence of temperature on the hardening function for visco-plasticity

In Chapter 4, the stress-relaxation tests to determine the hardening curve are described. The results used in Chapter 4 came from tests on Delft bituminous concrete at a relatively high temperature of 28 °C. This was done to keep the times required for the stress-relaxation as short as possible. At lower temperatures the relaxation times would increase rapidly. The results of two tests are set out in Fig. 6.5. These are two tests at a confining pressure of 100 kPa and a deformation rate of $4.2 \cdot 10^{-5}$ s^{-1}. The difference between the two tests lies in the temperature; one test was carried out

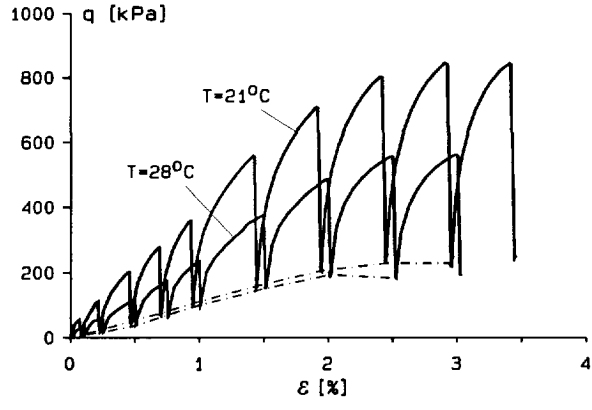

Fig. 6.5. Deviatoric stresses from stress-relaxation tests at different temperatures of 21 and 28 °C. Confining pressure of 100 kPa, deformation rate $4.2 \cdot 10^{-5}$ s^{-1}.

at a temperature of 28 °C, the other test at a temperature of 21 °C. It can be seen from the figure that the stress during the application of the deformation differs significantly.

The difference in peak stress for relaxation at the different temperatures has two causes. This will be explained by using a simplified stress-strain relation. For the simplified stress-strain relation we use $\Delta\sigma = \Delta\varepsilon/(1/E+t/\eta)$, in which E is an elasticity modulus and η a viscosity. As the temperature increases E and η decrease, so that for a given $\Delta\varepsilon$ a smaller $\Delta\sigma$ can be found. The low peak stresses in Fig. 6.5 for T = 28 °C have as cause, therefore, the relatively low elasticity modulus as well as the relatively low viscosity. The low elasticity modulus follows because the deformation is applied over a relatively longer time, and we can in fact not talk of an elasticity modulus but of a rate (and therefore temperature) dependent elasticity modulus.

What is also noticeable in Fig. 6.5 is that the relaxation curves differ little at first glance. In order to demonstrate this further the relaxation curves are set out in Fig. 6.6 for different tests at two temperatures. What is noticeable is that the slope of the relaxation curves is virtually identical. The maximum relaxation stresses from the tests at a temperature of 21 °C are, however, a little higher. If the combinations of maximum stresses

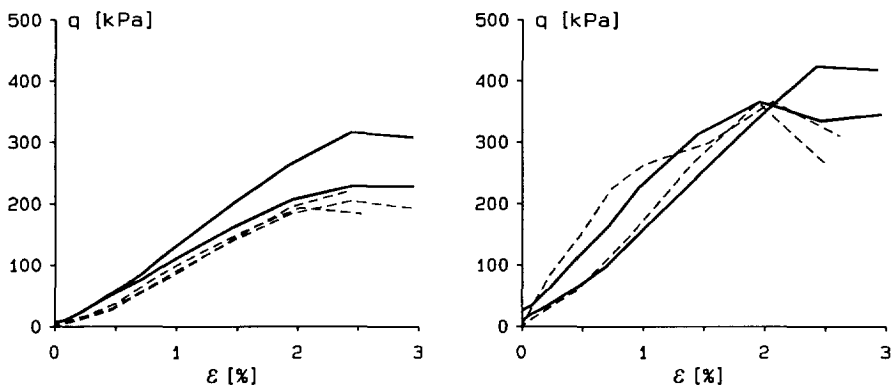

Fig. 6.6. Relaxation curves from stress-relaxation tests at different temperatures of 21 and 28 °C (dashed lines), deformation rate $4.2 \cdot 10^{-5}$ s^{-1}. (a) Confining pressure 100 kPa, (b) confining pressure of 300 kPa.

are set out in the p-q-plane (Fig. 6.7) it would seem as if the slope of M-line is the same. This corresponds with a constant ϕ-value and has been seen earlier in Section 2.2 for data from Di Benedetto. The value of a_{sct} does, however, increase. This means that the cohesion c_{sct} increases. From Fig. 6.7 follows an increase of approximately 30 to 35 per cent for a_{sct} with a temperature decrease from 28 °C to 21 °C. From equation (2.5) it appeared that the cohesion c_{sct} is proportional with a_{sct}, at least for the same angle of friction.

It is possible to deduce the influence of temperature on the cohesion from the above results. The data from Di Benedetto (see Section 2.2) is more suited to describing the temperature influence. It appears that the shifting rule (6.7) gives a reasonable approximation of the influence of temperature. We find

$$c_{sct}(T) = c_{sct}(T_r)\, e^{A(1/T - 1/T_r)}$$
$$a_{sct}(T) = a_{sct}(T_r)\, e^{A(1/T - 1/T_r)} \qquad (6.12)$$

Here a constant A has been included instead of the constant B in (6.7), in order to avoid confusion. The value for A that is found for the data from Di Benedetto is 3200 K. The original data are set out in Table 6.1 together with the values according to (6.12).

This value of A gives a difference of almost 30 per cent for the value of c_{sct} and a_{sct} at a temperature change from 28 °C to 21 °C. It would appear as if for both bitumen mixtures the same A can be used, but there is not a great deal of data for Delft bituminous concrete.

Table 6.1. Comparison values of c_{sct} from testing data by Di Benedetto and values according to equation (6.12) using A = 3200 K.

T [°C]	c_{sct} [kPa]	c_{sct} (6.12)
5	320	322
23	150	160
41	90	86

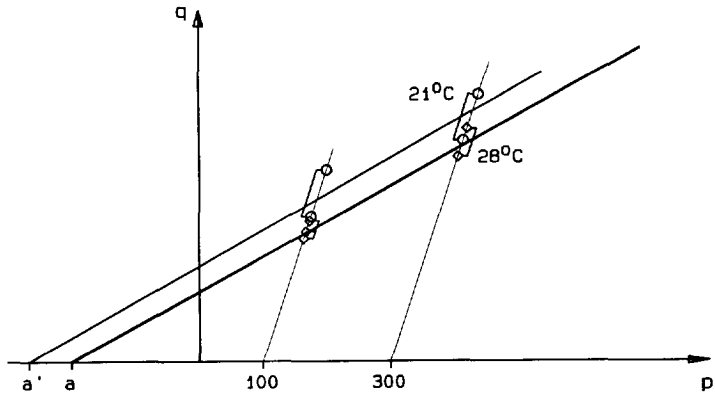

Fig. 6.7. Maxima of relaxation stresses for different confining pressures of 100, 300 kPa and two temperatures of 21 °C and 28 °C.

6.4 The influence of temperature on time parameter τ

In Section 2.2 τ-values are given for results of constant strain rate tests for 3 different temperatures. These τ-values appear to differ a great deal. As commented on earlier, these τ-values cannot simply be compared. In order to do this, first of all the τ-values must be determined for the same β-value (creep exponent in eq. 2.3). In Fig. 6.8 the values are set out for q-q_{sct} for various imposed deformation rates and three different temperatures. The original approximation with the constants from Table 2.1 is indicated by the dashed lines. The continuous lines give an approximation with the same value for β for the three temperatures. For this β-value 4 has been selected.

These new values for τ also appear able to be well described by the shifting formula as (6.7).

$$\tau(T) = \tau_r \, e^{B(1/T - 1/T_r)} \qquad (6.13)$$

A B is used here as earlier in eq. (6.7). It appears that a B-value of 16500 K can describe the τ-values well. Unfortunately a comparison with a B-value

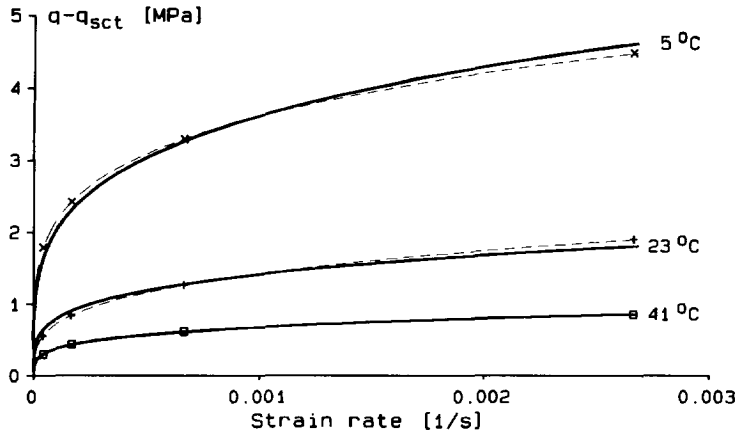

Fig. 6.8. Results and approximations for constant strain rate tests by Di Benedetto. Approximations using values from Table 2.1 (dashed lines) and using a value of 4 for the exponent β.

Table 6.2. Creep time parameter τ for equation (2.3) from constant strain rate triaxial tests performed by Di Benedetto. Values from fit with one value of the creep exponent β and fit using equation (6.13) with B = 16500 K.

T [°C]	β	τ [s]	τ (6.13)
5	4	170000	163000
23	4	4000	4400
41	4	210	180

for viscosity as referred to in Section (6.1) is not possible because no cyclic tests have been carried out on this bituminous concrete.

6.5 Concluding remarks on temperature dependency

In the literature shifting functions are usually used for the description of cyclic test results that are obtained at different temperatures. This procedure has been substantiated by us theoretically and experimentally in this chapter. We are not aware of other such theoretical justifications of

the shift function. The analysis of Section 6.2 shows that the shift function implies the existence of a unique *B*-factor (eq. 6.6) for all viscous elements of the Kelvin-Voigt series. For numerical analysis this *B*-factor is of great importance as it enables the evaluation of viscosities at any temperature.

The influence of the temperature on the visco-plastic behaviour can be found mainly in the rate of creep and to a lesser extent there is an influence on the cohesion. The angle of friction is only determined by the granular structure of the aggregate materials. This is apparently independent of the temperature. The viscous bitumen takes in the first instance a large part of the stress for its own account, but the bitumen creeps in such a way that after a period of time the granular structure takes over a great deal of the stress.

To summarize, the following temperature influences on material parameters have been found. For the viscosities for a visco-elastic Kelvin-Voigt series model:

$$\eta_i = \eta_i^r \, e^{B(1/T - 1/T_r)} \quad , \qquad B \approx 25000 \text{ à } 30000 \text{ K}$$

For the cohesion in the visco-plastic model

$$c_{sct}(T) = c_{sct}(T_r) \, e^{A(1/T - 1/T_r)} \quad , \qquad A \approx 3200 \text{ K}$$

and for the creep time constant τ

$$\tau(T) = \tau_r \, e^{B(1/T - 1/T_r)} \quad , \qquad B \approx 16500 \text{ K}$$

7. GENERAL 3-D CONSTITUTIVE MODEL

In the previous chapters a material model has been determined through triaxial tests. The constitutive equations were formulated in terms of axial strain, axial stress and radial stress. In this chapter, the relationships that have been found so far are generalized for three dimensional states of stress and strain.

7.1 General framework of the model

In the most general case we are dealing with 6 strain components and 6 stress components. For calculating constructions, a plane strain or an axial symmetric schematization is often sufficient. In that case we can do with only 4 components of strain and 4 stress components. We can organize these components in vector form as follows:

$$\underline{\varepsilon} = \{ \varepsilon_{xx}, \varepsilon_{yy}, \varepsilon_{zz}, \gamma_{xy} \}^T$$
$$\underline{\sigma} = \{ \sigma_{xx}, \sigma_{yy}, \sigma_{zz}, \sigma_{xy} \}^T \qquad (7.1)$$

Where the x coordinate and the y coordinate occur in the plane under consideration for the calculation. For the most general three dimensional case where the schematization to a plane strain or axial symmetric construction is not possible or is not desirable, these vectors can be augmented by two terms, γ_{yz} and γ_{zx} for the strain vector and σ_{yz} and σ_{zx} for the stress vector. For plane strain and axial symmetry, these extra terms equal zero.

In Chapters 2 to 4, relationships were given for the visco-plastic strain rate. In Chapter 5 relationships are given for the visco-elastic strains. If we combine both situations of visco-elastic behaviour and visco-plastic behaviour, we are able to resolve the strain and the strain rate into a visco-elastic and a visco-plastic component:

$$\underline{\varepsilon} = \underline{\varepsilon}^{ve} + \underline{\varepsilon}^{vp} \quad ; \quad \dot{\underline{\varepsilon}} = \dot{\underline{\varepsilon}}^{ve} + \dot{\underline{\varepsilon}}^{vp} \qquad (7.2)$$

In this model, the different strain elements will be more or less important depending on the load situation. The visco-plastic strain will be negligibly small with respect to the visco-elastic strain, for example, under low stresses and short load times. This has already been used in Chapter 5, where for cyclic tests it was assumed that the cyclic strain is equal to the visco-elastic strain. On the other hand, for creep tests, the visco-elastic strain is small in relation to the visco-plastic strain. This has already been used in Chapters 3 and 4. The combination of visco-elastic and visco-plastic strains can be seen clearly from the stress development during the application of a deformation. If the deformation is applied more rapidly or at a lower temperature, higher stress peaks occur as shown in Fig. 6.5 for stress-relaxation tests at different temperatures.

7.2 Generalization of Kelvin-Voigt series model

In Chapter 5 a series of Kelvin-Voigt elements was used for the description of the visco-elastic behaviour. With a Kelvin-Voigt element we are dealing with a parallel configuration of spring and dashpot. The same strain is present in the spring and the dashpot, but not the same stress. For such a Kelvin-Voigt element it applies that the stresses in the spring and the dashpot must be added:

$$\underline{\sigma} = \underline{\sigma}_i^{spring} + \underline{\sigma}_i^{dashpot} \quad \text{or} \quad \underline{\sigma}_i^{dashpot} = \underline{\sigma} - \underline{\sigma}_i^{spring} \tag{7.3}$$

We shall use a linear relationship for both the spring and the dashpot. For the spring a linear relationship between the stress and the strain and for the dashpot a linear relationship between the stress and the strain rate. These relationships are:

$$\begin{aligned} \underline{\sigma}_i^{spring} &= \underline{\underline{D}}_i \cdot \underline{\varepsilon}_i^{ve} \\ \underline{\sigma}_i^{dashpot} &= \underline{\underline{M}}_i \cdot \dot{\underline{\varepsilon}}_i^{ve} \end{aligned} \tag{7.4}$$

Including here an elasticity matrix $\underline{\underline{D}}_i$ and a viscosity matrix $\underline{\underline{M}}_i$, which are generally described as:

$$\underline{\underline{D}}_i = \frac{E_i}{(1+\nu_i)(1-2\nu_i)} \begin{bmatrix} 1-\nu_i & \nu_i & \nu_i & 0 \\ \nu_i & 1-\nu_i & \nu_i & 0 \\ \nu_i & \nu_i & 1-\nu_i & 0 \\ 0 & 0 & 0 & \frac{1}{2}-\nu_i \end{bmatrix}$$

$$\underline{\underline{M}}_i = \frac{\eta_i}{(1+\nu_i)(1-2\nu_i)} \begin{bmatrix} 1-\nu_i & \nu_i & \nu_i & 0 \\ \nu_i & 1-\nu_i & \nu_i & 0 \\ \nu_i & \nu_i & 1-\nu_i & 0 \\ 0 & 0 & 0 & \frac{1}{2}-\nu_i \end{bmatrix} \tag{7.5}$$

For each element of the Kelvin-Voigt series, a different Young's modulus E_i can be given, a different Poisson's ratio ν_i and a different viscosity η_i. For a Kelvin-Voigt element it is assumed that in the matrices $\underline{\underline{D}}_i$ and $\underline{\underline{M}}_i$ the same value for the Poisson's ratio can be taken. By a combination of equations (7.3) and (7.4) we find for the strain rate $\dot{\underline{\varepsilon}}_i^{ve}$ for element i in the Kelvin-Voigt series:

$$\dot{\underline{\varepsilon}}_i^{ve} = \underline{\underline{M}}_i^{-1} \left(\underline{\sigma} - \underline{\sigma}_i^{spring} \right) = \underline{\underline{M}}_i^{-1} \underline{\sigma} - \frac{E_i}{\eta_i} \underline{\varepsilon}_i^{ve} \tag{7.6}$$

The term E_i/η_i follows from evaluation of $\underline{\underline{M}}_i^{-1}\underline{\underline{D}}_i$. This results in a diagonal matrix with terms E_i/η_i on the diagonal. This applies, incidentally, only when Poisson's ratio ν_i for the spring and the dashpot are taken as equal, as assumed in this study.

For the total series of Kelvin-Voigt elements we can set out

$$\dot{\underline{\varepsilon}}^{ve} = \dot{\underline{\varepsilon}}_0^{ve} + \sum_{i=1}^{n} \dot{\underline{\varepsilon}}_i^{ve} = \underline{\underline{D}}_0^{-1} \cdot \dot{\underline{\sigma}} + \sum_{i=1}^{n} \left(\underline{\underline{M}}_i^{-1} \underline{\sigma} - \frac{E_i}{\eta_i} \underline{\varepsilon}_i^{ve} \right) \tag{7.7}$$

Here, the subscript 0 is used for the Kelvin-Voigt element degenerated to a pure elastic element.

In Chapter 5 parameters were determined for the separate Kelvin-Voigt elements for two bituminous concrete mixtures. These parameters are based on uniaxial situations, where only the vertical stress and strain are included. This gave the values for E_i and η_i. For a general three dimensional situation, a third parameter should be determined in addition to these

values. This is, for example, the Poisson's ratio ν_1. This ν-value should be determined again per element of the Kelvin-Voigt series. The ν-values can be determined if, in addition to the vertical strain, the horizontal strain is also measured. After all, for a uniaxial test on a linear elastic isotropic material, the horizontal strain is equal to $-\nu$ times the vertical strain. The precise determination of the ν-values for each element in the Kelvin-Voigt series is only possible if the complex Poisson's ratio is also given through cyclic testing.

Terrel (1973) states that for high frequencies and low temperatures, this is for the right hand asymptote in the S-curve in Fig. 5.5, the complex Poisson's ratio assumes low values, but provides no quantitative information. For low frequencies and high temperatures Terrel states, on the other hand, a Poisson's ratio of approximately 0.5. The same effects are found for Delft bituminous concrete. Starting with the data in Section 5.5, Montauban (1988) finds for high frequencies (acoustic tests) a Poisson's ratio of 0.2 to 0.35. He finds low values between 0.2 and 0.25 at a low temperature of 0 °C and higher values of 0.3 to 0.35 at a temperature of 30 °C. This seems to be in accordance with the investigation by Terrel, because we are still dealing with high frequencies. N.B., Montauban gives no Poisson's ratio for slow changes of load. The latter is possible using repeated-loading tests as performed in the context of this present investigation. For the relatively slow repeated-loading tests, as stated in Section 5.5, the horizontal strains have also been measured. The Poisson's ratio could, therefore, be determined for all instants. It appeared that shortly after the release of load (± 3 seconds) a Poisson's ratio can be found which already had a value greater than 0.4. The Poisson's ratio then increases to values of approximately 0.5. This is also in accordance with Terrel's findings.

It would appear then that for the Kelvin-Voigt elements with a low E-modulus that a high Poisson's ratio must be taken, for example of 0.49. A value of 0.5 for Poisson's ratio results in numerical problems because the viscosity matrix $\underline{\underline{M}}$ cannot then be inverted. For the Kelvin-Voigt elements with a high E-modulus lower values for the Poisson's ratio of approximately 0.2 to 0.3 should be taken. The intermediate elements can, for example, be taken in ascending order. For making calculations in practical situations, the choice of a Poisson's ratio of approximately 0.2 to 0.3 for the separate spring,

rising to a Poisson's ratio of approximately 0.45 to 0.49 for the weakest element would appear to be sufficient. Table 7.1 presents again a summary of the parameters which can be used for Delft bituminous concrete.

As indicated in Table 7.1, the values apply for a temperature of 20 °C. Earlier, in Section 5.5, viscosities were determined for a temperature of 10 °C. In Chapter 6 it is shown how to calculate the values of the viscosities for a different temperature. For a shift in the temperature of 10 °C to 20 °C it follows, with a *B*-value of 22000 K as found in section 5.5 for Delft bituminous concrete, that all viscosities should be multiplied by a factor 0.07. The values of the viscosities in Table 7.1 have been determined thus from the values in Table 5.3.

It would seem that a large number of parameters need to be determined before a calculation can finally be done with a Kelvin-Voigt series model, but this is only partially true. As indicated earlier, Section 5.5, it is possible to approximate the S-curve in Fig. 5.12 well by including 10 Kelvin-Voigt elements in the modelling. For an arbitrary bituminous concrete mixture it is possible to determine the parameters by assuming, for example, the greatest and smallest value of the complex modulus. The greatest *E*-modulus, belonging to element 0, is then known. In Table 7.1 a ratio of 2 is assumed between the successive moduli, at least for the moduli of the elements 3 to 9. For example, by assuming this ratio of 2 between the successive *E*-moduli, or by

Table 7.1. Parameters for the Kelvin-Voigt elements for Delft bituminous concrete, reference temperature of 20 °C.

i	E_i [MPa]	η_i [MPa.s]	ν_i [-]
0	23800	0	0.25
1	23800	0.7	0.30
2	23800	10	0.30
3	22400	30	0.35
4	11200	50	0.35
5	5600	100	0.40
6	2800	250	0.40
7	1400	700	0.45
8	700	3500	0.45
9	350	40000	0.49

adjusting this ratio a little. The other E-moduli can be determined fairly rapidly such that with the help of equation (5.14) the minimum complex modulus has been found. By maintaining the ratios of the viscosities in Table 7.1, the viscosities for the new mixture can be found if the complex modulus is known for an intermediate frequency. The values of the Poisson's ratio in Table 7.1 can be maintained.

7.3 Generalization of visco-plastic creep model

For the value of the visco-plastic creep rate a number of formulas have been derived in the previous chapters. A general formulation for the visco-plastic creep rate is the following

$$\dot{\underline{\varepsilon}}^{vp} = \frac{1}{\tau} f^{\beta} \frac{\partial g}{\partial \underline{\sigma}} \qquad \text{for } f > 0 \tag{7.8}$$

in which f is a so-called yield function. For values of f greater than 0 we find a visco-plastic creep rate. For values of f smaller than or equal to 0 the visco-plastic creep rate is equal to 0. The plastic-potential function g determines the direction of the creep rate vector. The time-parameter τ and the exponent β determine the size of the creep rate.

For the yield function f we made in Section 4.6 a distinction between two situations, triaxial compression and triaxial extension. By inputting an alternative deviatoric stress, $\tilde{q}$, we can consider these two situations simultaneously as well as all other possible stress situations. To this end we define the yield function f as

$$f = \frac{\tilde{q}}{p^*} - h(\kappa, p) \tag{7.9}$$

in which

$$h(\kappa, p) = M^*_{sct} \frac{\kappa}{\kappa_{sct}} e^{1-\kappa/\kappa_{sct}} \tag{7.9b}$$

$$M^*_{sct} = M_{sct} \left(1 - e^{-(p+p_1)/p_2} \right) \tag{7.9c}$$

The hardening function is now calculated by means of the variable κ. This variable κ is a more general strain variable than the vertical strain used in equation (4.2). The calculation of κ from the strains will be covered later. By inputting $\tilde{q}$ we can suffice with one formulation. This $\tilde{q}$ is expressed in principal stresses

$$\tilde{q} = \sigma_1 + \sigma_2 - 2\sigma_3 \tag{7.10}$$

where the principal stresses are ordered in such a way that $\sigma_1 \geq \sigma_2 \geq \sigma_3$, where pressure is assumed positive. For triaxial compression situations with $\sigma_1 \geq \sigma_2 = \sigma_3$ $\tilde{q}$ reduces to $\sigma_1 - \sigma_3$ and for triaxial extension situations with $\sigma_1 = \sigma_2 \geq \sigma_3$ $\tilde{q}$ reduces to $2(\sigma_1 - \sigma_3)$. Thus are the formulas (4.5) derived. In the three dimensional principal stress space f=0 gives a pyramid like shape as shown in Fig. 7.1. In the deviatoric plane f=0 gives a triangle as shown in Fig. 7.2.

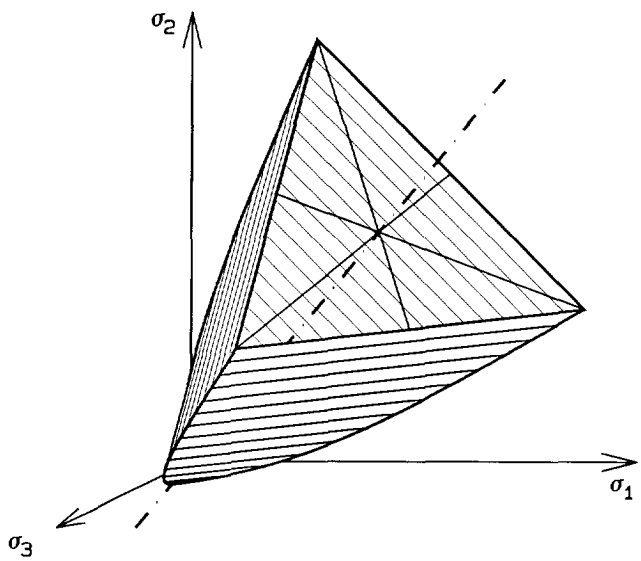

Fig. 7.1. Three-dimensional yield surface in principal stress space.

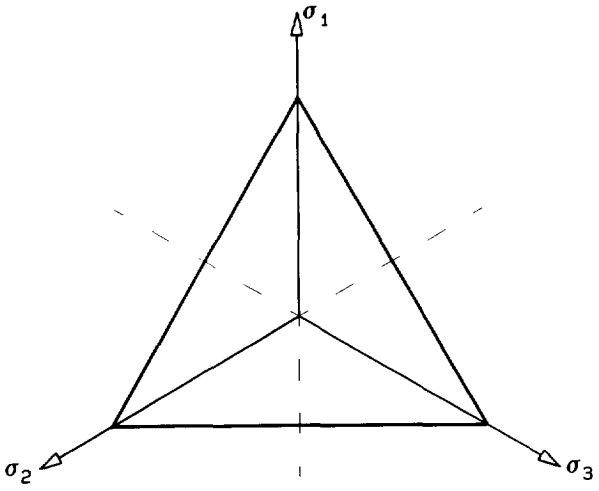

Fig. 7.2. Yield surface in deviatoric plane.

Vertex plasticity

With an angular yield surface as shown in Fig. 7.2, the corners need to be treated specially. Above the top of the triangle in Fig. 7.2 we have two yield functions with a positive value. These yield functions are

$$f_1 = \frac{\sigma_1 + \sigma_2 - 2\sigma_3}{p^*} - h(\kappa, p)$$
$$f_2 = \frac{\sigma_1 - 2\sigma_2 + \sigma_3}{p^*} - h(\kappa, p) \qquad (7.11)$$

For the visco-plastic strain rate we can now write (Koiter, 1960)

$$\dot{\underline{\varepsilon}}^{vp} = \Phi_1 \frac{\partial g_1}{\partial \underline{\sigma}} + \Phi_2 \frac{\partial g_2}{\partial \underline{\sigma}} \qquad (7.12)$$

in which $\Phi_1 = f_1^{\beta}/\tau$, $\Phi_2 = f_2^{\beta}/\tau$ (7.12b)

The plastic potential functions g_1 and g_2 belong to the yield functions f_1 and f_2 respectively. For these plastic potential functions we take the following functions

$$g_1 = \sigma_1 + \sigma_2 - 2\sigma_3 - h'(\kappa,p)\ p$$

$$g_2 = \sigma_1 - 2\sigma_2 + \sigma_3 - h'(\kappa,p)\ p \tag{7.13}$$

Where the function $h'(\kappa,p)$ is equal to the hardening function in equation (7.9b) for the yield function, except that a different parameter M'_{sct} is used in place of the parameter M_{sct} which was used for the yield function. By taking these functions, the derivative of the functions is perpendicular to the associated yield surfaces in the deviatoric plane in Fig. 7.2. Instead of a parameter M_{sct} in the yield function we now use a different constant M'_{sct}. This parameter can be expressed in the dilation angle ψ_{sct}. If the parameter M'_{sct} is taken to be equal to M_{sct}, then the vector $\partial g/\partial \underline{\sigma}$ is perpendicular to the yield surface. It appears from the tests not to be the case and we must take a lower value for M'_{sct}.

In the case of triaxial compression states of stress with $\sigma_2=\sigma_3$ it follows from equation (7.12b) that Φ_1 and Φ_2 are equal. We then find that

$$\dot{\underline{\varepsilon}}^{vp} = \Phi \left(\frac{\partial g_1}{\partial \underline{\sigma}} + \frac{\partial g_2}{\partial \underline{\sigma}} \right) \quad , \quad \Phi = f_1^{\beta}/\tau = f_2^{\beta}/\tau \tag{7.14}$$

if we plot $\dot{\underline{\varepsilon}}^{vp}$ as a vector in the principal stress space, and project it onto the deviatoric surface, this points in the direction of the principal stress σ_1.

The strain invariants which are associated with the stress invariants p and q, are the volume strain ε_{vol}, and the deviatoric strain κ. These invariants are calculated as follows

$$\dot{\varepsilon}^{vp}_{vol} = \dot{\varepsilon}^{vp}_1 + \dot{\varepsilon}^{vp}_2 + \dot{\varepsilon}^{vp}_3$$

$$\dot{\kappa} = \sqrt{\frac{2}{3}\left(\dot{e}^{vp2}_1 + \dot{e}^{vp2}_2 + \dot{e}^{vp2}_3 \right)} \tag{7.15}$$

with the deviatoric strain rates that are calculated as

$$\dot{e}^{vp}_1 = \dot{\varepsilon}^{vp}_1 - \frac{1}{3}\dot{\varepsilon}^{vp}_{vol} \ , \ \dot{e}^{vp}_2 = \dot{\varepsilon}^{vp}_2 - \frac{1}{3}\dot{\varepsilon}^{vp}_{vol} \ , \ \dot{e}^{vp}_3 = \dot{\varepsilon}^{vp}_3 - \frac{1}{3}\dot{\varepsilon}^{vp}_{vol} \tag{7.16}$$

In the case of triaxial stress situations $\dot{\kappa}$ reduces to

$$\dot{\kappa} = \frac{2}{3}(\dot{\varepsilon}_1^{vp} - \dot{\varepsilon}_3^{vp}) \tag{7.17}$$

at least if the strain rates are sorted as $\dot{\varepsilon}_1^{vp} \geq \dot{\varepsilon}_2^{vp} \geq \dot{\varepsilon}_3^{vp}$. For material where no plastic volume strains occur, we find for triaxial compression stress states that $\dot{\varepsilon}_2^{vp} = \dot{\varepsilon}_3^{vp} = -\frac{1}{2}\dot{\varepsilon}_1^{vp}$ and $\dot{\kappa}$ reduces to the axial component $\dot{\varepsilon}_1^{vp}$.

With the help of equations (7.11) to (7.16) incl., it can be shown that for triaxial compression situations

$$\dot{\varepsilon}_{vol}^{vp} = -2\Phi M' \quad ; \quad \dot{\kappa} = 2\Phi \tag{7.18}$$

In the same way, it can be shown that for triaxial extension situations (Φ_2=0)

$$\dot{\varepsilon}_{vol}^{vp} = -\Phi M' \quad ; \quad \dot{\kappa} = 2\Phi \tag{7.19}$$

In Fig. 7.3 the visco-plastic volume strain rates and the visco-plastic deviatoric strain rate $\dot{\kappa}$ is set out. These data are derived from compression stress-relaxation tests.

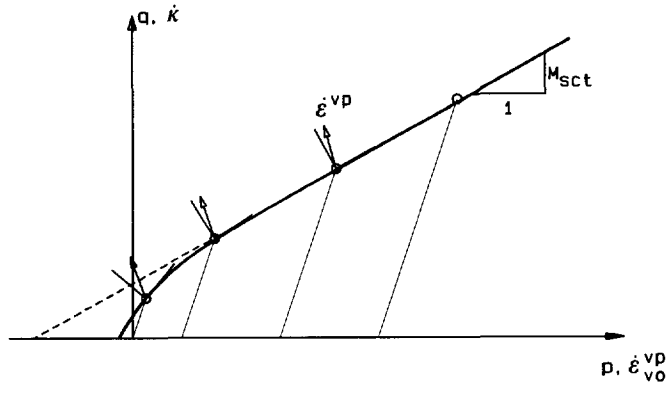

Fig. 7.3. Visco-plastic strain rate vector from stress-relaxation tests.

As can be seen in the figure, the incremental strain vector is not perpendicular to the yield surface. This means that we are not dealing here with associated behaviour. It can also be seen that the incremental strain vector is not vertical. In a pure vertical direction no visco-plastic volume changes occur. If no visco-plastic volume changes occur, this implies that the strain variable κ is in agreement with the vertical strain; if no visco-plastic volume changes occur, the horizontal strain ε_3^{vp} is equal to minus half the vertical strain ε_1^{vp} and with equation (7.17) it follows therefore that $\dot{\kappa} = \dot{\varepsilon}_1^{vp}$. Because some volume increase does take place, κ is greater than the vertical strain ε_1^{vp}, because of this we must take for κ_{sct} (equation 7.11) a slightly higher value than for ε_{sct} in equation (4.2). It appears from the direction of the incremental strain vector that for M'_{sct} we can take about half of M_{sct}.

Fig. 7.3 is drawn for the maximum relaxation stresses. Before these maximum relaxation stresses have been reached, we can also determine the incremental strain vector. It can be seen from this that the choice of the same hardening function with a different parameter M'_{sct} is a reasonable choice.

For completeness, an overview is given in Table 7.2 of the parameters to be used for the visco-plastic part of the model, applied to Delft bituminous concrete.

Table. 7.2. Material parameters for the visco-plastic part of the model. Parameters for Delft bituminous concrete.

Characteristic time	τ	5400	s	T = 20 °C
Creep exponent	β	2.5		
Mean stress additive	a_{sct}	270	kPa	T = 20 °C
Friction coefficient	M_{sct}	0.55		
Pre-peak strain	κ_{sct}	0.03		
Isotropic tensile stress	p_1	28	kPa	
Yield-surface convexity	p_2	53	kPa	
Dilation coefficient	M'_{sct}	0.30		

The parameters where a temperature is given depend, to a greater or lesser extent, on the temperature. In Chapter 6 the influence of temperature on these parameters was determined. Making use of the temperature shift rules found in Chapter 6, the values found earlier for a temperature of 28 °C are calculated for a temperature of 20 °C, in order to obtain one set of parameters, both the parameters that describe the visco-elastic part of the model and the parameters that describe the visco-plastic part of the model, at one temperature.

The parameters used can also be converted into other parameters. In Section 2.2 a conversion is given from the parameters M_{sct} and a_{sct} to a cohesion c_{sct} and an angle of friction ϕ_{sct}.

7.4 Some comments on the shape of the yield function

By choosing the formulation of $\tilde{q}$ in equation (7.10), the triangular form of the yield surface in the deviatoric plane follows. Equation (7.10) is a special case of the following formulation

$$\tilde{q} = \sigma_1 + (\alpha-1)\sigma_2 - \alpha\sigma_3 \tag{7.20}$$

where α is the ratio between the M-value in compression and the M-value in extension situations. For a value of 2 for α the equation (7.10) again follows. By varying α (between 1 and 2), the shape of the yield surface in the deviatoric surface changes from an equilateral Tresca hexagon to the equilateral triangle in Fig. 7.2. The well known shape of Mohr-Coulomb criterion is found for $\alpha = (3+\sin\phi)/(3-\sin\phi)$.
For an α-value greater than 2 a concave yield surface follows. Here it is possible that a combination of two stress situations where elastic behaviour occur, leads to a situation where plastic strains occur. This is shown in Fig. 7.4a, where a combination, σ_C, of two stress situations, σ_A and σ_B, which only cause reversible strains, gives rise to the occurrence of irreversible strains.
A situation where the ratio between the M-values in compression and extension is greater than 2, without loss of convexity of the yield surface, is possible by including anisotropy. Here the strength in the various directions

is different. This can be caused by the rolling process, for example. The stresses σ_1, σ_2 and σ_3 are then linked to these physical directions. In various directions, or in one direction, a higher strength is found than in the other directions. This is shown in Fig. 7.4b, where it is assumed that the 2 direction is a weaker direction.

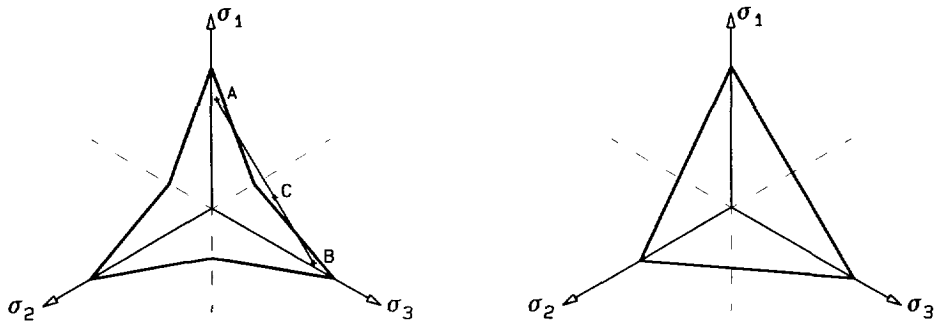

Fig. 7.4. (a) Non-convex yield surface for $\alpha>2$. (b) Non-isotropic yield surface with $\alpha>2$.

8. TIME INTEGRATION OF DIFFERENTIAL STRESS-STRAIN MODEL

In the previous chapters a model was derived for bituminous concrete. The model equations are given in strain rates. In order to calculate practical problems, these equations have to be solved in time. To this end, the practical problem is divided into a number of time steps. For this reason it is necessary to establish equations for finite time steps. There are incremental equations, i.e. equations that include finite increments of stress and strain. When establishing these equations for finite increments, such items as convergence, accuracy and acceptable time step size should be taken into account. These three considerations are interrelated; if convergence does not occur, the chosen time step will be too long and the accuracy will increase if smaller time steps are taken. On the other hand, the calculation time will increase if excessively small time steps are taken.

8.1 Basic time-integration

In order to calculate a finite time step, the model equations derived earlier should be integrated over the time step. The following time integration is used as the basis for the time integration for the model equations:

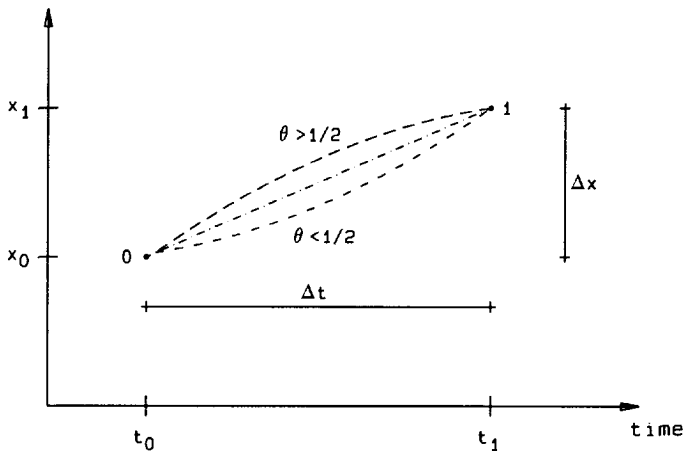

Fig. 8.1. Time integration.

$$\int_{t_0}^{t_0+\Delta t} x\,dt = x(t_0)\Delta t + \theta\Delta x\Delta t \quad ; \quad \Delta x = x(t_0+\Delta t) - x(t_0) \tag{8.1}$$

In the following, the value for a variable at the start of a time step will be given a subscript 0: i.e. $x_0 = x(t_0)$. The value at the end of a time step is indicated by a subscript 1: i.e. $x_1 = x(t_0+\Delta t)$. In equation (8.1) an integration constant θ is used. For explicit integration, a value of 0 for θ follows. For a value of $\frac{1}{2}$ we are dealing with trapezoidal integration and with a value of 1 for θ implicit integration follows. A value of $\frac{1}{2}$ often gives a good approximation to the integration, particularly if relatively small time steps are taken. The error in the integration is, after all, determined by the step size and the second derivative of the function x(t). For $\theta=\frac{1}{2}$:

$$\int_{t_0}^{t_1} x\,dt = \tfrac{1}{2}(x_0+x_1)\Delta t + O(\Delta t^3 x^{(2)}) \tag{8.2}$$

where O() is the error term in which $x^{(2)}$ is the second derivative of the function x at a point $t=\xi$ for which $t_0 \le t=\xi \le t_1$ applies. For small values of Δt the error in the integration is small. For large values of Δt the error can be large.

In the equations for bituminous concrete, the following solution plays a major role

$$x(t) = a + bt + ce^{-dt} \tag{8.3}$$

A similar function is, for example, found for the creep function in equation (5.3). The value of θ does not make any difference for the first two terms in equation (8.3); these terms do not give an error in the integration. However, the last term can, for larger time steps, result in a large error in the integration. By taking a larger value for θ, the integral is approximated better, as is shown in Tables 8.1 and 8.2. In Table 8.1 the integral of $x(t) = e^{-t}$ is determined for the interval of $t=t_0=0$ to $t=t_1=\Delta t$ and for different values of θ. In Table 8.2 the relative error that occurs in numerical integration is shown.

Table 8.1. Comparison of the integration, exact and numerical, of the function $x(t)=e^{-t}$ from $t=0$ to $t=\Delta t$ for different values of the integration parameter θ.

Δt	exact	$\theta=\frac{1}{2}$	0.6	0.7	0.8	0.9	1.0
0.01	0.00995	0.010	0.010	0.010	0.010	0.010	0.010
0.1	0.09516	0.095	0.094	0.093	0.092	0.091	0.090
0.5	0.39347	0.402	0.382	0.362	0.343	0.323	0.303
1	0.63212	0.684	0.621	0.558	0.494	0.431	0.368
2	0.86466	1.135	0.962	0.789	0.617	0.444	0.271
5	0.99326	2.517	2.020	1.524	1.027	0.530	0.034
10	0.99995	5.000	4.000	3.000	2.000	1.000	0.000

Table 8.2. Relative error, (Numerical-Exact)/Exact, in numerical integration [%].

Δt	$\theta=\frac{1}{2}$	0.6	0.7	0.8	0.9	1.0
0.01	0.00	-0.10	-0.20	-0.30	-0.40	-0.50
0.1	0.08	-0.92	-1.92	-2.92	-3.92	-4.92
0.5	2.07	-2.93	-7.93	-12.93	-17.93	-22.93
1	8.20	-1.80	-11.80	-21.80	-31.80	-41.80
2	31.30	11.30	-8.70	-28.70	-48.70	-68.70
5	153.39	103.39	53.39	3.39	-46.61	-96.61
10	400.05	300.05	200.05	100.05	0.05	-99.95

It can be deduced from Tables 8.1 and 8.2 that for large time steps, a larger value of θ gives better results, though too great a value of θ can also give poor results.

In order to derive the finite incremental relations, a distinction is made between the visco-elastic and the visco-plastic parts of the model. We shall start with the visco-elastic part of the model.

8.2 Integration of visco-elastic strain rates

The visco-elastic part of the model is represented by a series of Kelvin-Voigt elements, see Chapter 5. One of these elements is degenerated to an elastic spring element. The following relation was derived in Section 7.2 for a Kelvin-Voigt element:

$$\dot{\underline{\varepsilon}}_i^{ve} = \underline{\underline{M}}_i^{-1} \left(\underline{\sigma} - \underline{\underline{D}}_i \dot{\underline{\varepsilon}}_i^{ve} \right) = \underline{\underline{M}}_i^{-1} \underline{\sigma} - \frac{E_i}{\eta_i} \underline{\varepsilon}_i^{ve} \tag{8.4}$$

where the subscript i refers to Kelvin-Voigt element i. The spring element is represented by the elastic matrix $\underline{\underline{D}}_i$ and the dashpot element by the viscosity matrix $\underline{\underline{M}}_i$. For convenience a constant λ_i will be introduced for the ratio of Young's modulus E_i and the viscosity η_i: $\lambda_i = E_i/\eta_i$. Time integration of equation (8.4) gives

$$\int \dot{\underline{\varepsilon}}_i^{ve} \, dt = \int \left(\underline{\underline{M}}_i^{-1} \underline{\sigma} - \lambda_i \underline{\varepsilon}_i^{ve} \right) dt \quad , \quad \lambda_i = E_i/\eta_i \tag{8.5}$$

By using equation (8.1) this integration can be worked out and this gives the following relationship

$$\Delta\underline{\varepsilon}_i^{ve} = \underline{\underline{M}}_i^{-1} \left(\underline{\sigma}_0 \Delta t + \theta \Delta\underline{\sigma} \Delta t \right) - \lambda_i \left(\underline{\varepsilon}_{i0}^{ve} + \theta \Delta\underline{\varepsilon}_i^{ve} \Delta t \right) \tag{8.6}$$

Rearranging this equation gives

$$\left(1 + \theta \Delta t \lambda_i \right) \Delta\underline{\varepsilon}_i^{ve} = \theta \Delta t \, \underline{\underline{M}}_i^{-1} \Delta\underline{\sigma} + \Delta t \, \underline{\underline{M}}_i^{-1} \underline{\sigma}_0 - \Delta t \, \lambda_i \underline{\varepsilon}_{i0}^{ve} \tag{8.7}$$

The incremental strain of Kelvin-Voigt element i can now be expressed in the stress increment $\Delta\underline{\sigma}$, the stress at the start of the step $\underline{\sigma}_0$ and the strain in the element at the start of the step $\underline{\varepsilon}_{i0}^{ve}$

$$\Delta\underline{\varepsilon}_i^{ve} = \frac{\Delta t}{1 + \theta \Delta t \lambda_i} \left(\theta \underline{\underline{M}}_i^{-1} \Delta\underline{\sigma} + \underline{\underline{M}}_i^{-1} \underline{\sigma}_0 - \lambda_i \underline{\varepsilon}_{i0}^{ve} \right) \tag{8.8}$$

For element 0 in the Kelvin-Voigt series, the element degenerated to a spring, we can use the following relationships

$$\dot{\underline{\varepsilon}}_0^{ve} = \underline{\underline{D}}_0^{-1} \dot{\underline{\sigma}} \qquad \text{and} \qquad \dot{\underline{\sigma}} = \underline{\underline{D}}_0 \dot{\underline{\varepsilon}}_0^{ve} \tag{8.9}$$

By using this relationship, the stress increment is determined. The strain in this element is equal to the total strain minus the strain in the other Kelvin-Voigt elements and the visco-plastic strain. Moreover, according to equation (7.2) it applies that

$$\dot{\underline{\varepsilon}} = \dot{\underline{\varepsilon}}^{ve} + \dot{\underline{\varepsilon}}^{vp} = \dot{\underline{\varepsilon}}_0^{ve} + \sum_{i=1}^{n} \dot{\underline{\varepsilon}}_i^{ve} + \dot{\underline{\varepsilon}}^{vp} \tag{8.10}$$

and from this we derive that

$$\dot{\underline{\varepsilon}}_0^{ve} = \dot{\underline{\varepsilon}} - \sum_{i=1}^{n} \dot{\underline{\varepsilon}}_i^{ve} - \dot{\underline{\varepsilon}}^{vp} \tag{8.11}$$

The stress rate according to equation (8.9) is therefore equal to

$$\dot{\underline{\sigma}} = \underline{\underline{D}}_0(\dot{\underline{\varepsilon}}-\dot{\underline{\varepsilon}}^{vp}) - \sum_{i=1}^{n} \underline{\underline{D}}_0\dot{\underline{\varepsilon}}_i^{ve} \tag{8.12}$$

Integrated according to equation (8.1) this gives

$$\Delta\underline{\sigma} = \underline{\underline{D}}_0(\Delta\underline{\varepsilon}-\Delta\underline{\varepsilon}^{vp}) - \sum_{i=1}^{n} \underline{\underline{D}}_0\Delta\underline{\varepsilon}_i^{ve} \tag{8.13}$$

and with relationship (8.8) for the incremental strain $\Delta\underline{\varepsilon}_i^{ve}$ for the Kelvin-Voigt element i this gives the following equation

$$\Delta\underline{\sigma} = \underline{\underline{D}}_0(\Delta\underline{\varepsilon}-\Delta\underline{\varepsilon}^{vp}) - \underline{\underline{D}}_0 \sum_{i=1}^{n}\left\{\frac{\Delta t}{1+\theta\Delta t\lambda_i}\left(\theta\underline{\underline{M}}_i^{-1}\Delta\underline{\sigma} + \underline{\underline{M}}_i^{-1}\underline{\sigma}_0 - \lambda_i\underline{\varepsilon}_{i0}^{ve}\right)\right\} \tag{8.14}$$

After rearrangement, this equation becomes

$$\Delta\underline{\sigma} = \underline{\underline{P}}\,(\Delta\underline{\varepsilon}-\Delta\underline{\varepsilon}^{vp}) - \underline{\underline{P}}\left\{\sum_{i=1}^{n}\left(\frac{\Delta t}{1+\theta\Delta t\lambda_i}\underline{\underline{M}}_i^{-1}\right)\right\}\underline{\sigma}_0 + \underline{\underline{P}}\left\{\sum_{i=1}^{n}\left(\frac{\Delta t}{1+\theta\Delta t\lambda_i}\lambda_i\underline{\varepsilon}_{i0}^{ve}\right)\right\} \tag{8.15}$$

where

$$\underline{\underline{P}} = \left[\underline{\underline{I}} + \sum_{i=1}^{n}\left(\frac{\theta\Delta t}{1+\theta\Delta t\lambda_i}\underline{\underline{D}}_0\underline{\underline{M}}_i^{-1}\right)\right]^{-1}\underline{\underline{D}}_0$$

The stress increment $\Delta\underline{\sigma}$ is expressed in the total strain increment $\Delta\underline{\varepsilon}$, the unknown visco-plastic strain increment $\Delta\underline{\varepsilon}^{vp}$, the stress $\underline{\sigma}_0$ at the start of the step and the initial strains in the separate Kelvin-Voigt elements $\underline{\varepsilon}_{i0}^{ve}$.

Equation (8.15) can be written even more simply as

$$\Delta\underline{\sigma} = \underline{\underline{P}}(\Delta\underline{\varepsilon}-\Delta\underline{\varepsilon}^{vp}) + \Delta\underline{\sigma}^{ve} \tag{8.16}$$

in which

$$\Delta\underline{\sigma}^{ve} = -\underline{\underline{P}}\left\{\sum_{i=1}^{n}\left(\frac{\Delta t}{1+\theta\Delta t\lambda_i}\underline{\underline{M}}_i^{-1}\right)\right\}\underline{\sigma}_0 + \underline{\underline{P}}\left\{\sum_{i=1}^{n}\left(\frac{\Delta t}{1+\theta\Delta t\lambda_i}\lambda_i\underline{\varepsilon}_{i0}^{ve}\right)\right\}$$

$$= -\underline{\underline{P}}\sum_{i=1}^{n}\frac{\Delta t}{1+\theta\Delta t\lambda_i}\left(\underline{\underline{M}}_i^{-1}\underline{\sigma}_0 - \lambda_i\underline{\varepsilon}_{i0}^{ve}\right)$$

The significance of $\Delta\underline{\sigma}^{ve}$ in equation (8.16) is the stress change that occurs if pure visco-elastic relaxation takes place, relaxation in the elastic area; because the stress flows out of the dashpots. In the formulation selected, the value of $\Delta\underline{\sigma}^{ve}$ depends only on the state at the start of the step by means of $\underline{\sigma}_0$ and $\underline{\varepsilon}_{i0}^{ve}$, the chosen time step Δt and the integration constant θ. The change in the stresses or the internal strains during the time step Δt have, therefore, no influence on the value of $\Delta\underline{\sigma}^{ve}$.

8.3 Integration of visco-plastic strain rates

Up until now it has only been assumed that during the time step Δt an incremental visco-plastic strain equal to $\Delta\underline{\varepsilon}^{vp}$ occurs. A very simple method for determining this increment is explicit integration of the visco-plastic strain rate, the visco-plastic strain increment depends only on the state at the start of the time step and the size of that time step. The disadvantage of this explicit method is that small time steps are required in order to ensure convergence and accuracy. It is for this reason that, analogous with the integration of the visco-elastic strain rates, a time integration is used in the form

$$\Delta\underline{\varepsilon}^{vp} = \int \dot{\underline{\varepsilon}}^{vp}\,dt = (1-\theta)\Delta t\dot{\underline{\varepsilon}}_0^{vp} + \theta\Delta t\dot{\underline{\varepsilon}}_1^{vp} \tag{8.17}$$

where the subscript 1 is used for the value of a variable at the end of the time step. For a value of 0 for θ explicit integration follows, for a value of 1 for θ, implicit integration follows. The value of the visco-plastic strain rate $\dot{\underline{\varepsilon}}_0^{vp}$ is determined from the state at the start of the time step. The value follows from equation (7.8) or from equation (7.12) in Section 7.3. The value of the visco-plastic strain rate $\dot{\underline{\varepsilon}}_1^{vp}$ is determined for the state at the end of the time step. Unfortunately, the stresses and the value of the hardening variable at the end of the time step are not known a priori and a (sub)iteration scheme is required for determining $\dot{\underline{\varepsilon}}_1^{vp}$. One possible approach for calculating the stress increment is as follows: determine, by estimating $\dot{\underline{\varepsilon}}_1^{vp}$ and the change in the hardening variable $\dot{\kappa}_1$ an estimate for $\Delta\underline{\varepsilon}^{vp}$ and $\Delta\kappa$. Using these values, with equation (8.16) an estimate can then be made of the stress increment $\Delta\underline{\sigma}$. If this increment is known, the values for $\dot{\underline{\varepsilon}}_1^{vp}$ and $\dot{\kappa}_1$ can be calculated and new estimates for $\Delta\underline{\varepsilon}^{vp}$ and $\Delta\kappa$ follow. Generally speaking, these new estimates will not be equal to the old estimate. By using these new estimates, an estimate of the stress increment can be determined. If the difference in stress increment in consecutive iterations is small, then the (sub)iteration process need not be continued. If this is not the case, the process can be repeated with the improved estimates.

This basic iteration scheme can be adapted in a number of ways. The first estimates for $\Delta\underline{\varepsilon}^{vp}$ and $\Delta\kappa$ are made by using the incremental values from the previous step. It is assumed here that the incremental values in consecutive steps differ little and the values from the previous step do give a good estimate of the values in the current step. A different acceleration procedure follows from the value of $\Delta\underline{\sigma}$ in an iteration step being not only determined from the results of the current iteration step, but also from the estimate in the previous iteration step. Otherwise, the final solution would definitely be oscillating. Moreover, if a start is made with a small increment for the visco-plastic strain, a large stress increment $\Delta\underline{\sigma}$ would, in the first instance, be found. A high stress follows from this large stress increment and therefore, a large visco-plastic strain rate. In the second iteration, a large visco-plastic strain increment is used from which a small stress increment follows. In some cases, particularly if excessively large time steps are used, this could lead to divergence.

8.4 Critical time steps for visco-elasticity

There is, for the integration of the visco-elastic strain rate as well as for the visco-plastic strain rate, a limit to the time step. Oscillations may occur if the time steps are too large. In the worst case, a divergence may even occur for which no solution can be found. As has already been stated, oscillations may occur if the time steps are too large. This is shown in Fig. 8.2 for a simple Zener model without visco-plasticity, where at t=0 a uniaxial stress state with a unit vertical stress is applied. For this case the strain in time must give the creep function. In the figure, the solution is given for various time steps. For larger time steps oscillations seem to occur, and divergence does not occur, because an integration constant θ of $\frac{1}{2}$ is used for the calculations. Booker and Small (1977) have derived for visco-elasticity that for $\theta \geq \frac{1}{2}$ the integration process is unconditionally stable, although oscillations can occur. For values $\theta < \frac{1}{2}$ a limit applies for the time step whereby no divergence occurs.

It is still possible for the simple Zener model to give a relationship for the time step Δt where oscillations just do not yet occur. For a more complicated model, with more Kelvin-Voigt elements, it is much more difficult to find a good relationship for a time step for which no oscillations occur. One possibility is to consider the same creep test, and then to require that oscillations do not occur in a single Kelvin-Voigt element. To this end, use is made of equation (8.8). In the case of a creep test, this equation reduces to

$$\Delta \underline{\varepsilon}_i^{ve} = \frac{\Delta t}{1+\theta \Delta t \lambda_i} \left(\underline{\underline{M}}_i^{-1} \underline{\sigma}_0 - \lambda_i \underline{\varepsilon}_{i0}^{ve} \right) \tag{8.18}$$

Because the stress is known and does not change over time, the final strain in the Kelvin-Voigt element can be calculated.

$$\underline{\varepsilon}_{i\infty}^{ve} = \underline{\underline{D}}_i^{-1} \underline{\sigma}_\infty = \underline{\underline{D}}_i^{-1} \underline{\sigma}_0 \tag{8.19}$$

The maximum increment of the strain is equal to

$$\Delta \underline{\varepsilon}_i^{ve} = \frac{\Delta t}{1+\theta \Delta t \lambda_i} \left(\underline{\underline{M}}_i^{-1} \underline{\underline{D}}_i \underline{\varepsilon}_{i\infty}^{ve} - \lambda_i \underline{\varepsilon}_{i0}^{ve} \right) = \frac{\Delta t}{1+\theta \Delta t \lambda_i} \lambda_i \Delta \underline{\varepsilon}_i^{ve} \tag{8.20}$$

This equality applies exactly for

$$\frac{\Delta t\lambda_i}{1+\theta\Delta t\lambda_i} = 1 \qquad \text{or} \qquad \Delta t = \frac{\eta_i}{E_i}\,\frac{1}{1-\theta} \tag{8.21}$$

From further consideration of the critical time step found in this way by using certain material parameters, for example in Table 7.1, it appears that for the stiff spring elements that determine the right hand asymptote of the S-curve for cyclical load, it is necessary to use very small time steps, or an integration constant θ close to 1. The reason behind this is that these Kelvin-Voigt elements react so rapidly, that for the greater part of the time step the final strain state has already been reached, which justifies an integration constant of almost 1. The limit case actually applies to the element 0, which was degenerated to a spring, for which η=0 applies. Here, all stress will flow directly into the spring-element. Any unbalance between the external stress and the stress in the spring is corrected immediately, i.e with infinite strain rate.

Another possibility for allowing time steps larger than indicated in equation (8.21) is considering such a rapidly reacting Kelvin-Voigt element as instantaneous, which means that more Kelvin-Voigt elements degenerate to a single spring-element for large time steps. In practical situations where it is not the very rapid response after having applied a load that is of interest, it is therefore possible to take the Kelvin-Voigt elements that are then important together. If one is interested, however, in the rapid reactions, the possible reason often lies in the fact that rapidly changing loads are being considered. Here, in order to describe the load, small time steps must be taken.

In Fig. 8.2 the influence of varying the time step is shown for an academic problem. In this problem, a test specimen is uniaxially loaded with an instantaneously applied unit stress. For the material behaviour, the Zener model (see Fig. 5.3) is assumed for the description of the visco-elastic behaviour; no visco-plasticity is included. The theoretical solution for the time dependent strain is given by creep function as dealt with in Section 5.2. The material parameters used are

$$E_0 = 2 \;;\; \nu_0 = 0 \;;\; E_1 = 2 \;;\; \nu_1 = 0 \;;\; \eta_1 = 2$$

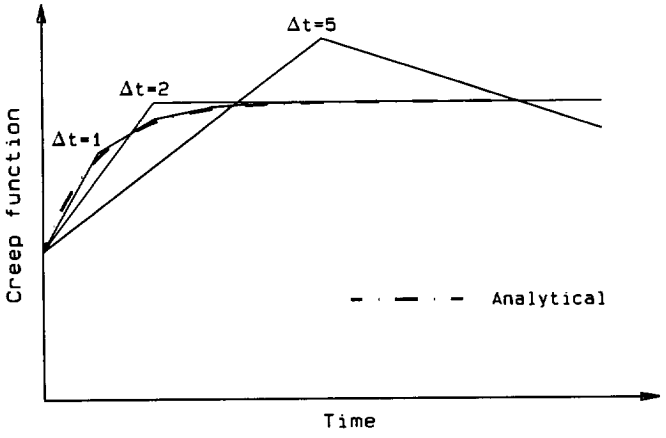

Fig. 8.2. Comparison of results for different time steps for an academic problem involving the Zener model.

The creep function for this case is

$$c(t) = 1 - \frac{1}{2} e^{-t} \tag{8.22}$$

In accordance with equation (8.21) the critical time step for this problem is equal to 2, at least if an integration constant θ of $\frac{1}{2}$ is used. In Fig. 8.2 the solutions found for the various time steps have been plotted. These time steps are 1, 2 and 5. As can be seen in the figure, there is only a small difference, of a few percent, to be seen between the exact solution and the time step of 1. The time step of 2, the time step in accordance with equation (8.21), produces after one step the final value of the creep function, following which the strain does not change further. For the time step of 5 we can see oscillating strains; finally, the value for the strain for this time step converges to the exact solution.

The possibility of varying the integration constant θ is not only a global possibility, i.e. for all Kelvin-Voigt elements at the same time, but it is also possible to input a more or less ideal integration constant θ_i per Kelvin-Voigt element, for example

$$\theta_i = 1 - 0.7 \frac{\eta_i}{E_i \Delta t} \quad ; \quad \theta_i \geq 0.5 \tag{8.23}$$

for $\Delta t E_i/\eta_i > 3$ and a linear interpolation between $\theta_i = \frac{1}{2}$ for $\Delta t=0$ and θ_i according to equation (8.23) for $\Delta t E_i/\eta_i = 3$. By taking a factor 1 instead of 0.7 in equation (8.23) the equality of equation (8.21) follows exactly and, in the case of a creep test, the exact solution for $t=\infty$ would be found. It appears that by taking this relationship for θ_i per Kelvin-Voigt element, the errors are small.

8.5 Theory on time step selection for visco-plasticity

Various methods are given in the literature in order to arrive at stable results by limiting the time step. The permissible time step depends on the material and on the stress state. For example, Cormeau (1975) gives a derivation for the permissible time step in time integration. The disadvantage of the method used is that the method is really only suitable for associated material behaviour.

Another method, see for example Stolle (1989), assumes the visco-plastic strain rate at the end of a time step for elasto-visco-plasticity. If visco-plasticity occurs at the start of the time step, $f_0>0$, the visco-plasticity should still occur at the end of a time step, $f_1>0$. The visco-plastic strain rate is given by

$$\dot{\underline{\varepsilon}}^{vp} = \Phi(f)\,\frac{\partial g}{\partial \underline{\sigma}} \tag{8.24}$$

where, for example, $\Phi(f) = f^{\beta}/\tau$. If at the end of the step visco-plasticity still occurs, $\Phi(f_1)>0$ applies. Φ is approximated by a truncated Taylor series:

$$\Phi_1 \cong \Phi_0 + \frac{\partial \Phi}{\partial \underline{\sigma}}^T \Delta\underline{\sigma} + \frac{\partial \Phi}{\partial \kappa}\Delta\kappa \tag{8.25}$$

For explicit integration we have for an elastic-visco-plastic model

$$\Delta\underline{\sigma} = \underline{\underline{D}}(\Delta\underline{\varepsilon} - \Delta\underline{\varepsilon}^{vp}) \tag{8.26}$$

$$\Phi_1 = \left(1 - \frac{\partial \Phi}{\partial \underline{\sigma}}^T \underline{\underline{D}}\,\frac{\partial g}{\partial \underline{\sigma}}\Delta t\right)\Phi_0 + \frac{\partial \Phi}{\partial \underline{\sigma}}^T \underline{\underline{D}}\Delta\underline{\varepsilon} + \frac{\partial \Phi}{\partial \kappa}\Delta\kappa \tag{8.27}$$

The term $\frac{\partial\Phi}{\partial\kappa}\Delta\kappa$ can be written as $-\frac{\partial\Phi}{\partial f}H_p\Phi_0\Delta t$, where H_p is a visco-plastic hardening parameter. Similarly we can write

$$\frac{\partial\Phi}{\partial\underline{\sigma}}^T \underline{\underline{D}}\frac{\partial g}{\partial\underline{\sigma}} = \frac{\partial\Phi}{\partial f}\frac{\partial f}{\partial\underline{\sigma}}^T \underline{\underline{D}}\frac{\partial g}{\partial\underline{\sigma}} = \frac{\partial\Phi}{\partial f}H_e \tag{8.28}$$

and we have

$$\Phi_1 = \left(1 - \frac{\partial\Phi}{\partial f}(H_e+H_p)\Delta t\right)\Phi_0 + \frac{\partial\Phi}{\partial f}\frac{\partial f}{\partial\underline{\sigma}}^T \underline{\underline{D}}\Delta\underline{\varepsilon} \tag{8.29}$$

For stress relaxation ($\Delta\underline{\varepsilon}=\underline{0}$) we find that

$$\Delta t \le \Delta t_{max} = \frac{1}{\frac{\partial\Phi}{\partial f}(H_e+H_p)} \tag{8.30}$$

where Δt_{max} is the maximum time step for non-oscillating visco-plasticity. This method is suitable for explicit integration and for a linear rate-law ($\partial\Phi/\partial f$=constant). Here, for all stress points a model dependent value can be calculated for the maximum permissible time step. These values will differ little for linear yield functions and if H_p is approximately equal for all stress points or if H_p is small in comparison with H_e.

In order to determine convergence of the sub-iteration process for visco-plasticity, it is not an expression for the critical time step that is sought, but a more general investigation of the progress of the sub-iteration process for determining the visco-plastic strain increment. Considering the non-linear relationship for the visco-plastic strain rate, the derived relationships do not then apply generally, but continually changing values may occur during the sub-iteration process.

The scheme used for the sub-iteration process is as follows:

- Determine $\Delta\underline{\sigma}^*$ by means of $\Delta\underline{\varepsilon}^{vp}_{k-1}$, the visco-plastic strain increment from the previous sub-iteration,

- Determine $\underline{\sigma}^*_1 = \underline{\sigma}_0 + \Delta\underline{\sigma}^*$, a prediction of the stress at the end of the time step,

- Determine the strain rate for this stress $\dot{\underline{\varepsilon}}_1^{vp*} = \Phi(\underline{\sigma}_1^*)\frac{\partial g}{\partial \underline{\sigma}}$, $\Phi = f^{\beta}/\tau$

- $\Delta\underline{\varepsilon}^{vp*} = \left((1-\theta)\dot{\underline{\varepsilon}}_0^{vp} + \theta\, \dot{\underline{\varepsilon}}_1^{vp*} \right) \Delta t$,

- $\Delta\underline{\varepsilon}^{vp}{}_k = \Delta\underline{\varepsilon}^{vp}{}_{k-1} + \omega\left(\Delta\underline{\varepsilon}^{vp*} - \Delta\underline{\varepsilon}^{vp}{}_{k-1}\right)$

In the last step the parameter ω represents an under-relaxation factor, which means that the final visco-plastic strain increment is determined from the information from the predicted stress $\underline{\sigma}_1^*$ during this sub-iteration and from the increment from the previous sub-iteration. If this were not the case then oscillations would occur with a greater chance of divergence.

The approach used for deriving relationships for the time step, the integration constant θ and the under-relaxation factor ω is as follows: Assume an initial small disturbance in the exact solution. Determine the disturbance after a sub-iteration step. The ratio between the disturbances before and after the sub-iteration step, give relationships for the parameters to be used.

We state that the exact solution is given by

$$\Delta\underline{\sigma} = \underline{\underline{P}}(\Delta\underline{\varepsilon}-\Delta\underline{\varepsilon}^{vp}) + \Delta\underline{\sigma}^{ve} \tag{8.31}$$

In sub-iteration k-1 we found that $\Delta\underline{\varepsilon}^{vp}{}_{k-1} = \Delta\underline{\varepsilon}^{vp} + \delta\Delta\underline{\varepsilon}^{vp}{}_{k-1}$, where $\delta\Delta\underline{\varepsilon}^{vp}{}_{k-1}$ is a (small) error in comparison with the exact solution. For predicting the stress $\Delta\underline{\sigma}^*$ it is found that:

$$\Delta\underline{\sigma}^* = \underline{\underline{P}}(\Delta\underline{\varepsilon}-\Delta\underline{\varepsilon}^{vp}{}_{k-1}) + \Delta\underline{\sigma}^{ve} = \Delta\underline{\sigma} - \underline{\underline{P}}\ \delta\Delta\underline{\varepsilon}^{vp}{}_{k-1} \tag{8.32}$$

$$\underline{\sigma}_1^* = \underline{\sigma}_1 - \underline{\underline{P}}\ \delta\Delta\underline{\varepsilon}^{vp}{}_{k-1} \tag{8.33}$$

where $\underline{\sigma}_1$ is the exact solution for the stress at the end of the time step. The value of the visco-plastic strain rate at the end of the time is given by

$$\dot{\underline{\varepsilon}}_1^{vp*} = \Phi(\underline{\sigma}_1^*)\frac{\partial g}{\partial \underline{\sigma}} = \Phi(\underline{\sigma}_1 - \underline{\underline{P}}\delta\Delta\underline{\varepsilon}^{vp}{}_{k-1})\frac{\partial g}{\partial \underline{\sigma}} \tag{8.34}$$

Here, it is assumed that the derivative of the plastic potential function does not change. By linearisation around the exact solution it is found that

$$\dot{\underline{\varepsilon}}_1^{vp*} = \dot{\underline{\varepsilon}}_1^{vp} - \frac{\partial g}{\partial \underline{\sigma}} \frac{\partial \Phi}{\partial \underline{\sigma}}^T \underline{\underline{P}} \delta\Delta\underline{\varepsilon}^{vp}{}_{k-1} \tag{8.35}$$

By using this value it is found for the visco-plastic strain increment that

$$\Delta\underline{\varepsilon}^{vp*} = \left((1-\theta)\dot{\underline{\varepsilon}}_0^{vp} + \theta\, \dot{\underline{\varepsilon}}_1^{vp} - \theta \frac{\partial g}{\partial \underline{\sigma}} \frac{\partial \Phi}{\partial \underline{\sigma}}^T \underline{\underline{P}} \delta\Delta\underline{\varepsilon}^{vp}{}_{k-1} \right) \Delta t$$

$$= \Delta\underline{\varepsilon}^{vp} - \theta\Delta t \frac{\partial g}{\partial \underline{\sigma}} \frac{\partial \Phi}{\partial \underline{\sigma}}^T \underline{\underline{P}} \delta\Delta\underline{\varepsilon}^{vp}{}_{k-1} \tag{8.36}$$

And finally under-relaxation is applied which gives:

$$\Delta\underline{\varepsilon}^{vp}{}_k = (1-\omega)\Delta\underline{\varepsilon}^{vp}{}_{k-1} + \omega\Delta\underline{\varepsilon}^{vp} - \omega\theta\Delta t \frac{\partial g}{\partial \underline{\sigma}} \frac{\partial \Phi}{\partial \underline{\sigma}}^T \underline{\underline{P}} \delta\Delta\underline{\varepsilon}^{vp}{}_{k-1} \tag{8.37}$$

The error can now be looked at after all steps in the sub-iteration process. This error is equal to

$$\delta\Delta\underline{\varepsilon}^{vp}{}_k = \Delta\underline{\varepsilon}^{vp}{}_k - \Delta\underline{\varepsilon}^{vp}$$

$$\delta\Delta\underline{\varepsilon}^{vp}{}_k = \left[(1-\omega)\underline{\underline{I}} - \omega\theta\Delta t \frac{\partial g}{\partial \underline{\sigma}} \frac{\partial \Phi}{\partial \underline{\sigma}}^T \underline{\underline{P}} \right] \delta\Delta\underline{\varepsilon}^{vp}{}_{k-1} = \underline{\underline{A}}\ \delta\Delta\underline{\varepsilon}^{vp}{}_{k-1} \tag{8.38}$$

With $\underline{\underline{A}}$ an amplification matrix. For convergence it is necessary that

$$|\delta\Delta\underline{\varepsilon}^{vp}{}_k| < |\delta\Delta\underline{\varepsilon}^{vp}{}_{k-1}| \tag{8.39}$$

For this the maximum eigenvalue of the amplification matrix $\underline{\underline{A}}$ should apply that

$$\underline{\underline{A}}:\ |\lambda_{max}| < 1 \tag{8.40}$$

It appears simply that $\partial g/\partial \underline{\sigma}$ is always an eigenvector of $\underline{\underline{A}}$. It is assumed that the related eigenvalue is the maximum eigenvalue. This related eigenvalue is equal to

$$\lambda = 1-\omega - \omega\theta\Delta t \frac{\partial\Phi}{\partial\underline{\sigma}}^T \underline{\underline{P}} \frac{\partial g}{\partial\underline{\sigma}} \tag{8.41}$$

From the requirement that the greatest eigenvalue remains limited to 1 arise a number of considerations. We found

$$-1 < 1-\omega - \omega\theta\Delta t \frac{\partial\Phi}{\partial\underline{\sigma}}^T \underline{\underline{P}} \frac{\partial g}{\partial\underline{\sigma}} < 1 \tag{8.42}$$

The equation on the right presents no problems; this is always satisfied. The left hand equation can be interpreted in a number of ways. For example, we can write

$$\Delta t < \frac{2-\omega}{\omega\theta \frac{\partial\Phi}{\partial\underline{\sigma}}^T \underline{\underline{P}} \frac{\partial g}{\partial\underline{\sigma}}} \tag{8.43}$$

This equation appears simple, but there is a difficulty in the fact that the matrix $\underline{\underline{P}}$ also depends on the time step Δt, see equation (8.15). For this reason the critical time step can only be determined iteratively.

If we compare equation (8.43) with the solution found earlier according to (8.30), it is noticeable that practically the same formula has been found. However, equation (8.43) is only found for $\theta>0$. For $\theta=0$ the iteration process does not depend on the values at the end of a step and the process is therefore directly 'converged' and this alternative approach has no point. Another difference is that the functions in equation (8.43) are evaluated for the estimate of the values at the end of a time step, by the method according to equation (8.30) at the start of a time step.

The assumptions will be summarised once more; firstly, it was assumed that the derivative of the plastic potential function around the solution is constant, secondly, a linearisation of Φ was used, no higher order terms were included. The third assumption was that the eigenvalue associated with the eigenvector $\partial g/\partial\underline{\sigma}$ is the maximum eigenvalue. The second assumption in particular may be a bad one, after all $\Phi = f^{\beta}/\tau$ and small changes in the stress may cause large changes in Φ.

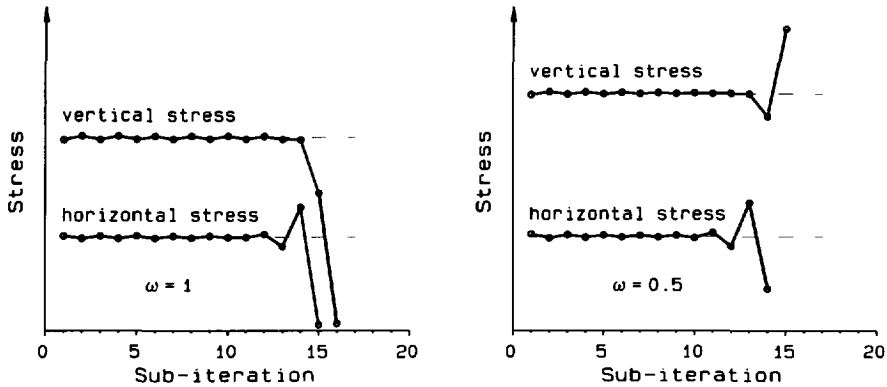

Fig. 8.3. Stresses during sub-iterations in a constant strain rate test simulation.

The usefulness of the under-relaxation can be shown by referring to an example. When calculating a triaxial test with constant confining pressure and an imposed vertical deformation rate, a steadily increasing time step is taken until divergence occurs. The vertical and horizontal stress for the various sub-iteration steps have been plotted in Fig. 8.3. Situations have been plotted in the figure at which divergence occurred. No under-relaxation was used for the left part of the figure, in the right of the figure an under-relaxation factor of 0.5 was used. The ratio in the time step between the two situations amounts to three.

From Fig. 8.3 we can see that the stresses change only slightly during the first sub-iterations. If we look further we see that there are oscillations, whereby no convergence occurs. Rather unexpectedly, divergence occurs. In the right part of the figure this divergence occurs at higher stresses, which means a greater value for the yield function f and also a greater value for $\frac{\partial \Phi}{\partial \underline{\sigma}}^T \underline{\underline{P}} \frac{\partial g}{\partial \underline{\sigma}}$. This means that the influence of an under-relaxation factor ω has a great influence on the convergence of the sub-iteration process.

8.6 Manipulation of control parameters for visco-plasticity

In the previous section a formula was derived for the convergence of the iteration process for the visco-plastic strain increment. For a calculation the time step is imposed. If fixed values for the integration parameter θ and the under-relaxation factor ω have been chosen, it appears quite rapidly whether the iteration process converges or diverges. With divergence the only solution is to choose smaller time steps, for example by dividing the time step up into a number of smaller time steps in which smaller strain increments are also imposed. One possibility where the same time increment can be calculated is to make the under-relaxation factor variable. From equation (8.41) we deduce that

$$\omega = \frac{1 - \lambda}{1 + \theta\Delta t \dfrac{\partial \Phi}{\partial \underline{\sigma}}^{T} \underline{\underline{P}} \dfrac{\partial g}{\partial \underline{\sigma}}} \tag{8.44}$$

During the sub-iteration process the denominator for the right hand term can be determined. By using a value for λ a value for ω can then be determined.

By referring to the development of the stresses in the subsequent sub-iterations, an estimate can be given for the eigenvalue λ. It applies that

$$\frac{|\Delta\underline{\sigma}_k - \Delta\underline{\sigma}_{k-1}|}{|\Delta\underline{\sigma}_{k-1} - \Delta\underline{\sigma}_{k-2}|} = \frac{|\underline{\underline{P}}\delta\Delta\underline{\varepsilon}_k^{vp} - \underline{\underline{P}}\delta\Delta\underline{\varepsilon}_{k-1}^{vp}|}{|\underline{\underline{P}}\delta\Delta\underline{\varepsilon}_{k-1}^{vp} - \underline{\underline{P}}\delta\Delta\underline{\varepsilon}_{k-2}^{vp}|} \approx \frac{|\lambda-1|}{|1-1/\lambda|} = |\lambda| \tag{8.45}$$

The sign for λ can be determined by considering the subsequent stress increments. If oscillations occur, the value of λ is negative. By using this estimate of λ a higher or lower value of the under-relaxation factor ω can be taken that follows from equation (8.44) with a selected value of λ.

The sub-iteration process can be stopped if the difference in stresses in subsequent iterations is sufficiently small, e.g. can be taken as

$$\frac{2\,|\Delta\underline{\sigma}_k - \Delta\underline{\sigma}_{k-1}|}{|\Delta\underline{\sigma}_k| + |\Delta\underline{\sigma}_{k-1}|} < \mathrm{TOL} \tag{8.46}$$

with TOL a small value, for example 1 to 5 per cent. In the case of a creep test, where constant stresses dominate, this convergence criterion can gives rise to problems because the denominator becomes small. For this reason something can be added to the denominator. The denominator can, for example, be:

$$|\Delta\underline{\sigma}_k| + |\Delta\underline{\sigma}_{k-1}| + \mathrm{TOL}\cdot|\underline{\sigma}_k| \tag{8.47}$$

so that finally a small difference is found for the stress increment in consecutive (sub)iterations.

One yield function was assumed in the above. As appeared in Section 7.3 in the case of triaxial compression states of stress, use was made of two yield functions. Particularly in the step from equation (8.34) to (8.35) changes will take place because the value of $\dot{\underline{\varepsilon}}_1^{vp*}$ now depends on a number of yield functions. Because of this the amplification matrix $\underline{\underline{A}}$ (equation 8.38) changes and there is analytically no eigenvector with associated eigenvalue to be derived. Through the estimate of the eigenvalue according to equation (8.45) the iteration process can be kept well under control as shown in Fig. 8.4.

Table 8.1. Values of ω and λ (according to eq. 8.45) for the data in Fig. 8.4.

	ω	λ	error
1	1		0.422
2	1		0.419
3	1	-1.193	0.502
4	0.9	-1.060	0.526
5	0.81	-0.869	0.457
6	0.729	-0.702	0.335
7	0.656	-0.525	0.173
8	0.590	-0.407	0.072
9	0.531	-0.387	0.028

	ω	λ	error
1	0.5		0.461
2	0.5		0.183
3	0.5	-1.231	0.204
4	0.45	-0.768	0.151
5	0.405	-0.888	0.132
6	0.364	-1.051	0.136
7	0.328	-1.817	0.245
8	0.295	-1.726	0.413
9	0.266	-1.410	0.564
10	0.239	-1.130	0.620
11	0.215	-0.898	0.555
12	0.194	-0.717	0.405
13	0.174	-0.586	0.243
14	0.157	-0.475	0.117
15	0.141	-0.348	0.041

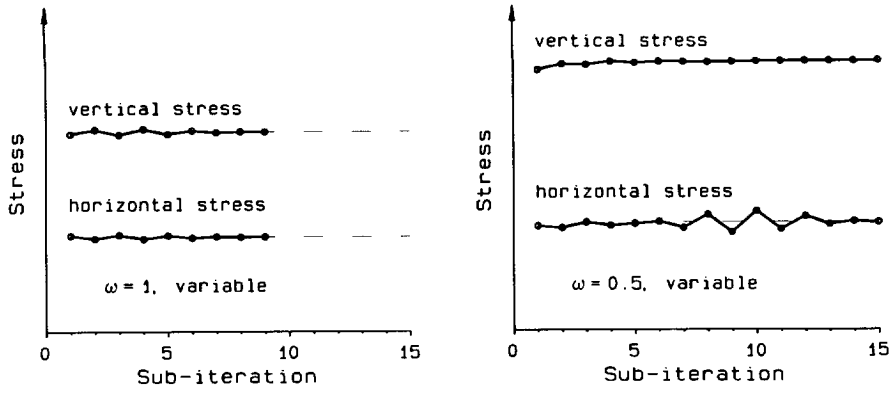

Fig. 8.4. Stresses during sub-iterations using a variable under-relaxation factor ω.

For Fig. 8.4 the same problem as in the previous section is calculated. The value of ω has been made variable. If the absolute value of λ according to equation (8.45) is too high, the value for ω is adjusted. As can be seen in the figure, the stress stabilises. In Table 8.1 the values of ω, λ according to equation (8.45) and the error according to equation (8.46) have been plotted for the various sub-iteration steps.

8.7 Simulation of multiple-step creep test

In a multiple-step creep test at any one moment the stresses are known. From these the strain rates of the Kelvin-Voigt elements can be determined at any one time. The visco-plastic strain rate still depends on the hardening variable κ. However, the value of κ at the end of a time step can be estimated well by extrapolation from the start of the time step; $\kappa_1 \approx \kappa_0 + \dot{\kappa}_0 \Delta t$. The total strain is then a simple addition of the contributions from the separate terms.

$$\Delta \underline{\varepsilon} = \Delta \underline{\varepsilon}_0^{ve} + \sum_{i=1}^{n} \Delta \underline{\varepsilon}_i^{ve} + \Delta \underline{\varepsilon}^{vp} \tag{8.48}$$

The separate contributions are derived in equation (8.8) for the strain increment of a Kelvin-Voigt element and in equation (8.17) for the visco-plastic strain increment.

On the basis of the principle outlined here of adding strain increments, is a rapid way to simulate a stress driven test. By simulating a multiple-step creep test the model will be tested. The simulation is a multiple-step creep test at a temperature of 28 °C. The confining pressure here is equal to 100 kPa. Some of the results of the test have already been used in Section 3.4 in the verification of the primary creep. The visco-elastic parameters that were used for the simulation, are taken from the results in Section 5.5, where the viscosities are scaled to a temperature of 28 °C. For the visco-plastic parameters, relative to the values in Table 7.2, deviant values of $M_{sct} = 0.6$ and $\kappa_{sct} = 0.025$ were taken, because in this case (the start of) the hardening curve is known. Relative to the generally found value this means a stiffer progress of the hardening curve; a difference of approximately 30 per cent. The creep exponent β (= 2.5) and the time parameter τ (= 1200 s) have been kept the same as the values found earlier in Section 3.4.

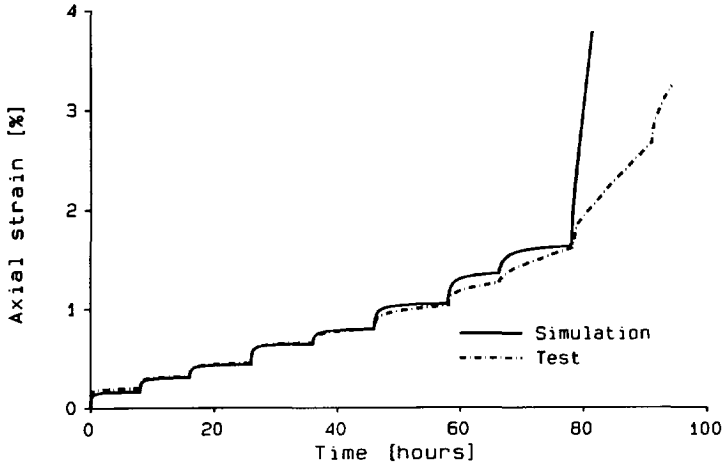

Fig. 8.5. Strain-time comparison. Multiple-step creep test and simulation.

In Fig. 8.5 the strain has been plotted against time. It appears from the figure that the test and the simulation show good agreement. However, for the highest stress, in the figure from approximately 80 hours, the simulation gives a much greater strain and strain rate than the test. The ratio between the strain rates is approximately a factor 8. If we wish to explain this in relation to the theory, this means that the value of the yield function is a good factor 2 too high. A value of the hardening function of approximately 0.625 would, in this case, give a much better approximation to the strain rate. It appears here that a change of only a few percent of M_{sct} can have a strong influence on the strain rate. Moreover, the influence of the change of M_{sct} can also be achieved by increasing the cohesion value, and with it a_{sct}, a little. This is to do with the maximum deviatoric stress that can be achieved and this is determined by both the parameter M_{sct} and the parameter a_{sct}.

8.8 Simulation of stress-relaxation test

The stress-relaxation test is a test where both the stress boundary condition and a displacement boundary condition apply. The axial strain is imposed in time; the radial stress is constant. This problem is tackled as follows. From an unbalance in the stress, a strain increment is determined with due observance to the imposed boundary condition of the strain increment. This unbalance in the stresses simply means that there is a difference between the stress present in the material - the constitutive stress - and the imposed stress - the equilibrium stress. By definition, there is no unbalance if a displacement boundary condition has been imposed. The strain increment is used for calculating the stress increment in accordance with equation (8.16) where the visco-plastic strain increment follows by using the procedures in Sections 8.5 and 8.6. An unbalance in the stress can be determined from this stress increment. From this a new strain increment can be determined that can be used for determining a new stress increment.

For the simulation a test was performed with an imposed vertical strain rate of $4.2 \cdot 10^{-5}$ [1/s], a confining pressure of 100 kPa and a temperature of 28 °C. In Fig. 8.6 the stress-strain relationships are plotted for the test and a simulation.

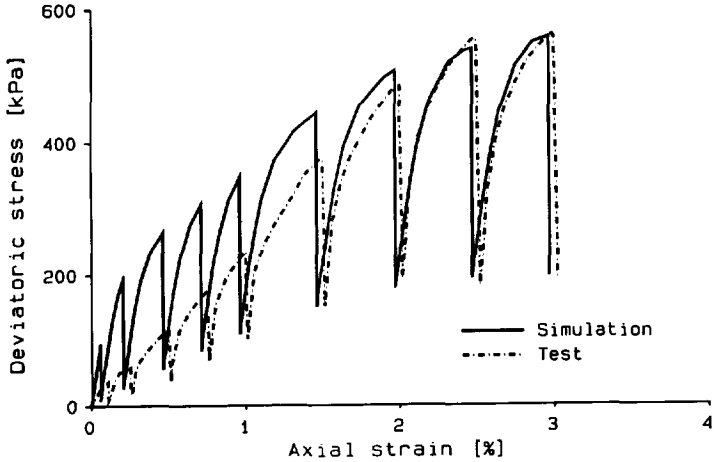

Fig. 8.6. Stress-strain comparison. Stress-relaxation test creep test and simulation.

As can be seen in the figure the stress at the start is overestimated. This means that the stiffness in the simulation is too great. Further investigation shows that the influence of the weak Kelvin-Voigt elements still has a reasonable influence on the build up of the stress. For this reason, a good description of the left part of the S-curve for cyclic loads is important.

9. FINITE ELEMENT IMPLEMENTATION AND VALIDATION

Once the model equations have been derived and the time integration has been dealt with, the next logical step is to formulate equations with which practical problems can be calculated. The formulas derived earlier were used for a finite element implementation.

In the previous chapters, test results were often used. For granular materials such as sand and bituminous concrete, which are often loaded with compression stresses, it is usual to present the results in such a way that shortening of the test specimen and compression stresses are plotted in a positive direction. In contrast to the previous chapters, the usual sign convention for mechanics will be used in this chapter. This means that tensile stresses are considered to be positive, just as a elongation is considered to be a positive strain.

9.1 Compatibility and equilibrium equations for finite element analysis

In a finite element approach a problem is divided up into a number of elements. The variables, such as displacements and stresses, that are used in the calculation are maintained in a limited number of points. By interpolation of the displacements from the nodes, the displacements can be calculated everywhere. This interpolation is done by means of shape functions. The displacements within an element are determined solely by the nodes in that element. Depending on the number of nodes a certain degree of interpolation is possible. Because the displacements are known throughout, the strains at any point can be determined. The strains at one point are calculated from the derivatives of the displacements at that point as

$$\underline{\varepsilon} = L\underline{u} \tag{9.1}$$

where

$$\underline{\varepsilon} = \begin{Bmatrix} \varepsilon_{xx} \\ \varepsilon_{yy} \\ \varepsilon_{zz} \\ \gamma_{xy} \end{Bmatrix} , \quad L = \begin{bmatrix} \frac{\partial}{\partial x} & 0 & 0 \\ 0 & \frac{\partial}{\partial y} & 0 \\ 0 & 0 & \frac{\partial}{\partial z} \\ \frac{\partial}{\partial y} & \frac{\partial}{\partial x} & 0 \end{bmatrix} , \quad \underline{u} = \begin{Bmatrix} u_x \\ u_y \\ u_z \end{Bmatrix}$$

in which L is a differential operator matrix, u_x , u_y and u_z are the displacement components at the point considered. These components can, by interpolation, be expressed in the displacements of the nodes in an element; for example

$$u_x = N_1 u_{x1} + N_2 u_{x2} + \ldots + N_n u_{xn} \tag{9.2}$$

where u_{x1}, u_{x2} etc. are the displacement components of the nodes in an element, n is the number of nodes in an element, and the functions N_1, N_2 etc. are the interpolation or shape functions. By the interpolation according to equation (9.2) a continuous displacement field follows.

By using the derivatives of the shape functions, by combining equations (9.1) and (9.2), the strains at any one point can be calculated; there follows

$$\underline{\varepsilon} = \underline{\underline{B}}\underline{a} \tag{9.3}$$

in which $\underline{\underline{B}}$ is the so-called strain interpolation matrix and $\underline{a}$ the vector with nodal displacements.

By using the strains, the stresses can be determined. These stresses should be in equilibrium with external loads such as weight and boundary loads. Although the displacements, by the correct choice of shape functions, are also continuous beyond the element edges, this does not need apply to the stresses. The equilibrium equations are

$$L^T \underline{\sigma} = -\underline{f} \tag{9.4}$$

where, if we only consider the x and y directions

$$L^T = \begin{bmatrix} \frac{\partial}{\partial x} & 0 & \frac{\partial}{\partial y} \\ 0 & \frac{\partial}{\partial y} & \frac{\partial}{\partial y} \end{bmatrix} \quad ; \quad \underline{\sigma} = \begin{Bmatrix} \sigma_{xx} \\ \sigma_{yy} \\ \sigma_{xy} \end{Bmatrix} \quad ; \quad \underline{f} = \begin{Bmatrix} f_x \\ f_y \end{Bmatrix}$$

in which f_x and f_y are body forces. Further, for the shear stresses it applies that $\sigma_{xy} = \sigma_{yx}$.

At the boundaries the stresses should be in equilibrium with the external load present.

9.2 Finite element equations

Starting with the virtual work equilibrium equation (Fung, 1965; Zienkiewicz, 1968) the following equations follow:

$$\int_V \underline{\underline{B}}^T \underline{\sigma} dV = \underline{q} \tag{9.5}$$

where V is the volume is of the problem under consideration. The load vector $\underline{q}$ arises through body forces, prescribed boundary stresses and other possible loads. The integral is calculated by Gauß integration, by using the data for a limited number of points in an element.

In calculations with (visco) plasticity, incremental relationships are assumed. At the end of a step, indicated by a subscript 1, it applies that

$$\begin{aligned} \underline{\sigma}_1 &= \underline{\sigma}_0 + \Delta\underline{\sigma} \qquad & \underline{\varepsilon}_1 &= \underline{\varepsilon}_0 + \Delta\underline{\varepsilon} \\ \underline{q}_1 &= \underline{q}_0 + \Delta\underline{q} \qquad & \underline{a}_1 &= \underline{a}_0 + \Delta\underline{a} \end{aligned} \tag{9.6}$$

Where a subscript 0 is used for the values at the start of a step.

If the equations (9.6) are substituted in equation (9.5) the following equation results

$$\int_V \underline{\underline{B}}^T \Delta\underline{\sigma} dV = \Delta\underline{q} + \underline{r}_0 \tag{9.7}$$

in which

$$\underline{r}_o = \underline{q}_o - \int_V \underline{\underline{B}}^T \underline{\sigma}_o dV$$

This vector $\underline{r}_o$ is the unbalance at the start of a step. In non-linear equations some unbalance will always occur. Inclusion of this unbalance prevents an accumulation of errors.

By now using the stress-strain relationship (8.13) together with equation (9.7) the following equation arises

$$\int_V \underline{\underline{B}}^T \underline{\underline{P}} \Delta\underline{\varepsilon} dV = \Delta\underline{q} + \underline{r}_o + \int_V \underline{\underline{B}}^T \underline{\underline{P}} \Delta\underline{\varepsilon}^{vp} dV - \int_V \underline{\underline{B}}^T \Delta\underline{\sigma}^{ve} dV \tag{9.8}$$

by using equation (9.3) for increments in strains and displacements ($\Delta\underline{\varepsilon}=\underline{\underline{B}}\Delta\underline{a}$) follows

$$\underline{\underline{K}}\Delta\underline{a} = \Delta\underline{q} + \underline{r}_o + \int_V \underline{\underline{B}}^T \underline{\underline{P}} \Delta\underline{\varepsilon}^{vp} dV - \int_V \underline{\underline{B}}^T \Delta\underline{\sigma}^{ve} dV \tag{9.9}$$

where the stiffness matrix $\underline{\underline{K}}$ is introduced as

$$\underline{\underline{K}} = \int_V \underline{\underline{B}}^T \underline{\underline{P}}\underline{\underline{B}} \, dV \tag{9.10}$$

Equation (9.9) can be solved for a first estimate by, for example, taking the (unknown) visco-plastic strain increment as zero. A set of displacement increments $\Delta\underline{a}_1$ then follows. By using these displacement increments, strains can be determined and with the procedures from Chapter 8, the stress increments and therefore stresses at the end of an iteration are determined and the equilibrium can be checked. If visco-plastic strains occur, there will generally be an unbalance between the internal stresses and the load applied. The unbalance at the end of iteration k is calculated as

$$\underline{r}_k = \underline{q}_o + \Delta\underline{q} - \int_V \underline{\underline{B}}^T \underline{\sigma} dV \tag{9.11}$$

This unbalance can be used to calculate additional displacements in a following iteration:

$$\underline{\underline{K}}\ \Delta \underline{a}_{k+1} = \underline{r}_k \tag{9.12}$$

The total displacement increment $\Delta \underline{a}$ is calculated as the sum of the contributions from all iterations

$$\Delta \underline{a} = \Delta \underline{a}_1 + \Delta \underline{a}_2 + \ldots + \Delta \underline{a}_{k+1} \tag{9.13}$$

The iteration process can be stopped if the unbalance after an iteration has become small, i.e. small in respect of, for example, the load vector.

The method outlined above gives the incremental displacements for a given load increment. It should be remarked here that the calculation of the stress increments should be converged. If when calculating the stress increments, divergence occurs, it is very unlikely that the unbalance vector $\underline{r}_k$ converges to zero.

9.3 **Accelerated solution techniques**

If the problem to be calculated is mainly determined by visco-plasticity, very many iterations may be required because the stiffness matrix is determined by using the relatively stiff Kelvin-Voigt elements. With respect to the procedure outlined above, it is possible to apply a number of acceleration techniques. Estimation of the displacement increment $\Delta \underline{a}_1$ according to equation (9.6), it is not necessary to calculate the whole right hand side. If in a calculation, one load is increased proportionally, a good approximation of $\Delta \underline{a}_1$ is possible by extrapolation of the results from the previous step. For proportional load increase it applies that (see also Vermeer and Van Langen, 1989)

$$\Delta \underline{q} = \Delta \underline{q}_{pr} \tag{9.14}$$

where $\Delta \underline{q}_{pr}$ is the load increment from the previous step. A good approximation for the first displacement increment is then

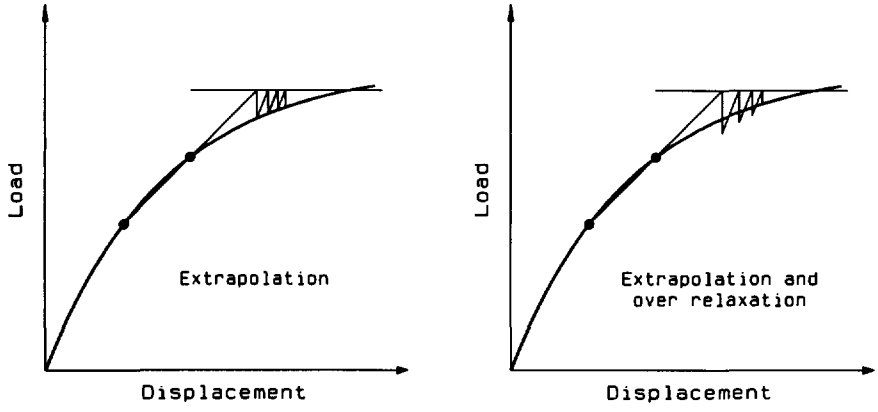

Fig. 9.1. Schematic representation of extrapolation procedure (left) and over-relaxation procedure (right).

$$\Delta \underline{a}_{-1} = \Delta \underline{a}_{-pr} \tag{9.15}$$

where $\Delta \underline{a}_{-pr}$ is the displacement increment from the previous step.

Another acceleration can be achieved by using the so-called over-relaxation. This means that the displacement increment is not calculated according to equation (9.12) but according to

$$\underline{\underline{K}}\ \Delta \underline{a}_{-k+1} = \omega\ \underline{r}_{-k} \tag{9.16}$$

For an over-relaxation factor ω that is a little greater than 1, a little more than the actual unbalance is solved. Under certain conditions it can be proved that the over-relaxation factor must lie between 0 and 2 in order to ensure convergence. One of the limitations to this proof is that associated behaviour is assumed. Considering that we are not dealing here with associated behaviour, this proof does not apply to the situation that we are considering.

The extrapolation procedure and the over-relaxation procedure are shown schematically in Fig. 9.1.

9.4 Validation of finite element implementation

A first validation of the finite element implementation is the comparison with problems from the literature. Preferably, these are problems that can be solved analytically. Considering that problems with visco-elasticity and visco-plasticity cannot or are very difficult to solve analytically, we have selected a problem here described by Booker and Small (1985). The problem involves a two layer system of a visco-elastic material on an elastic material. This system is loaded by a circular distributed load, as shown in Fig. 9.2. For the solution Booker and Small used a Finite Layer method, with which horizontally layered visco-elastic soils can be calculated. The great advantage of the method used is that a one dimensional discretisation is used, so that the computer storage used, compared with the finite element method, is limited. However, a disadvantage is the limitation of the geometry of the soil layers.

The two layers are of equal thickness. The radius of the circular loaded part is equal to the thickness of the layers. The Zener model is used for the visco-elastic material (Fig. 5.3), where the ratios between the spring stiffnesses and the relaxation time are given. The stiffness of the elastic material is equal to the initial stiffness of the visco-elastic material.

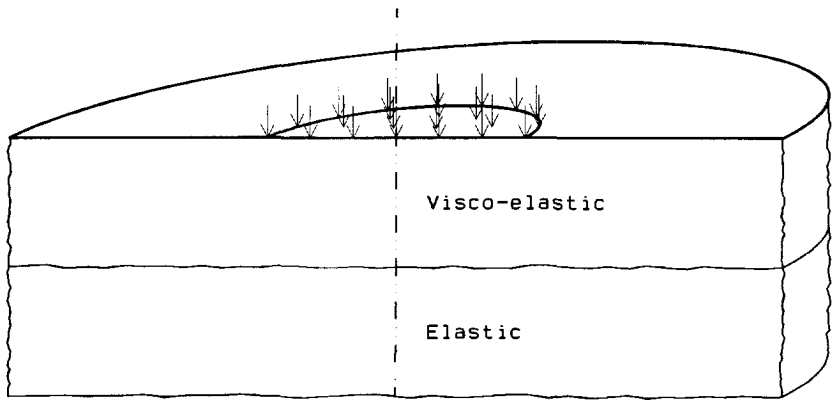

Fig. 9.2. Geometry of validation problem (after Booker and Small, 1985).

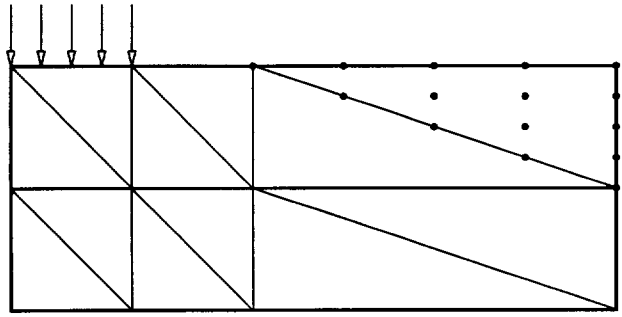

Fig. 9.3. Finite element schematization.

The element mesh in Fig. 9.3 has been chosen for the validation. The distribution into only 12 triangular elements appears to be very coarse, however high value 15-noded elements are used (n=15 in equation 9.2). In comparison with the original problem, where the layers are infinitely wide, the edge had to be chosen here. A boundary at a distance five times the radius of the loaded area was chosen. The lower boundary of the mesh is held completely fixed. Horizontal displacement is not possible along the vertical boundaries and the vertical displacements are free. The displacements on the upper side of the mesh are free.

The material parameters for the calculation have emerged as follows. The parameters are given in shear moduli, bulk moduli and a relaxation time. It is given that the ratio between bulk modulus, K, and the initial shear modulus, G_0, is equal to $\frac{8}{7}$. With the relationships $K = \frac{1}{3}E/(1-2\nu)$ and $G = \frac{1}{2}E/(1+\nu)$ a ν_0 value of $\frac{5}{31} = 0.1613$ follows. The bulk modulus has a constant value; this means that no volume changes occur in the Kelvin-Voigt element. In other words, a value of $\frac{1}{2}$ should be taken for Poisson's ratio ν_1. This is not possible in a finite element calculation and for that reason a value of 0.495 is taken. The ratio between the initial and final shear modulus is given as $G_\infty/G_0 = \frac{3}{10}$. It can be derived from this that $G_1 = \frac{3}{7}G_0$ and with the found ν values, $E_1 = \frac{31}{56}E_0$ follows. Finally, a ratio between the shear moduli and the (shear) viscosity follows from the relaxation time. The relaxation function for shear deformation is given as

$$G(t) = G_\infty + (G_0 - G_\infty)e^{-\lambda t}$$

where λ is the reciprocal value of the relaxation time. The parameter λ, for the Zener model, can be expressed in the shear moduli and the shear viscosity

$$\lambda = 3(G_0+G_1)/\eta_1$$

To summarise, for the visco-elastic material it follows that

$$\nu_0 = \frac{5}{31} = 0.1613$$

$$\nu_1 = 0.495 \ (\approx \frac{1}{2})$$

$$G_1 = \frac{3}{7}G_0$$

$$E_1 = \frac{31}{56}E_0$$

$$\eta_1 = 3(G_0+G_1)/\lambda$$

For the lower layer it applies that

$$E = E_0$$

$$\nu = \nu_0 = \frac{5}{31}$$

All parameters are known, or are dependent on two parameters to be chosen, E_0 and λ. In the original problem, a dimensionless displacement was plotted against a dimensionless time. The time is rendered dimensionless by plotting λt, the displacement by plotting $vG_0/(qa)$ whereby v is the vertical settlement of the centre of the area loaded, q the magnitude of the distributed load and a the radius of the area loaded, the radius of the area loaded is equal to the thickness of the layers.

The following choice was made for the time steps: after an initial step in which the load is applied instantaneously, the time step is taken that get progressively larger. It is ensured here that, plotted on a logarithmic scale, the time settlement progress can be followed easily. After a number of time steps, a total time of λt=100 follows. Considering that the time steps at the end become larger, there is a chance that oscillations occur and for

this reason the variable integration parameter for the Kelvin-Voigt element in accordance with equation (8.23) was chosen.

The results of the finite element calculation and the results according to Booker and Small are compared in Fig. 9.4. It appears that both methods give almost the same time settlement curve.

In addition to the time settlement curve, the stresses and strains can be compared on the symmetry axis. It appears from this that they agree well.

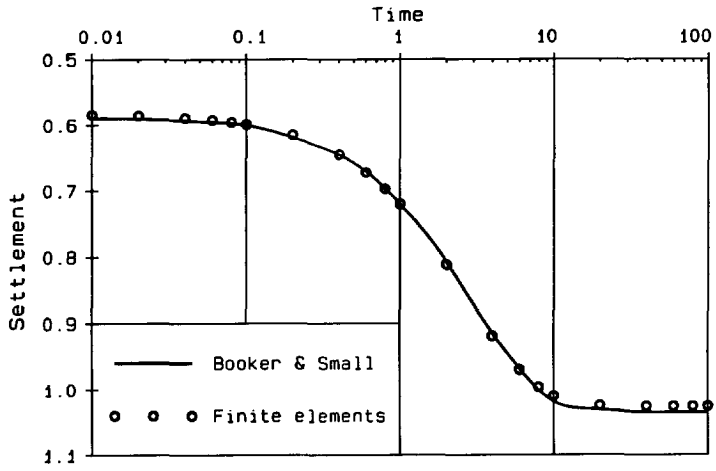

Fig. 9.4. Comparison of time-settlement curves for the Booker and Small (1985) problem.

10. ANALYSIS OF REVETMENT UNDER HYDRAULIC UPLIFT PRESSURES

One of the problems in the design of virtually impermeable dike revetments is the hydraulic uplift problem. This hydraulic uplift is caused by differences in water level inside and outside the dike body as illustrated in Fig. 10.1. If the water level outside the dike is lower than the water level inside, as caused by tidal movements, the resultant pressure may cause uplift or sliding of the protective revetment.

The problem of possible uplift of the protective revetment under tidal movements will be investigated here in more detail. The problem can be divided into two parts: the determination of the uplift pressures and the determination of deformations and stability due to the uplift pressures.

The constitutive model for bituminous concrete derived earlier will be used, though for this particular problem somewhat indirectly, as we use the model to estimate a suitably elastic Young's modulus for use in an elastic analysis as described in Section 10.5.

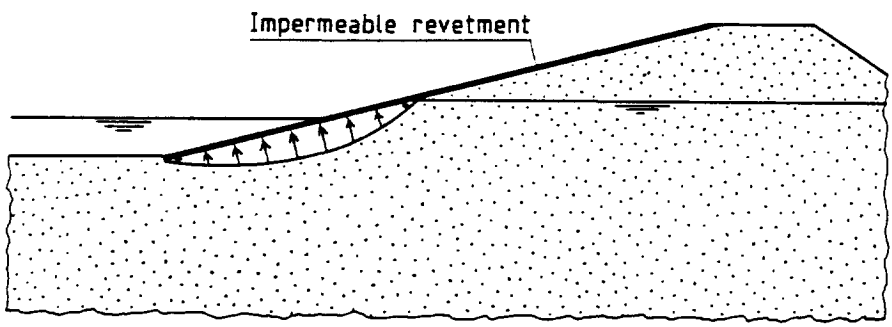

Fig. 10.1. Typical geometry of an embankment with impermeable revetment and possible resulting uplift pressures due to tidal water movements.

10.1 One-dimensional considerations

In order to become familiar with the phenomena, we will start with the situation of a one-dimensional case of an impermeable revetment on a sub-soil as shown in Fig. 10.2. From the figure we can see that equilibrium must be maintained between the forces acting on a small section of the revetment. Assuming that the forces in the revetment are in equilibrium, i.e. $\sigma_\alpha^l = \sigma_\alpha^r$ and $\tau_\alpha^l = \tau_\alpha^r = 0$ we only have the weight of the revetment and the contact pressure between the revetment and the sub-soil. Initially we have hydrostatic water pressures on both sides of the revetment. For this situation, the effective contact pressure σ'_c between the revetment and the sub-soil is equal to

$$\sigma'_c = (\gamma_a - \gamma_w) \cdot d_a \cdot \cos\alpha \tag{10.1}$$

where

γ_a = bulk weight of the revetment material
γ_w = bulk weight of water
d_a = thickness of the revetment
α = slope angle

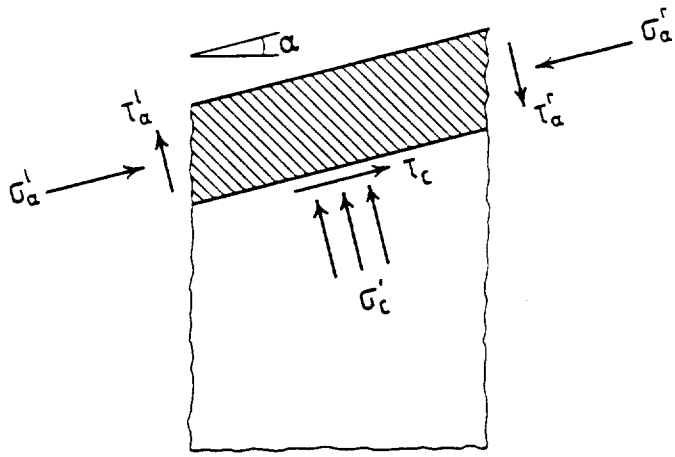

Fig. 10.2. In one-dimensional considerations the revetment is locally carried by the sub-soil, i.e. σ_α^l is assumed to be equal to σ_α^r and τ_α^l is assumed to coincide with τ_α^r.

When the water level above the revetment is lowered, without a change of the water pressures below the revetment, the effective contact pressure decreases:

$$\sigma'_c = (\gamma_a - \gamma_w) \cdot d_a \cdot \cos\alpha - \Delta\sigma_w \quad ; \quad \Delta\sigma_w = \gamma_w \cdot \Delta h_w \tag{10.2}$$

where Δh_w is the decrease of the water level above the revetment. It can be seen that the minimal thickness of the revetment is related to the decrease of the water level and the weight of the revetment material. Normal equilibrium will be ensured for

$$d_a \geq \frac{\Delta\sigma_w}{(\gamma_a - \gamma_w)\cos\alpha} \tag{10.3}$$

This is the uplift criterion according to the guidelines by the Dutch Technical Advisory committee on Water defences (TAW, 1984).

According to these guidelines, there are two criteria for the calculation of the thickness of a protective revetment under uplift pressures. One criterion exists for an uplift mechanism as described above. This uplift criterion should be used for situations that rarely occur, such as storm surges. Another criterion exists for a sliding mechanism, which should be used for situations that occur frequently, such as spring tides. The sliding criterion is based on equilibrium in the direction of the slope. According to this criterion, sliding will not occur as long as

$$d_a \geq \frac{\tan\theta \; \Delta\sigma_w}{(\gamma_a - \gamma_w) \cdot (\tan\theta \cos\alpha - \sin\alpha)} \tag{10.4}$$

where θ is the angle of friction between the revetment and the sub-soil. We obviously have $\theta \leq \phi$ where ϕ is the angle of internal friction of the sub-soil. Equation (10.4) is based on equilibrium of a section of the revetment assuming that the forces in the direction of the slope are in equilibrium, i.e. $\sigma^l_\alpha = \sigma^r_\alpha$.

It should be noted here that the sliding criterion (10.4) gives a greater thickness than the uplift criterion (10.3). Indeed, it can be seen that when the uplift criterion is satisfied exactly, the sliding criterion is not

satisfied. When there is no contact pressure between the revetment and the sub-soil, it is obvious that no shear stresses can exist. This means that tensile forces in the revetment will have to occur to compensate for the loss of shear stresses between the revetment and the sub-soil.

Using the formulas for the uplift criterion and a sliding criterion, it seems easy to determine the thickness of the revetment. However, there is one obstacle to determining the uplift pressure. The simplest way of calculating the hydraulic head difference Δh_w as caused by tidal actions is to assume a constant water table in the interior of the embankment. For this assumption, Δh_w would become equal to the drop of the outer tidal water and this would be extremely conservative. Therefore one uses the formula $\Delta h_w = c_r(h_{in.} - h_{out.})$, where c_r is a reduction factor, $h_{in.}$ water height inside the dike and $h_{out.}$ the water height outside the dike. A geometry dependent formula for c_r can be found in the guidelines (TAW, 1984).

10.2 **Two-dimensional ground water flow analysis**

The uplift problem can be separated into two different problems. The first problem is to determine the (maximum) uplift pressures and the second problem is to determine the safety against uplift and sliding for a particular structure. The first problem of determining the maximum uplift pressures can be dealt with by solving the boundary value problem for non-steady ground water flow. Of course one has to choose realistic boundary conditions. Similarly realistic data for permeabilities and phreatic storage are needed.

One particular case of ground water flow resulting from a storm surge will be investigated here in detail. This case involves a geometry as depicted in Fig. 10.3 with a slope of 1:4. The revetment is situated over the entire slope. The bottom of the mesh was taken at 20 m below the toe of the embankment. The left boundary was taken at 30 m to the left of the toe. At the right side the mesh is continued to a ditch at the inner toe of the embankment. It is a homogeneous soil profile and the permeabilities were taken to be 10^{-4} m/s in both the horizontal and vertical direction. Phreatic storage was taken into account by using an effective porosity of 30 per cent.

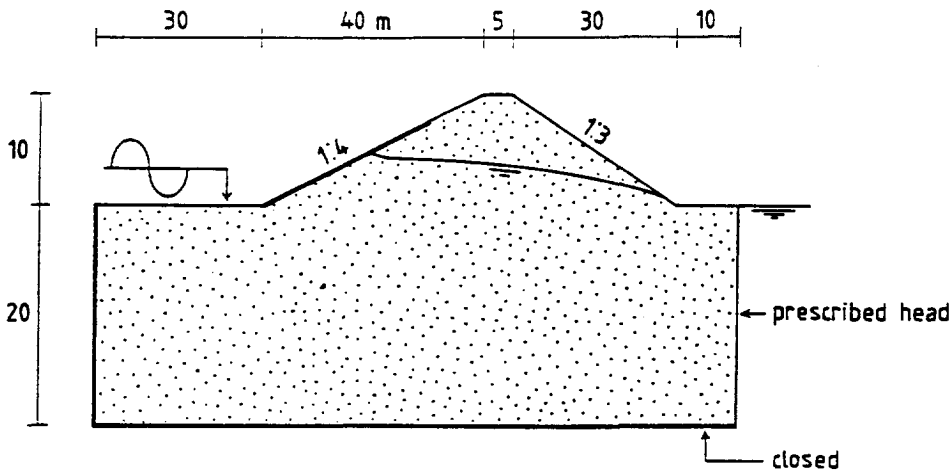

Fig. 10.3. Boundary value problem for non-steady ground water flow due to tidal variations.

The flow boundary conditions were taken as follows. At the horizontal part left of the toe a hydraulic head boundary was applied where the value depends on time to simulate several tides during a storm surge as shown in Fig. 10.4. The fluctuations include two periods of 12 hours and 25 minutes of normal tidal movements. The difference between high and low tides is 3.6 m. These first two periods are necessary in order to obtain a good approximation of the "initial" non-steady situation. After these first two periods there are three periods with increasing average water height to simulate storm tide and two periods with normal tide. The total simulated time is approximately 90 hours.

The slope of the embankment was taken to be impermeable. At the inner side of the embankment there is a seepage boundary condition which implies that water can flow out freely. The hydraulic head to the right of the inner toe was kept constant at the level of the outer toe. It should be noted that during the calculations the hydraulic head boundary condition attributable to the tide can change into a seepage boundary condition when the external water level is equal or below the surface.

The computations were done by Best (1991) by using the SEEP finite element code for non-steady ground water flow. From the calculations, the hydraulic

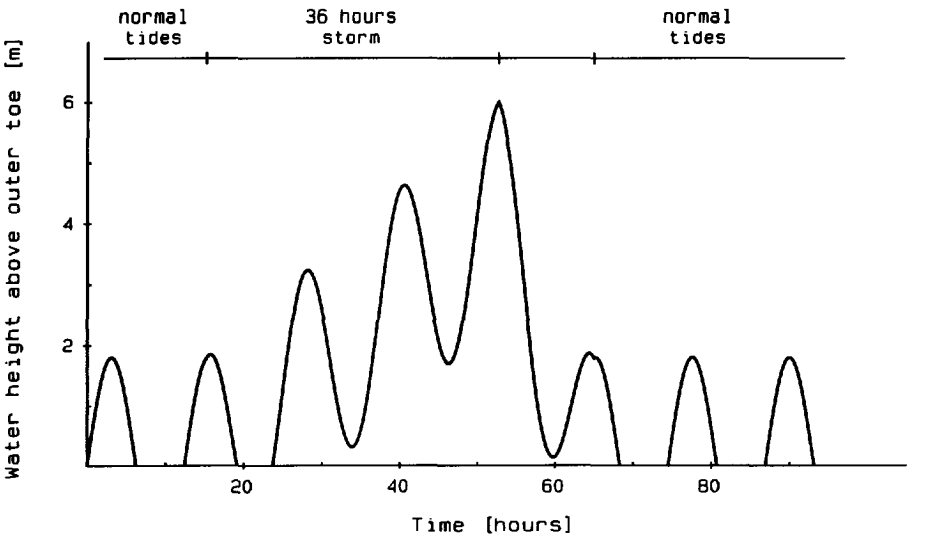

Fig. 10.4. Boundary condition at left side of toe for non-linear ground water flow calculation.

head at several points below the revetment are depicted in Fig. 10.5. From the difference in hydraulic head above and beneath the revetment, uplift pressures can be calculated. The calculation of the uplift pressures will be explained by using Fig. 10.6. In Fig. 10.6 we have plotted the water pressure outside the embankment (from the input boundary condition at the left side of the toe of the embankment) and the pore pressure at some point below the impermeable revetment. These pore pressures are calculated from the hydraulic head Φ

$$\Phi = y + \frac{\sigma_w}{\gamma_w} \qquad \text{or} \qquad \sigma_w = \gamma_w (\Phi - y) \tag{10.5}$$

Where y is the vertical coordinate relative to the toe of the embankment. When the water pressure outside is greater than the pore pressure inside, a resulting pressure will act downwards on the revetment and this pressure will cause an increase of the effective contact pressure between the revetment and the sub-soil. When the water pressure outside is lower than the pore pressure inside (the shaded area in Fig. 10.6), a resulting uplift pressure will occur.

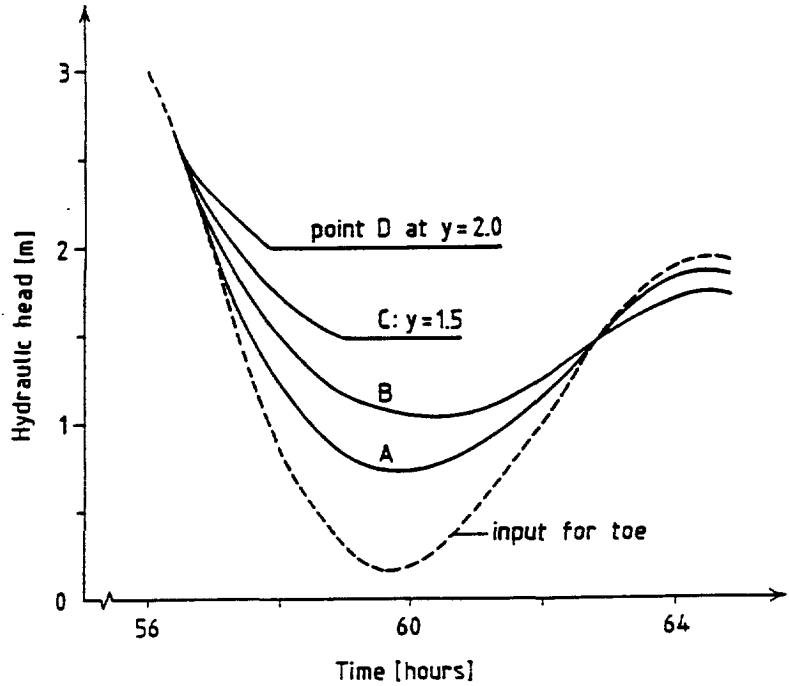

Fig. 10.5. Computed hydraulic head below revetment for points A, B, C and D in Fig. 10.8.

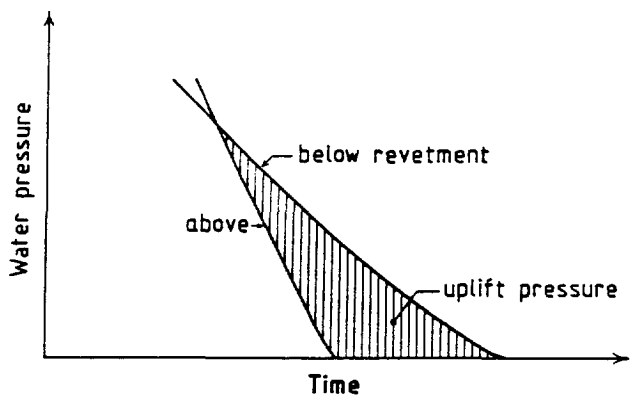

Fig. 10.6. Typical variation of water pressures for an element of the revetment. This output from non-steady ground water flow calculation is used to determine uplift pressures, which are needed as input for a deformation analysis.

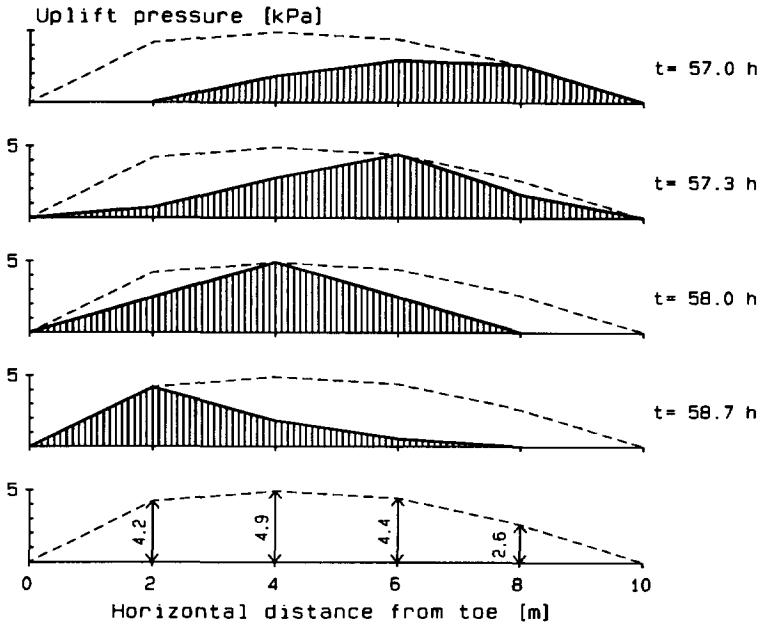

Fig. 10.7. Distribution of uplift pressures below revetment for various times.

The uplift pressures can be calculated from Fig. 10.5. In Fig. 10.5 we have on the vertical axis the hydraulic head Φ. As we know the vertical coordinates of the points A through D, we can calculate the pore pressures at these points. For the water pressure above the revetment we use the hydraulic head at the toe of the embankment, as this is input for the flow calculation. The water pressure at a point above the revetment can be calculated using equation (10.5); subtract the y-coordinate of the particular point and multiply it by the weight of water. When this gives a negative water pressure this indicates that the outer water level is below the point and we should set the water pressure to zero.

Calculation of the uplift pressure will give different distributions in time as shown in Fig. 10.7, where we plotted the distribution of the uplift pressures at various times. As can be seen from the figure, the location of the maximum uplift pressure shifts in time. The location at which the maximum uplift pressure occurs coincides approximately with the location of the external water level, which is going down in time.

One, conservative, approach is to use the maximum uplift pressures at different points and to assume that this distribution increases linearly in time to the maximum values and then decreases to zero. Another, more realistic, approach is to use different distributions of the uplift pressures for various times as shown in Fig. 10.7. Of course in the latter approximation it is possible to adjust the water level outside the embankment in time, whereas in the first approximation a constant water table must be used.

10.3 Input for two-dimensional deformation analysis

The second part of the analysis of the uplift problem involves the calculation of deformations and stresses. In this part the uplift pressures come from the results of the ground water flow simulation. For the deformation analysis we need to specify the region of interest, the boundary conditions and the material properties.

For the finite element calculations, a mesh had to be designed. Here we will not model the entire embankment. Instead a reduced area was modelled as indicated in Fig. 10.8. The left side of the mesh was taken at 4 m to the left of the toe of the embankment, the right boundary at 12 m to the right of the toe of the embankment. The bottom of the mesh was taken 5 m below the toe of the embankment. The protective revetment starts at the toe of the embankment and continues up to 2.5 m above the toe; in reality this may be much more, but this will suffice for the calculations. The thickness of the revetment was taken to be 0.25 m. The mesh consists of 580 nodes with 64, 15-node elements. Also interface elements were used between the sub-soil elements and the revetment elements to be able to model the interface behaviour (van Langen, 1991) and to follow the contact stresses between the sub-soil and the revetment.

The most realistic approach to activate the uplift pressures is to use the water pressures resulting from the ground water flow calculation and enter these in the finite elements. Unfortunately, it is not easy to do this. Therefore we will use the derived uplift pressures and a horizontal phreatic surface inside the embankment. The height of the phreatic surface inside the

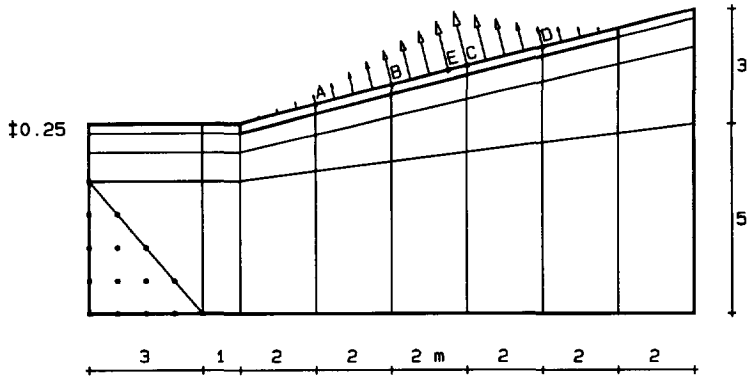

Fig. 10.8. Element mesh for deformation analysis with prescribed tractions to simulate uplift pressures.

embankment is equal to the external water level. This means that no pressures act on the revetment due to a difference in water level inside and outside the revetment. Entering the same phreatic surface inside the embankment as outside the embankment does have another effect. Seepage forces due to flow of water is disregarded. It is felt that this has little influence on the results. The uplift pressures acting on the revetment are treated correctly by entering them as tractions.

For the calculation we will use different uplift pressure distributions in time. We will start with the distribution at t= 57.3 h (see Fig. 10.7). These uplift pressures will be represented by tensile tractions acting on the top of the revetment as shown in Fig. 10.8. In reality the uplift pressures act at the bottom of the revetment but in the current version of the calculation program, PLAXIS, it is not possible to enter tractions inside the mesh. Due to the stiffness of the revetment it is expected that the results will be the same for both ways of modelling the uplift pressures. However, care should be taken that the tractions do not exceed an allowable tensile stress in the bituminous concrete because otherwise the revetment itself may fail.

For the calculation we have two materials: firstly the sand sub-soil and secondly the bituminous concrete for the revetment. For the sand we use an elastic perfectly plastic material model. For this material model we have linear elastic behaviour until the stresses reach a yield criterion. The

yield criterion is the well-known Mohr-Coulomb failure criterion. In order to get a realistic shear modulus of the sub-soil we use the following empirical formula for sand

$$G = \alpha p_0 \sqrt{\frac{p'}{p_0}} \qquad p' = \tfrac{1}{3}(\sigma'_1 + \sigma'_2 + \sigma'_3) \tag{10.6}$$

where

p_0 = 100 kPa
α = 50 to 150

The dash is used to indicate effective stresses. Later it will be shown that all deformations as caused by tidal action occur in a thin layer of soil just below the revetment. Therefore the relevant pressure level is about the weight of the revetment. For a bituminous concrete revetment with d_a = 0.25 m and a volumetric weight of 24 kN/m^3 this gives $p' \approx 4$ kPa. By using the above formula for the shear modulus we obtain values in the range 1000 to 3000 kPa. As most existing embankments are constructed from compacted sand, we will adopt the largest value; i.e. G = 3000 kPa. The Poisson's ratio was taken to be 0.3. The friction angle and dilation angle were taken to be $\phi = 35^\circ$ and $\psi = 5^\circ$, respectively, being realistic for sand. The cohesion was taken to be 1 kPa but no tensile stresses were allowed. On using a Mohr-Coulomb model with a so-called tension cut-off, the mechanical behaviour of the sand is considered to be modelled fairly well.

The material data used for the bituminous concrete will be explained in the next section.

10.4 **Material data for bituminous concrete**

For the bituminous concrete, we do not adopt the full model as described in previous chapters. Instead we use the full model to compute realistic parameters for a simplified model. To do this we need an estimation of the stresses in the revetment. These stresses can be input for a simple program to calculate strains for a given stress path in time. From this calculation we can find a relation between the maximum strain and the stress.

A realistic stress in the revetment can be found by considering equilibrium of a part of the revetment. Taking into account the uplift pressures and the initial contact pressure. The difference between these stresses will cause bending of the revetment. Over a certain area of the revetment the uplift pressures are larger than the initial contact pressures as shown in Fig. 10.9. This area can be calculated using the uplift pressures from Fig. 10.7 and the initial contact pressure from equation (10.1). This resulting load will give a bending moment. When we only consider this part where we have a resulting load, and assume zero moment at the ends, we can calculate the maximum bending moment. The assumption that the bending moments are zero at the ends is not very realistic; the ends are partially clamped. Therefore we can reduce the maximum bending moments somewhat.

When calculating the stresses due to bending for the situation that we will consider later on in the finite element calculation, we arrive at stresses due to bending in the order of 30 kPa. Due to the initial situation there are already some compressive stresses in the revetment. These compressive stresses are in the order of 5 to 10 kPa. Together with the stresses due to bending of the revetment we will get a maximum tensile stress in the bituminous concrete of about 20 to 25 kPa and a maximum compressive stress of about 35 to 40 kPa.

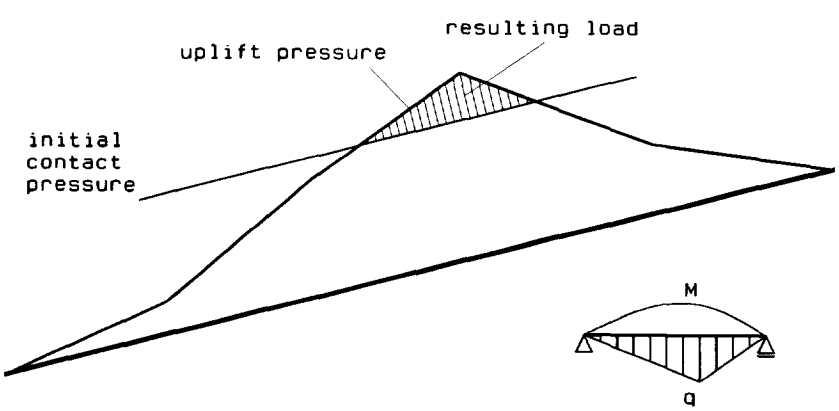

Fig. 10.9. Resulting load on the revetment.

These stresses will start to develop as soon as the contact pressure has vanished. The maximum stress is found when the uplift pressure has fully developed. From Fig. 10.7 we can deduce that the time during which the stresses develop is about 20 minutes.

Using this data for the stress development, we can calculate the strain response. We assume a linearly increasing stress in time up to the maximum stress of 40 kPa. After this we assume a linear decrease of the stress down to zero. This stress situation was entered in a small program to calculate the resulting strains. For this program we assumed that we have a uniaxial stress situation. The material parameters were taken from earlier chapters. The temperature dependent parameters were scaled, using the formulas derived in Chapter 6, to a temperature of 15 °C.

In Fig. 10.10 we plotted the resulting stress-strain curves for two situations; one for compression and one for tensile stresses. From the figure we observe that on loading we have a decreasing stiffness and while unloading we have some reversible strain and some irreversible strain as is to be expected from the model. We also observe that the irreversible strain is relatively large for the tensile stresses. This can be expected as the strength is lower and the visco-plastic strain rate is higher for tensile stresses.

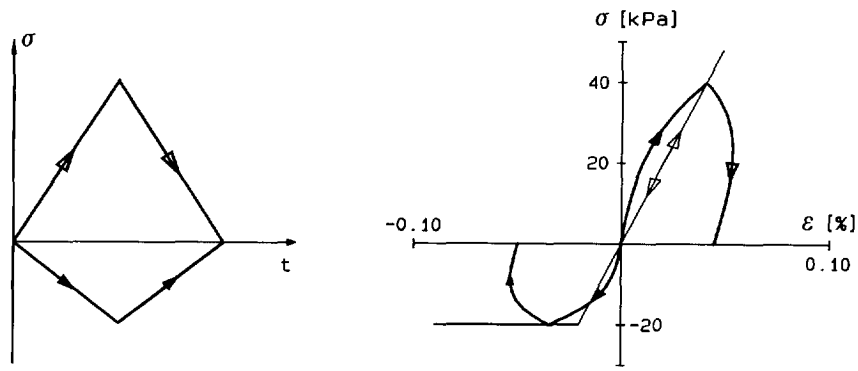

Fig. 10.10. Simulated stress situation and resulting stress-strain relation.

For the simplified material model for the bituminous concrete we use a relatively simple elastic-plastic model. For this model we use an average value of the stiffness modulus based on the result of the simulation with the full model. When we take the modulus resulting from the strains when the maximum stress is applied, as indicated in Fig. 10.10, for the compression test we find a stiffness value of 100 MPa and for the tension test we find a value of 60 MPa. In the finite element calculation we use a value of 100 MPa. From the simulation we see that in extension the strains are relatively large when compared with the strains in compression. Therefore, we included a limited tensile stress of 20 kPa. When using the relatively high stiffness from the compressive stress simulation, this gives a reasonable approximation of the stress-strain curve. This is shown in Fig. 10.10 where the bilinear approximation of the stress-strain relation is plotted. The strength in compression does not appear to be important, the maximum stresses in compression and in extension are about the same because bending will be most important in this problem. Therefore we use a friction angle of 15 degrees and a cohesion of 50 kPa.

After the calculation of the revetment under uplift pressures we can check whether the estimated stresses coincide with the calculated stresses in the revetment. If necessary, the calculation can be repeated using a more accurate estimation of stiffness of bituminous concrete.

10.5 Two-dimensional calculations and results

A first step in the calculation of the uplift problem is the calculation of the initial state due to soil weight and pore pressures. After this, the displacements were reset to zero as the initial deformations are irrelevant. The tractions, according the uplift pressures at t=57.3 h, were applied by incrementally increasing the tractions until failure occurs. The maximum value of the tractions at this time of 57.3 h is equal to 4.4 kPa.

From the output of the calculations we will first discuss the load-displacement curve as given in Fig. 10.11. In the curve we plotted the vertical displacement of a point E (see Fig. 10.8) at the surface of the revetment. This node, at which the displacement is extreme, is located at a

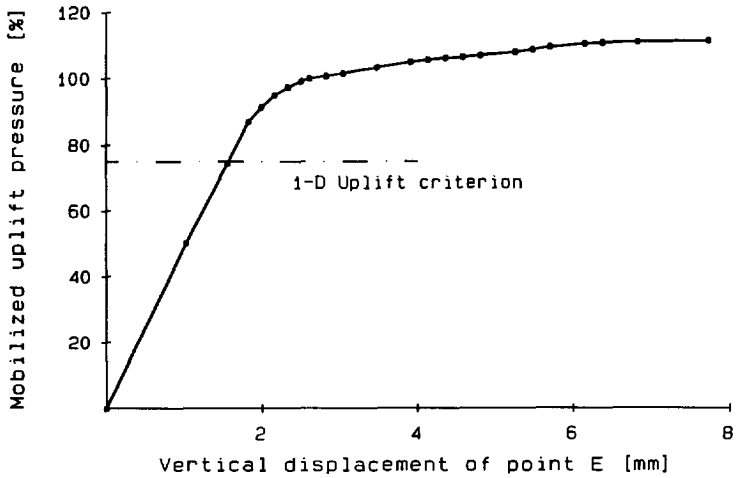

Fig. 10.11. Computed load-displacement curve for point E of the revetment.

horizontal distance of 5.5 m from the toe of the embankment. The vertical coordinate of the node is 1.375 m above the toe. It can be seen that the total tractions, or even more, can be applied, but the displacements increase more rapidly. The traction at failure is approximately 110 per cent of the input value: i.e. 4.8 kPa. According to the one-dimensional uplift criterion (10.3) we calculate a maximum traction of 3.3 kPa. The difference between the calculated failure traction and the value according to equation (10.3) can be explained by the fact that equation (10.3) does not take the shear stresses τ_α^l and τ_α^r (see Fig. 10.2) into account.

From the figure it can be seen that we have more or less elastic behaviour up to about 85 per cent of the maximum tractions. At this point the uplift criterion (10.3) is violated for a small area around the maximum traction. After this, the vertical displacement increases rapidly for increasing tractions. The cause of this can be seen when inspecting the deformed meshes at approximately 85 per cent and at failure. At a relative traction of 85 per cent we can see that there is a more or less uniform uplift of the revetment. This is mainly caused by a reduction of the effective stresses under the revetment resulting in small deformations in the sub-soil.

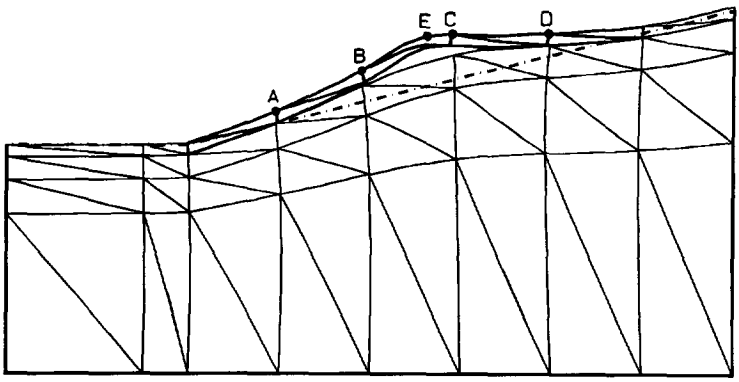

Fig. 10.12. Deformed mesh at full uplift pressures.

When continuing loading, the lack of weight has to be compensated in another way. When inspecting the deformed mesh (Fig. 10.12) at full loading, i.e. when 100 per cent of the load has been applied, we see that the uplift of the revetment is more local. From Fig. 10.12 we can see that the displacements at full loading involve mostly the revetment from x=4 m to x=6.5 m. The maximum opening of the gap is about 1 mm. The soil under the revetment does not displace further; a gap develops between the revetment and the sub-soil. This also means that the contact pressure between the revetment and the sub-soil has reduced to zero. The lack of weight in the zone around the maximum traction is compensated for by weight from regions where the uplift criterion is not violated. Now the bending of the revetment becomes important as the load has to be transferred by means of bending moments. The development of the bending moments will cause displacements. The values of the displacements will depend on the stiffness of the revetment material. When inspecting the deformed mesh at a relative load of 110 percent, we see that the gap has become larger. The maximum opening of the gap is now about 5 mm.

As indicated before, we have to check the resulting stresses in the revetment. From the situation where the tractions are fully activated (100 per cent of the load), we observe relatively low stresses in the revetment. The maximum tensile stresses in the revetment are in the order of 5 to 10 kPa, the maximum compressive stress in the revetment is in the order of 25 kPa. In the estimation of the stresses we derived stresses of about 20 kPa

and 40 kPa, respectively. The order of magnitude of the stresses seems to be correct. A difference exists in the initial contact pressures between the sub-soil and the revetment. The contact pressure is not constant along the revetment; above the water table the contact pressure is higher than below the water table. Around the water table there is a transition zone from lower to higher contact pressures. This means that the resulting load (see Fig. 10.9) becomes lower and therefore the stresses due to bending will be smaller. When using the stresses from the calculation to recalculate the proper stiffness of the bituminous concrete, it is found that the stiffness increases by about 30 per cent. It is felt that this difference in stiffness does not have much influence on the resulting failure load or displacements and therefore calculations were not repeated.

In Fig. 10.13 we see the plastic points, these are points where the yield criterion is violated; i.e. the material behaviour is plastic. The yield criterion comprises two criteria: the first is the Mohr-Coulomb yield criterion, the second is a tension cut-off criterion where tensile stresses cannot occur. The markers in the figure indicate that all plasticity occurs in the interface between the sub-soil and the revetment and we have some plasticity in the sub-soil. The type of marker indicates that the tension cut-off criterion is activated in most of the plastic points; this means that there are no contact stresses between the sub-soil and the revetment. For the

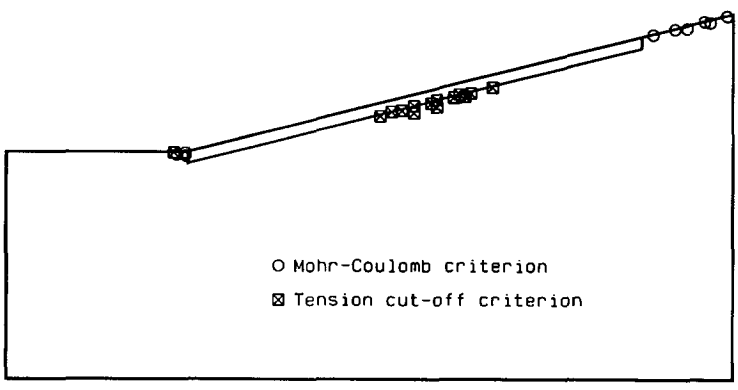

Fig. 10.13. Plastic points at full loading; in most points the tension criterion is used.

revetment, the tension cut-off criterion allows for some tensile stresses (20 kPa). From Fig. 10.13 we see that no plastic points occur in the revetment as can be expected because the maximum tensile stress in the revetment is about 5 to 10 kPa.

In the previous part is was shown that the tractions at t=57.3 h can be restrained and there is some extra safety against uplift of the revetment. The maximum uplift pressure at this time was 4.4 kPa, whereas the maximum uplift pressure of 4.9 kPa occurs at t=58 h (see Fig. 10.7). Therefore the calculation was continued. Also, from t=57.3 h to t=58 h the external water level becomes lower. This will result in an increase of the contact pressures between the sub-soil and the revetment. This lowering of the water level has been applied together with the change of the uplift pressure profile. It appeared that these changes resulted in a reduction of the deformations; the effect of increase of the contact pressure is, in this case, more important than the increase of the maximum uplift pressure. When increasing the loads to failure for t=58 h, it was found that more than 115 per cent of the load could be applied.

10.6 **Concluding remarks**

Using the uplift pressures according to the values from the time-dependent ground water flow calculation program, it is found that there is an extra safety margin of approximately 40 per cent when compared to the formulas in the guidelines (TAW, 1984). When the uplift criterion is violated, the displacements increase more rapidly. The question remains as to whether the increase of displacements is permissible or whether a criterion should be developed for the maximum displacements that will take place.

The method of using a relatively simple stress-strain relationship for the bituminous concrete appeared to be satisfactory. Using this method, one can simulate uplift behaviour rapidly when investigating, for instance, the influence of temperature on the deformations.

In these calculations it appeared that the maximum uplift pressure does not give the limiting case. It was found that the uplift pressure distribution at

an earlier time gave a lower safety margin. This may probably be caused by the water level for the calculation. For a lower water level the contact stresses between the sub-soil and the revetment increase and this effect is, in this case, more important than the increase of the uplift pressures.

An effect that has not been taken in to account in the calculations is that the external water level is not at all times horizontal and known. Because of waves, the external water level will change rapidly. This will cause local lower external water pressures and thus the uplift pressure, $\Delta\sigma_w$, according to equation (10.2) will increase. This happens only during short periods of time, in the order of magnitude of several seconds. For this short time one can expect that the bituminous concrete behaves more stiffly. Another phenomenon which has not been included in the above calculations, the filling of the gap, will be more important for these short loading times. When the gap is developing, the gap will be filled with water. This filling will cause additional pore pressures; the pore pressures under the revetment will decrease and thus we also have smaller uplift pressures.

11. PERMANENT DEFORMATIONS IN ROADS

One of the phenomena in road engineering that is receiving a lot of attention is the development of permanent deformations. Large wheel loads are the main cause of permanent deformations. Under a particular wheel load deformation occurs, some of which becomes permanent due to the incomplete recovery of the load-bearing structure. The development of these permanent deformations, also called rutting, depends on many factors. For instance, the magnitude of the wheel loads, the time interval during which the loads act on the structure and the number of loads. As the time interval is important, the temperature is also important as the material parameters of bituminous concrete are temperature-dependent.

The problem of rut formation has been simplified in this study. For this study stationary wheel loads of constant magnitude acting under constant temperature conditions have been assumed.

11.1 Modelling of the problem

As mentioned above the problem has been simplified. As the material model is implemented in a program for plane strain and axisymmetric problems (PLAXIS), moving wheel loads cannot be accurately described. In practice a vehicle moves at a certain speed and follows a certain track. The next vehicle, with a different load, may move at a different speed and follow a (slightly) different track. For the simulations moving loads will not be considered. Instead, the position of the load is fixed and an axisymmetric schematization is used. A single wheel load is considered and this load is schematized using a constant distributed load over a circular area with a diameter of 300 mm.

The typical geometry for a heavily loaded main road forms the basis of this study. The geometry is characterised as follows:

- 240 mm thick bituminous concrete top layer;
- 300 mm thick crushed masonry / crushed concrete sub-base.

These two layers are on a sand sub-soil (see Fig. 11.1).

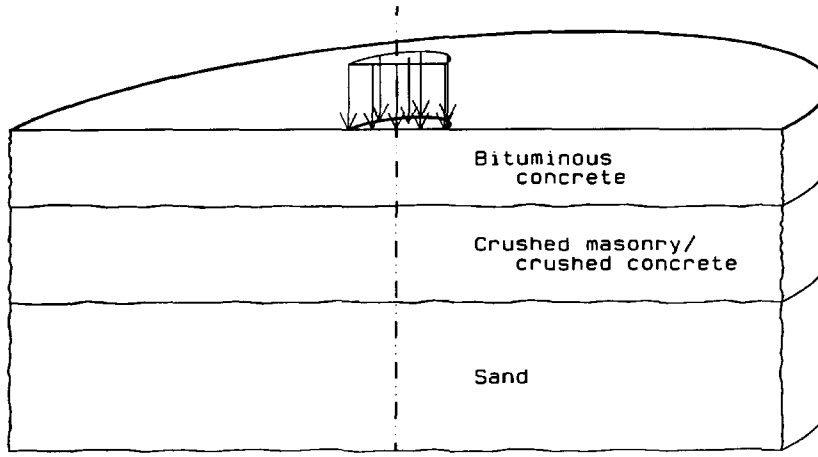

Fig. 11.1. The analysed geometry.

To include some of the effects of moving loads, a load pulse is described. The assumed load pulse is plotted in Fig. 11.2. The maximum time used here to describe the load pulse is 20 ms. This value is derived from the speed of a truck travelling at 15 m/s. Assuming a diameter of 300 mm for the wheel, a value of 20 ms is found. The shape of the load pulse is taken somewhat arbitrary. Allaart (1992) has investigated the effect of the shape of the load pulse in more detail. It was found that both the maximum value of the load and the impulse - the area of the time-load diagram - are important. Here we will restrict ourselves to the diagram in Fig. 11.2.

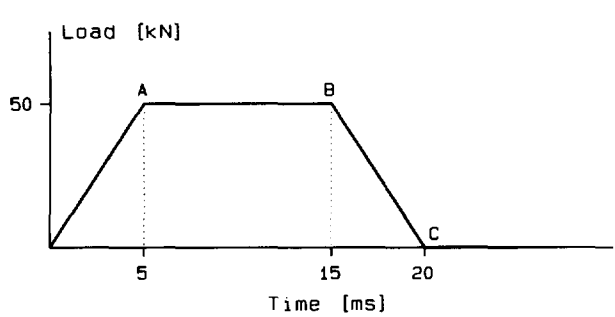

Fig. 11.2. Load-time diagram.

Table 11.1. Material parameters for sub-base materials.

Layer	1	2	
Material	crushed masonry/ crushed concrete	sand	
Depth	0.24 - 0.54	0.54 - 1.00	m
Weight	16	16	kN/m^3
E-modulus	500	100	MPa
Poisson's ratio	0.35	0.35	-
Cohesion	1	1	kPa
Friction angle	40	35	°
Dilation angle	10	5	°

For the sub-base material and the sub-soil an elastic-plastic material model was used. Elasticity is described using Hooke's law and plasticity is described using a non-associated Mohr-Coulomb model. The material parameters used for the sub-base material and the sub-soil are listed in Table 11.1. For the bituminous concrete we used parameters derived for our hydraulic bituminous concrete. The temperature of the bituminous concrete was taken to be 40 °C. This is rather high and it is questionable if this high temperature should be used for all calculations involving permanent deformations of road. In practice permanent deformations will also occur at lower temperatures but for this high temperature permanent deformations will develop more rapidly.

11.2 **Initial situation**

For the initial situation we will consider the construction without wheel load. The vertical stresses in the materials follow from the weight of the material on top. The horizontal stresses are derived from the vertical stresses and a K_0-factor. For the K_0-factor we used a value of 0.7 for the bituminous concrete and 0.6 for the base layers.

For the model for bituminous concrete these initial stresses give rise to some additional considerations. When initial stresses exist without initial strains in the Kelvin-Voigt elements, the constitutive model will give strain

rates in the Kelvin-Voigt elements (see equation 7.6 with $\underline{\sigma}\neq\underline{0}$ and $\underline{\varepsilon}_i^{ve}=\underline{0}$). To prevent this the initial strains in the Kelvin-Voigt elements can be calculated using

$$\underline{\varepsilon}_{i0}^{ve} = \underline{\underline{D}}_i^{-1}\ \underline{\sigma}_0 \tag{11.1}$$

Using this relation no initial strain rates will be found in the Kelvin-Voigt elements. For the visco-plastic part of the model we have a similar phenomenon when we use a hardening model. When we start off without any hardening (i.e. $\kappa=0$), we have no initial strength of the material and visco-plastic strain rates will follow. To prevent this an initial value for κ can be calculated, such that no visco-plastic strain rates occur. For the initial situation we demand that $f_0\leq 0$ where f_0 is the value of the yield function for the initial stresses. When using the yield function according to equation (7.9), it follows that for $f_0=0$:

$$\frac{\kappa}{\kappa_{sct}}\, e^{1-\kappa/\kappa_{sct}} = \frac{\tilde{q}}{p^*\, M_{sct}\left(1 - e^{-(p+p_1)/p_2}\right)} \tag{11.2}$$

When the initial stresses and the strength parameters are known, the right hand side of equation (11.2) is known. From the non-linear equation (11.2) the minimum value for κ can easily be solved. For the situation under consideration a value for κ of $4\cdot 10^{-4}$ will prevent visco-plastic strain rates in the initial situation. For this value of κ we have that the strength is less than 4 per cent of the maximum strength.

11.3 **Simulations**

For the simulations the finite element mesh in Fig. 11.3 was used. The top layer of bituminous concrete was modelled using two layers of 15-noded elements. The other two layers were modelled using only one layer of elements. The total number of 15-noded elements used for these simulations is 48. Additionally, interface elements were used, mainly to inspect the stress distribution at the interface between the bituminous concrete layer and the base layers.

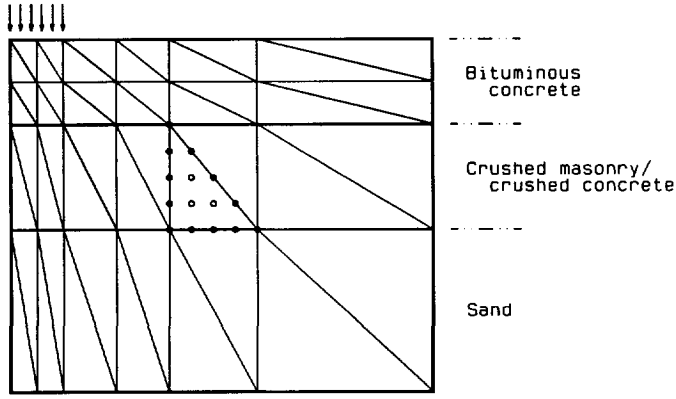

Fig. 11.3. Finite element mesh for simulations.

From the initial situation a first load cycle is applied according to the load-time diagram in Fig. 11.2. The load-time diagram is sub-divided into small time steps until t=25 ms. Thereafter this the calculation is continued using increasing values of the time step until a total time of about 5 s is reached. It appears that at this stage the displacements have reached a more or less stationary value as shown in Fig. 11.4.

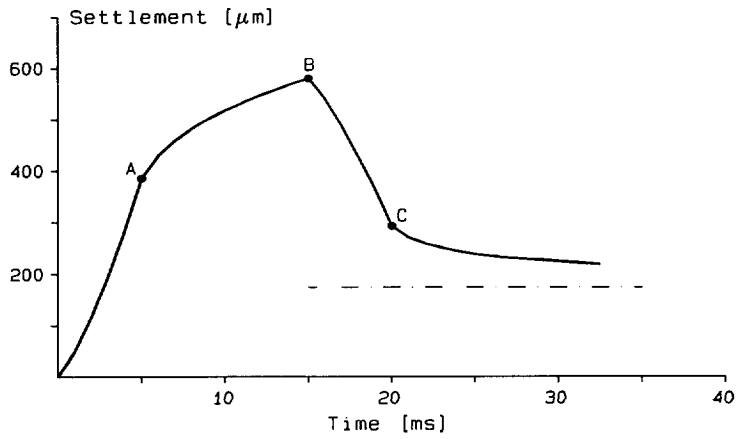

Fig. 11.4. Time-displacement curve for the centre of the loaded area. The points A, B and C are according to the points in the load-time diagram 11.2.

At this stage additional calculations were performed with a different number of Kelvin-Voigt elements. As stated in Section 8.4, the integration variable θ_i for Kelvin-Voigt element i of the Kelvin-Voigt series can be made dependent on the time step. For relatively large time steps, compared to the relaxation time η_i/E_i, a value close to 1 follows for θ_i. In this case we can also combine several Kelvin-Voigt elements, the first k Kelvin-Voigt elements with a relatively short relaxation time, to one elastic element for which we can use ($\eta_i \ll E_i \Delta t$, take $\eta_i=0$):

$$\sum_{i=0}^{k} \underline{\varepsilon}_i^{ve} \approx \left(\sum_{i=0}^{k} \underline{\underline{D}}_i^{-1} \right) \underline{\sigma} = \tilde{\underline{\underline{D}}}^{-1} \underline{\sigma} \tag{11.1}$$

$$\frac{1}{\tilde{E}} = \sum_{i=0}^{k} \frac{1}{E_i} \quad ; \quad \frac{1}{\tilde{G}} = \sum_{i=0}^{k} \frac{1}{G_i} \quad ; \quad \tilde{\nu} = \frac{\tilde{E}}{2\tilde{G}} - 1 \tag{11.2}$$

One elastic element using the parameters $\tilde{E}$, $\tilde{G}$, $\tilde{\nu}$ and $\eta=0$ replaces the first $k+1$ elements, this will reduce storage and to a lesser extent the computation time. In fact, using the combination of k Kelvin-Voigt elements into one elastic element, we are using a lower right asymptote of the S-curve for cyclic loading. Using this technique, we find that for this problem using these time steps, we can, for instance, use only 7 Kelvin-Voigt elements instead of 10 without notable influence on the stresses, strains and displacements.

The contact stresses between the layer of bituminous concrete and the sub-base can be examined. For the first load pulse, we can inspect the contact pressures at different characteristic times (Fig. 11.5). For instance, after 5 ms when the load is fully applied, after 10 ms, after 15 ms, when the load will be reduced again and after 20 ms, when the load has vanished. It appears that due to the relatively stiff behaviour of the material, the maximum contact pressure after 5 ms is approximately 180 kPa. This value increases to a value of approximately 270 kPa after 15 ms. This is caused by the decreasing stiffness due to the visco-elastic behaviour and the build up of visco-plastic strains. Although not very obvious from the figure, due to the relatively stiff behaviour of the bituminous concrete, the load is spread more after 5 ms than after 15 ms.

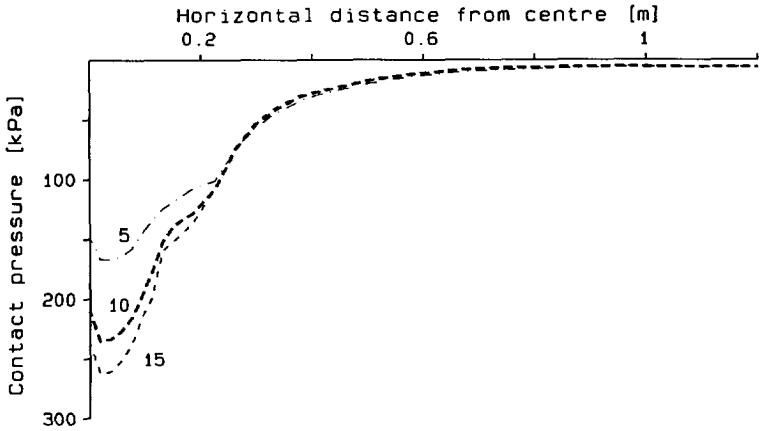

Fig. 11.5. Comparison of the contact pressure in the interface between the bituminous concrete and the sub-base for times of 5, 10 and 15 ms.

At this point we can plot the stresses and strains in the bituminous layer. This is done for points near the centre of the loaded area, both at the bottom and at the top of the layer of bituminous concrete. In Fig. 11.6 the vertical stress is plotted against the horizontal stress and the vertical strain against the horizontal strain for the first load pulse.

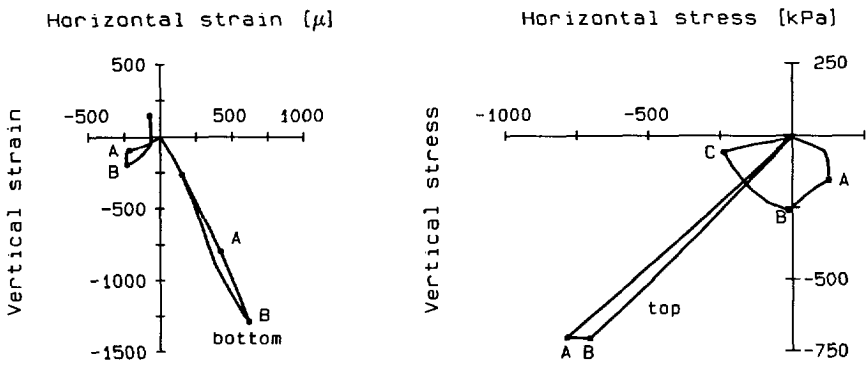

Fig. 11.6. Stresses and strains in the bottom and the top of the bituminous concrete layer for the first load pulse.

As can be seen from the figure we have very different reactions at the top of the layer and at the bottom. At the top of the layer we observe high compressive stresses (compression and shortening are negative in the figure) and small strains. For the bottom of the layer we observe relatively small stresses and relatively large strains. The stresses in the material are partly caused by the load and, especially the horizontal stresses, by bending of the layer. When considering bending of an elastic plate, the horizontal stresses should be about the same with different signs. When considering bituminous concrete, tensile stresses cause much more strains than compressive stresses. In this case the load will be carried by another mechanism where bending of the layer is less important. As can be seen from the figure the horizontal stress at the bottom of the layer changes sign from positive (tension) in point A, after 5 ms when the load is totally applied, to negative (compression) in point B, after 15 ms just before the load will be removed. During unloading, from point B to point C after 20 ms, it can be seen that the stresses in the top of the bituminous layer almost disappear, whereas in the bottom of the layer additional compressive stresses can be observed. After the load has disappeared stress relaxation is observed in the bottom of the layer.

11.4 Application of multiple load pulses

Considering the first load pulse only is not enough to understand the process of permanent deformations. Due to hardening and the build up of residual stresses, the mechanisms for the development of permanent deformations can change. Therefore additional load pulses were applied to the structure. Between every load pulse a rest time of approximately 5 seconds was allowed. This was done to be able to study the permanent deformation. After these 5 seconds a more or less stationary deformation is found and the influence of visco-elasticity is finished. In total 150 load pulses were applied. In Fig. 11.7 the permanent displacement of the centre of the loaded area is plotted against the number of load pulses. As can be seen from the figure, the permanent displacement still grows with every load pulse but the displacement due to a single load pulse decreases as the number of load pulses increases. Whereas the permanent displacement after the first load cycle is about 175 μm, an increment of about 15 μm is found for the last load pulse. It is

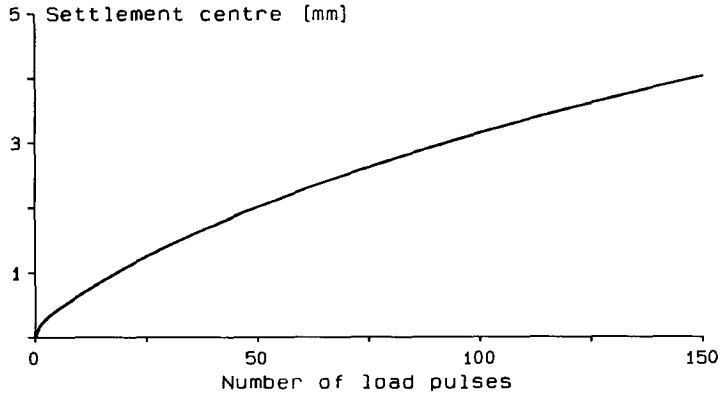

Fig. 11.7. Development of the permanent displacement of the centre of the loaded area.

interesting to compare the stresses during this last load pulse (Fig. 11.8) to the stresses during the first load pulse. As can be seen from the figure there is a shift of the stress path, especially for the stress path at the bottom of the bituminous layer. The stress path for the first load pulse starts near the origin whereas the stress path has shifted to more compressive stresses during the increase of the number of load pulses. In other words, a residual compressive stress builds up at the bottom of the bituminous concrete layer.

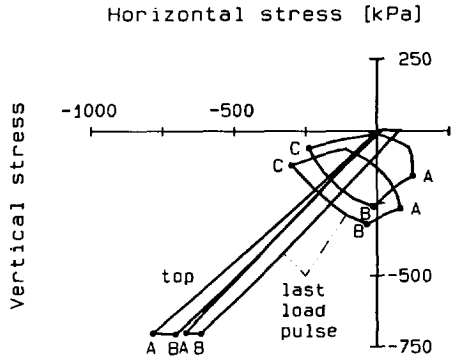

Fig. 11.8. Horizontal and vertical stresses at the bottom and the top of the bituminous concrete layer for the last load pulse.

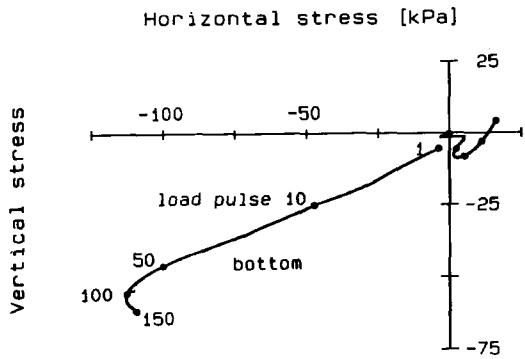

Fig. 11.9. Build up of residual horizontal and vertical stresses at the bottom and the top of the bituminous concrete layer during the load pulses.

The build up of permanent stresses at the top and the bottom of the bituminous concrete layer is plotted in Fig. 11.9. As can be seen from the figure we have an increasing compressive residual stresses at the bottom of the layer but the residual stresses seem to reach a more or less constant value. At the top of the layer we have rather small residual stresses. The vertical stress at the top of the layer should be about zero. The figure has been made using data from integration points near the top and bottom of the layer. Therefore the vertical stress at the top of the layer is not exactly zero.

We can consider the mechanism by considering the incremental permanent displacements due to a single load pulse. This was done for the last load pulse and in Fig. 11.10 the incremental permanent displacements are visualized. As can be seen from the figure we have a rather local mechanism. Most of the displacements occur in the bituminous concrete, below and near the edge of the loaded area. The vertical displacements of the top of the foundation layer are small compared to the displacements in the bituminous layer. From this it can be concluded that most of the permanent displacements are in the bituminous concrete.

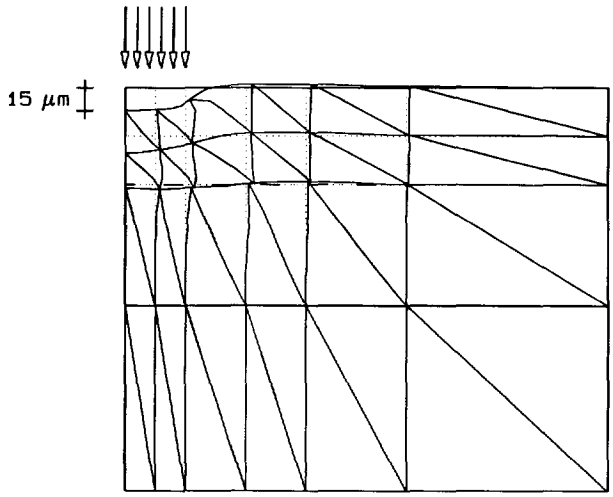

Fig. 11.10. Mesh deformation due to the last load pulse.

11.5 Concluding remarks

From these calculations we can draw several conclusions. Although we were not considering moving loads, the mechanism seems to be correct when considering a plane perpendicular to the direction of a moving load. In practice not all vehicles follow exactly the same track and this means that the shape of the permanent deformations at the surface are not described exactly.

The shape of the load pulse and the maximum load were not varied. It is thought that the shape of the load pulse and the magnitude of the load influence the permanent deformations. In practice not all loads have the same magnitude. For each load of about 50 kN there are many loads with a relatively low magnitude. These smaller loads also influence the permanent deformations, but their contribution to permanent deformations is much smaller.

One shortcoming in these calculations is its restriction to the use of our Delft bituminous concrete. This was done mostly because data for Delft bituminous concrete is readily available. These calculations should be

repeated using parameters for bituminous concrete used in roads. Therefore additional tests should be performed to obtain the parameters.

The effect of temperature was not included in these calculations. Instead a constant temperature was used. In reality the temperature will vary and permanent deformations will occur at all temperatures although the contribution of permanent deformations is thought to be lower at low temperatures.

For sake of simplicity all load pulses were applied using a time between successive load pulses which is relatively long. In this rest period most of the reversible strains are regained. In practice the resting time varies considerably. Between the loads of one truck the resting time is much smaller and between two heavy vehicles the resting time can be much longer.

12. DISCUSSION AND CONCLUSIONS

In this thesis a material model has been formulated for bituminous concrete. This material model is based on a number of tests which were conducted on Delft bituminous concrete. In the course of this series of tests an enormous amount of data has been generated. Although much of this data has been used for the formulation of the model and the determination of the parameters, much more information can be gleaned from the data. Not much attention has been paid in this thesis to the possibilities of reproducing these tests. In Section 4.2 thought has been given to the reproduction of the hardening curve from stress-relaxation tests. The results show very little scatter. The scatter of the results for strain using stress-based tests such as the multiple-creep test was, however, much greater. It appears that the hardening curves correspond very well to the results obtained from stress-relaxation tests. Under conditions of stress approaching the yield limit it appears, however, that strain and strain rate are very difficult to predict (cf. Fig. 8.5). As a result of the scatter of the strength of the material substantial differences can occur in strain rate - thus also with regard to strain - under a given condition of stress.

In Chapter 8 two tests have been simulated. A number of other tests remain however still to be simulated. This would allow for a comparison - in detail - of test results with the results of the simulations. Arising from the fact that many tests were repeated, the scatter for the parameters could thus also be determined.

In practical situations the scatter for the parameters is not always important, as not all parameters carry the same weight in these situations. In practical situations it is however important to be able to assess the importance of the individual parameters. Interaction with the sub-soil often occurs and there are different possible mechanisms to carry the load. If the load-bearing capacity of the bituminous concrete layer is low, a greater part of the load is transferred to the sub-soil. This is coupled with other forms of deformation, e.g. in the case of rutting permanent displacement will become concentrated and the rut deepens.

For the simulation of practical situations involving the use of bituminous concrete two conditions have to be met. It is firstly necessary to have sufficient information about the material and the parameters for the material model for each type of bituminous concrete, in particular for a typical bituminous concrete mix for use in road engineering. For example, it is apparent from Chapter 2 that while for Lyon bituminous concrete parallel stress lines were found for equal visco-plastic strains, for Delft bituminous concrete these lines were found to fan out from one point. Secondly, for the calculation of practical situations much work has to be done in the field of schematizing the practical situations and accompanying loads. In general, load and deformation influence each other, e.g. in the case of uplift of revetments of embankments a link can be traced between the flow of ground water and the deformation of the embankment. The division of the problem into two separate problems, viz. the determination of the load and thus the determination of the deformation, becomes less justifiable. This is also to be noted in the case of rutting of roads, where dynamics plays a role. Irregularities in the road surface could result in heavier local loading. Shear stress in the road surface - a result either of tyre deformation or forces originating from the drive-wheel - also influence its deformation.

(Scale) tests of practical problems, which can be simulated using finite element calculations, can be performed. The results from these tests can be compared to the results from the finite element simulation. A suitable test has been performed in Lausanne (Dumont, 1992). This test can be used to compare test results and finite element simulations.

Those aspects of the behaviour of bituminous concrete which have in this thesis received little or no attention are aging, fatigue and crack formation. Aging, i.e. behavioural changes over time, could be caused by temperature changes or by chemical reactions. To what extent these factors could be included in the model described in this thesis is not clear. Crack formation and fatigue are related phenomena. In the series of tests carried out within the framework of this research, failure - i.e. a reduction of relaxation stress in the stress-relaxation test - was used to signal the end of the test. The post-peak behaviour could therefore not be deduced from this series of tests. In the formulation of the hardening function a limited amount of post-peak strength reduction has been introduced. It is probable

that the strength reduction will occur more rapidly and that in practice localisation of the deformation will occur in the form of discrete crack formation. This phenomenon not only occurs with bituminous concrete but can also be observed in other materials such as concrete and sand.

It must be concluded that even with the development of a material model for bituminous concrete we are still a long way away from solving all the related problems. The development of an advanced material model such as described in this thesis is only a starting point in the attempt to gain more insight into the phenomena which occur in practice. The next step should be a detailed investigation and analysis of the parameters of models for various mixes of bituminous concrete and the schematization of the practical situations and accompanying loads.

Appendix **MATERIAL DESCRIPTION**

This appendix gives the description of the bituminous concrete tested in Delft and of the bituminous concrete tested in Lyon by Di Benedetto (1987). Delft bituminous concrete is a mixture used in hydraulic engineering for dyke revetment. Lyon bituminous concrete is a mixture that is more realistic for use in road construction. Delft bituminous concrete comprises a poorly graded grain skeleton of sand and gravel. Lyon bituminous concrete, on the other hand, comprises a very well-graded grain skeleton of sand and gravel. Delft bituminous concrete comprises a somewhat softer bitumen compared with Lyon bituminous concrete.
For a detailed description of the testing techniques for bituminous concrete and bituminous type materials, you are referred to the standards as set out in, for example, The Netherlands Standards (Bitumen and Tar Products, NEN 3901-3970).

Delft bituminous concrete
According to the guidelines for the application of asphalt in hydraulic engineering (TAW, 1984), bituminous concrete for hydraulic engineering purposes comprises a mixture of gravel, sand, filler and bitumen 80/100. A low void ratio should be obtained in order to obtain an impermeable layer. A low void ratio can be obtained by selecting an optimum ratio for the percentages of gravel, sand, filler and bitumen. For revetment thicknesses of more than 150 mm gravel 6/22 is used, in other words gravel with a diameter between 6 and 22 mm. For the ratio between gravel, sand and filler, the following values are recommended in the guideline; gravel ± 50 %, sand ± 42 % and filler ± 8 %. A mass percentage of approximately 7 in respect of the aggregate for the bitumen level is recommended. The bitumen 80/100 is used in order to obtain a flexible mixture.

The material investigated originated in the dyke revetment of the sea dyke near West-Kapelle in the South West of the Netherlands. A number of plates were sawn from this layer and samples drilled with a diameter of 100 mm. Most of the samples were drilled with the axis in the direction of the slope.

The density of the mixture, i.e. the aggregate with bitumen without voids, is fairly constant. Values were found of approximately 2413 kg/m^3, with a

deviation of less than 1 percent. With a void ratio of 2.5 % a density of the samples, which includes the voids, of approximately 2350 kg/m^3. This value agrees well with the density of the samples as determined in the testing of the samples.

The bitumen content amounts to an average of 6.2 %. This is a mass percentage with respect to the aggregate. Two characteristics were determined from the extracted bitumen. These are penetration by means of the penetration tests and the softening point using the test with ring and ball. The penetration test (see NEN 3949) is a test whereby a standard probe, loaded with a mass of 100 g, at a temperature of 25 °C for a period of 5 seconds penetrates into the bitumen. The value measured is expressed in 0.1 mm penetration. If a low penetration of, for example, 30 is found, this is referred to as hard bitumen. For a high penetration value of, for example, 300 this is referred to as soft bitumen. For the 15 samples that were investigated, an average value of 87 was found, where the individual values varied between 69 and 99.

The softening point (see NEN 3948) determines the temperature at which a standardized ball breaks through a ring with bitumen. The value measured is expressed in degrees Celsius. For the bitumen investigated an average value of 46.5 was found, with extreme values of 45 and 49.

Both the penetration and the softening point indicate a bitumen 80/100 as is stated in the guidelines (TAW, 1984).

The grain distribution in the aggregate is shown in Table A.1 and in Fig. A.1. As can be seen in the figure, what we have here is a gap-graded material, i.e. there is little aggregate present (±10 per cent) with a diameter between 0.5 and 4 mm.

Table A.1. Aggregate grading for Delft bituminous concrete. Minimum and maximum percentage passing sieve size. Data from 15 samples.

sieve size	passing (% by weight)
16 mm	99.2 - 100.0
11.2	85.9 - 91.5
8	66.6 - 74.5
5.6	53.7 - 62.1
4	49.2 - 56.5
2	47.0 - 54.1
500 μm	39.9 - 47.0
180	20.5 - 26.1
63	7.1 - 8.6

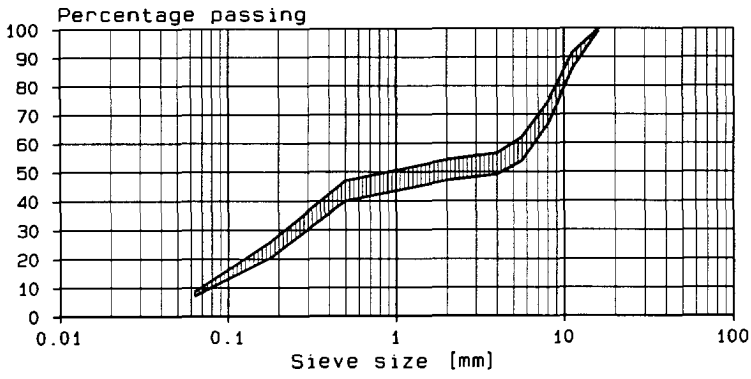

Fig. A.1. Aggregate grading for Delft bituminous concrete.

Lyon bituminous concrete

For this investigation results from triaxial tests by Di Benedetto (1987) were often used. For this reason, a profile of this material will also be given. The samples were created in the laboratory. The ingredients were selected carefully and mixed together. This mixture was then placed in a metal cylinder and the mixture was compressed under a certain pressure. Depending on the pressure with which the compression was carried out, a density was found. For the data presented, the density amounts to approximately 2350 kg/m^3.

The bitumen used is ELF-FEYZIN, type 60/70. Penetration tests give an average value of 59.4. A value of 48 °C was obtained for the softening point.

The bitumen content for this bituminous concrete amounts to 7.3 %, once again a mass percentage relative to the aggregate.

The grain material comprises 23 % aggregate 4/6 (diameter between 4 and 6 mm), 16.3 % aggregate 2/4, 56.4 % aggregate 0/2 and 4.3 % filler. The final grain distribution of the aggregate is determined for two aggregate mixtures and given in Table A.2 and in Fig. A.2 (Yan, 1988). As can be seen in this figure, there follows here, contrary to Delft bituminous concrete, a smooth progress to the curve; we are now dealing with a well-graded aggregate.

Table A.2. Aggregate grading for Lyon bituminous concrete. Data for two samples.

sieve size	passing (% by weight)	
6.3 mm	96.1	97.5
5	87.7	90.5
3.2	71.7	76.2
2	58.3	65.1
1	40.7	42.9
500 µm	27.3	23.4
200	18.4	15.3
80	12.6	10.1

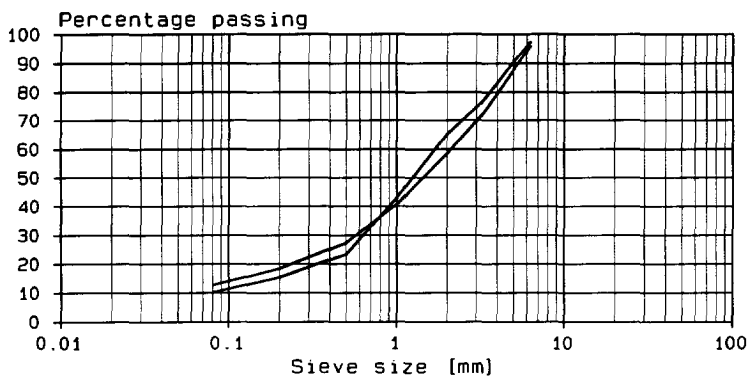

Fig. A.2. Aggregate grading for Lyon bituminous concrete.

REFERENCES

Allaart, A.P. Design principles for flexible pavements, a computational model for granular bases. Thesis Delft University, 1992.

Apicella, A., C. Caliendo, B. Festa and P. Giannatasio. Influence of polymer modifications on the viscoelastic behaviour of bitumens and on mechanical properties of bituminous mixtures: evaluation tests. In: Mechanical Tests for Bituminous Mixes. Proc. RILEM Budapest, 1990.

Argyris J.H., K.S. Pister and K.J. William. Thermomechanical creep of aging concrete. A unified approach. IABSE publication, 23-57, 1976.

Argyris J.H., K.S. Pister, J.Szimmat and K.J. William. Unified concepts of constitutive modelling and numerical solution methods for concrete creep problems. Comp. Meth. Appl. Mech. Eng. 10, 199-246, 1977.

Bailey, R.W. Trans. World Power Conf. Tokyo, 1089, 1929.

Bednar, K. Mastic asphalts modified by scrap rubber. In: Mechanical Tests for Bituminous Mixes. Proc. RILEM Budapest, 1990.

Best, H. Overdrukken onder asfalt taludbekleding onder invloed van extreme getijden, Grondmechanica Delft, 1991.

Booker, J.R. and J.C. Small. An investigation of the stability of numerical solutions of the equations of viscoelasticity. Int. J. Num. Meth. in Eng., vol. 11, 1819-1830, 1977.

Booker, J.R. and J.C. Small. Finite layer analysis of layered viscoelastic materials under three-dimensional loading conditions. Int. J. Num. Meth. in Eng., vol. 21, 1709-1727, 1985.

Borst, R. de. Thermomechanical analysis of aging visco-elastic soilids. TNO IBBC report BI-84-35/68.6.0230. Rijswijk, 1984.

Chauvin, J.J. L'essai de module complexe utilise pour la formulation des enrobés (Complex modulus testing for coating formulation). In: Mechanical Tests for Bituminous Mixes. Proc. RILEM, Budapest, 1990.

Cormeau, I. Numerical stabilty in quasi-static elasto/visco-plasticity. Int. J. Num. Meth. in Eng., vol. 9, 109-127, 1975.

Di Benedetto H., 'Modélisation du comportement des géomatériaux. Application aux enrobés bitumineux et aux bitumes', D.E. Thesis, Lyon France, 1987.

Dumont, A.G., EPFL Lausanne, Private communications, 1992.

Ferry, J.D. Viscoelastic Properties of Polymers. New-York: Wiley, 1980.

Fung, Y.C. Foundations of solid mechanics. Prentice-Hall New Jersey, 1965.

Gerritsen, A.H. , C.A.P.M. van Gurp, J.P.J. van der Heide, A.A.A. Molenaar and A.C. Pronk. Prediction and prevention of surface cracking in asphaltic pavements, Proc. 6th Int. Conf. Structural Design of Asphalt Pavements, Ann Arbor, USA, 1987.

Glasstone, S., K.J. Laider, H. Eyring. The theory of rate processes. New York: McGraw-Hill, 1941.

Hult, J.A.H., Creep in Engineering Structures, Blaisdel Publ. Co., Waltham, Massachusetts, 1966.

Koiter, W.T., General theorems for elastic-plastic solids. In: Progress in Solid Mechanics, Vol.1 (Eds. Sneddon and Hill), 165-221. North Holland Publishing Co., Amsterdam, 1960.

Langen, H. van, Numerical Analysis of Soil-Structure Analysis. Dissertation, Delft University of Technology, Delft, 1991.

Montauban, C.C., Asfaltbetonbekleding van de proefvakken West-Kapelle, Rijkswaterstaat, 1988.

Netherlands Standards-Bitumen and Tar Products. NEN 3901 - 3970, Nederlands Normalisatie Instituut, Delft.

Norton, F.H., Creep of Steel at High Temperatures. McGraw-Hill, New York, 1929.

Nunn, M.E. Prediction of permanent deformation in bituminous pavement layers. Eurobitume, 1985.

Odqvist, F.K.J. - Mathematical Theory of Creep and Creep Rupture, Clarendon Press, Oxford, 1966.

Perzyna, P. - Fundamental Problems in Viscoplasticity. Advan. Appl. Mech., 9, 243-377, 1966.

PLAXIS Manual, P.A. Vermeer (editor). A.A. Balkema, Rotterdam, the Netherlands, 1991.

Prandtl, L.Z. - Angew. Math. Mech., 8, 85-106, 1928.

Ruygrok, P.A., Kort verslag van het onderzoek op monsters met behulp van de OYO SONIC VIEWER, Delft Geotechnics, 1987.

Ruygrok, P.A., Triaxiale beproeving van asfaltbeton ten behoeve van een constitutief model (meetrapport), Delft Geotechnics, 1991.

Schapery, R.A., Viscoelastic behaviour and analysis of composite materials. In: Composite materials, Vol. 2. Mechanics of composite materials, Ed. G.P. Sendeckyj, 1974.

Schmalz, M., R. Letsch and M. Plannerer. Investigation on High and Low temperature behaviour ofasphalt by static and dynamic creep tests. In: Mechanical Tests for Bituminous Mixes. Proc. RILEM Budapest, 1990.

Soderberg, C.R., Trans. ASME, 58, 733-743, 1936.

Stolle, D.F.E. and J.E. Higgins. Viscoplasticity and plasticity - numerical stability revisited. Proc. NUMOG III, Elsevier, 1989.

Technische Adviescommissie voor de Waterkeringen, Leidraad voor de toepassing van asfalt in de waterbouw, 's Gravenhage, 1984.

Terrel, R.L., I.S. Awad and L.R. Foss. Techniques for characterizing bituminous materials using a versatile triaxial testing system. In Fatique and dynamic testing of bituminous mixtures, ASTM STP 561, 47-66, 1973.

Troost E., Mechanical behaviour of asphalt concrete, Proc. NUMOG III, Elsevier, 1989.

Vermeer, P.A. and H. van Langen. Soil collapse computations with finite elements. Ingenieur-Archiv 59, 221-236, 1989.

Yan, X., Etude du comportement mécanique de matériaux traités aux liants hydrocarbonés, Lyon France, 1987.

Zener, C., Elasticity and Anelasticity of Metals. Chigaco: Univ. of Chicago Press, 1948.

Zienkiewicz, O.C., M. Watson and I.P. King. A numerical method of visco-elastic stress analysis. Int. J. Mech. Sci. 10, 807-827, 1968.

SUMMARY IN DUTCH (Samenvatting)

In deze studie is het vervormingsgedrag van asfaltbeton onderzocht. Evenals het gedrag van vele andere materialen wordt hier onderscheid gemaakt in twee typen materiaalgedrag, te weten reversibel visco-elastisch gedrag en irreversibel visco-plastisch gedrag. In dit proefschrift wordt in de hoofdstukken 2, 3 en 4 begonnen met de beschrijving van de irreversibele rekken. Voor de irreversibele rekken wordt uitgegaan van zogenaamde over-stress visco-plasticiteit (Perzyna, 1966). In hoofdstuk 2 wordt de formulering beperkt tot secundaire kruip, dit is voornamelijk relevant voor hoge spanningen. In hoofdstuk 3 wordt de formulering uitgebreid zodat ook primaire kruip kan worden beschreven. Primaire kruip is voornamelijk van belang voor lage spanningen. Voor het beschrijven van primaire kruip wordt een hardenings formulering gebruikt. In hoofdstuk 4 wordt aan de hand van een groot aantal proeven een éénduidige hardeningscurve afgeleid. Deze hardeningscurve blijkt onafhankelijk te zijn van onder andere de snelheid van vervormen, de temperatuur en de steundruk. Ook wordt in dit hoofdstuk aandacht besteed aan het gedrag bij lage drukspanningen en bij trekspanningen.

In hoofdstuk 5 wordt visco-elasticiteit behandeld. De reversibele visco-elastische rekken worden beschreven door een keten van Kelvin-Voigt elementen. Resultaten van cyclische proeven worden beschouwd en vergeleken met resultaten van belasting-ontlastings proeven. Het blijkt dat combinatie van de resultaten een consistent beeld oplevert. Deze resultaten kunnen worden beschreven met behulp van een serie Kelvin-Voigt elementen.

Temperatuur is belangrijk voor de vervormingen van asfaltbeton. In hoofdstuk 6 wordt de invloed van de temperatuur op de model parameters bepaald. Het blijkt dat de temperatuur afhankelijke model parameters beschreven kunnen worden met behulp van simpele formules.

In de hoofdstukken 2 t/m 6 zijn model vergelijkingen opgesteld voor één-assige en triaxiale spannings situaties. In hoofdstuk 7 wordt het model uitgebreid naar algemene drie-dimensionale spannings- en reksituaties. In dit hoofdstuk worden de model parameters voor Delft bituminous concrete afgeleid.

In hoofdstuk 8 wordt ingegaan op de tijdsintegratie van de model vergelijkingen. In de voorgaande hoofdstukken werden de model vergelijkingen uitgedrukt in vervormingssnelheden. Voor berekeningen naar praktijksituaties moeten tijdstappen worden gebruikt. Daarom zijn er incrementele vergelijkingen voor spanningen en rekken opgesteld. Hier wordt ook aandacht besteed aan convergentie en nauwkeurigheid van het tijdsintegratie proces. Twee proeftypes worden gesimuleerd met behulp van een programma voor homogene spannings- en reksituaties.

In hoofdstuk 9 worden de vergelijkingen gegeven voor het oplossen van een randvoorwaarde probleem. Er worden ook enkele versnellingstechnieken beschreven. Een probleem met visco-elastische materiaalgedrag wordt behandeld als validatie van de eindige elementen implementatie.

Hoofdstuk 10 behandelt een simulatie van het opdrijven van een dijkbekleding. Voor dit opdrijfprobleem worden de resultaten van een tijdsafhankelijke grondwaterstromings analyse beschreven. Deze resultaten worden gebruikt om de vervormingen en de veiligheid te berekenen voor een dijkbekleding. De veiligheid wordt vergeleken met het opdrijfcriterium in de Nederlandse Leidraad.

In hoofdstuk 11 wordt gekeken naar blijvende vervormingen bij wegen. Een versimpeld spoorvormings probleem wordt behandeld. In plaats van verplaatsende belastingen, zoals die in de praktijk optreden, wordt een niet-bewegende belasting aangenomen. De nadruk ligt op de blijvende vervormingen en het mechanisme wat optreedt gedurende een aantal belastingen.

Hoofstuk 12 bevat enkele algemene conclusies en aanbevelingen voor verder onderzoek naar het gedrag van asfaltbeton en de toepassing van numerieke modellen voor het berekenen van praktische situaties.

CURRICULUM VITAE

Naam	Paul Godfried Bonnier
12 September 1964	Geboren te Nijmegen.
Sept. 1976-juni 1982	Petrus Canisius College te Alkmaar, afgesloten met Atheneum-B diploma.
Sept. 1982-maart 1988	TU Delft, studierichting Civiele Techniek, afgesloten met het behalen van het diploma (met lof) van civiel ingenieur (okt. 1988). Afstudeerrichting Mechanica en Constructies
Sept. 1988-juli 1993	Assistent-in-Opleiding aan de Technische Universiteit Delft, Faculteit der Civiele Techniek.